

KĪLAUEA VOLCANO DEFORMATION AND LAVA FLOW DYNAMICS

A DISSERTATION SUBMITTED TO THE GRADUATE DIVISION OF THE UNIVERSITY
OF HAWAI‘I AT MĀNOA IN PARTIAL FULFILLMENT OF THE REQUIREMENTS FOR
THE DEGREE OF

DOCTOR OF PHILOSOPHY

IN

GEOLOGY AND GEOPHYSICS

December 2019

By

Alyssa Natasha Anderson

Dissertation Committee:

James Foster, Chairperson

Sarah Fagents

Neil Frazer

Bridget Smith-Konter

Steven Businger

ACKNOWLEDGEMENTS

I wahi waihona 'ike no nā mamo o Hawai'i nei

I would like to thank the University of Hawai'i at Mānoa, the School of Ocean and Earth Science and Technology, the Department of Earth Sciences, and the Hawai'i Institute of Geophysics and Planetology. It has been an honor to do my graduate work here. Thank you to my committee members. James Foster, thank you for seeing potential in me by offering a position in the Pacific GPS Facility, and for sharing your knowledge of geodesy over the years. Sarah Fagents, thank you for the opportunity to work with you on lava flows, and providing me with resources and guidance to succeed. Neil Frazer, your patient explanations were extremely helpful in navigating unfamiliar concepts. Bridget Smith-Konter, your positivity and kind words of advice and support were always appreciated. Steven Businger, thank you for your encouragement to continue in science.

To the faculty members in the department, thank you. I have learned so much from the classes you have taught and the encouragement you have provided. John Sinton and Scott Rowland, thank you for introducing me to Hawaiian geology. Stephen Martel, thank you for your mentoring when I was the Teaching Assistant for your structural geology class during my first semester in graduate school, and your constant help with stress equations during my last semester. Thank you to Scott, Henrietta, and Leona for being great mentors when I was your Teaching Assistants. Also thank you Stephen Baloga for your gracious input, support, and yellow note book pages.

Thank you to my fellow graduate students and researchers for the friendships, supportive conversations, and companionship on the field trips in Hawai'i and beyond. Thank you to RCF and HIGP support for helping with computer problems, and the administrative staff for your continuous hard work and organization: Susan, Lily, Vi, Leona, Evelyn, Grace and others.

To the organizations that have helped support me: Thank you to the Graduate Student Organization for providing a travel grant for field work in New Zealand for the Explosive Volcanism course led by Bruce Houghton, whose guidance was always appreciated. Thank you to the Geological Society of America On to the Future Program, Barb Bruno, and Heidi Kane for providing a travel scholarship to attend the Phoenix, Arizona conference. Thank you to Maile Mentoring for allowing me to be part of your program and for providing funding to attend the SACNAS conference. Thank you also to USGS Hawaiian Volcano Observatory for your help over the years, and Asta Miklius for your insight to and help with Kīlauea deformation.

Thank you to my dear family and friends, you are cherished. To Hālau Hula Ka Lehua Tuahine and Kumu Ka'ilihiwa, thank you for your aloha, wisdom, and opportunities to learn and share the stories of Hawai'i in this lineage.

Mahalo piha iā 'oukou a pau, e nā kūpuna, nā mākua, a me nā kumu no ka hā'awi 'ana mai ia 'u i ka 'ike, ka ikaika, a me ka na'auao i ko'u ola. Mahalo ho'i i ke kāko'o a me ke kōkua 'ana mai ia 'u. Mahalo nui iā 'oe, e Lalepa, nāu nō i a'o mai i nā mo'olelo o nā kūpuna. 'O kekahi mea ko'iko'i loa o kou a'o 'ana mai, ko'u hiki i kēia manawa ke hō'ike i ka 'ikena i ia mau mo'olelo o ka 'āina me ka 'ikena o ka Hawai'i, a me ka pilina o nā mea 'elua.

Finally, this work is for the people of Hawai'i. The geologic history of Hawai'i is woven with the history of the people of Hawai'i, these stories and histories continue vibrantly.

Ke aloha nō,

Alyssa

ABSTRACT

Kīlauea volcano is located on the southeastern side of the island of Hawai‘i and is one of the most active volcanoes in the world. Magma moves underground to supply eruptions at the summit or along the rift zones, causing deformation at the surface. Volcano monitoring at Kīlauea has provided the excellent datasets on which the studies presented here are based. The first study, described in Chapter 2, focuses on a common and relatively small style of deformation recorded in surface deformation data. These events exhibit deflation and inflation at the summit, and are considered to be caused by changes in magma reservoir pressure below the caldera. We used geophysical and statistical analyses to compare three different models for the cause of these events, finding a complex relationship between the magma reservoirs. Summit and eruptive activity at Kīlauea changed drastically in 2018, when a series of major caldera collapse events occurred as magma drained from the summit to feed a fissure eruption in the lower East Rift Zone. The second study, described in Chapter 3, investigates the processes driving these collapse events using a force balance approach. As pressure decreases due to magma withdrawal, stresses acting on the caldera faults increase until failure occurs and the caldera rock collapses. We use a crustal deformation model to predict the pressure changes in the deflating magma reservoir, analytical equations to determine the stress distribution on the caldera faults, and a force balance configuration to relate the resulting pressure changes and stresses. Our analysis suggests that the strength of the fault is likely to be the factor controlling failure during the collapse events. The final study, described in Chapter 4, turns our attention to the 2018 eruption in the lower East Rift Zone, which produced channelized lava flows that were well observed by video monitoring. We develop and apply a thermal model to examples of lava surface crust disruption due to changes in channel width observed in images of these lava flows. The primary result is that narrowing lava channels increase the surface area of exposed incandescent lava, causing enhanced cooling, which can ultimately influence the final length of the flow. These three studies provide new insight to Kīlauea’s volcanic processes and contribute to a better understanding of volcanic hazards for communities at risk.

TABLE OF CONTENTS

ACKNOWLEDGEMENTS.....	iii
ABSTRACT.....	v
TABLE OF CONTENTS	vi
TABLE OF TABLES.....	ix
TABLE OF FIGURES	x
LIST OF ABBREVIATIONS AND SYMBOLS	xii
COMMENTS ON THE PREPARATION OF HAWAIIAN TEXT.....	xiv
CHAPTER 1. INTRODUCTION.....	1
1.1 Dissertation overview	1
1.2 Hawaiian volcanoes.....	2
1.3 Kīlauea volcano.....	2
CHAPTER 2. IMPLICATIONS OF DEFLATION-INFLATION EVENT MODELS ON KĪLAUEA VOLCANO, HAWAI‘I.....	8
Abstract.....	8
2.1. Introduction.....	9
2.2. Background	11
2.2.1 Existing model of Kīlauea summit	11
2.2.2 Previous deformation modeling.....	12
2.2.3 Deflation-inflation events.....	12
2.3. Motivation: Implications of DI model scenarios.....	13
2.4. Data.....	16
2.5. Predicted tilt from modeling geodetic sources.....	18
2.5.1 Magma reservoir deformation during DI events	18

2.5.2 Deformation for volume increase in SCR and decrease in HMMR	21
2.6. Selected DI event observations	24
2.6.1 Characterizing events.....	24
2.6.2 Modeling events and model comparison.....	27
2.7. Discussion	30
2.8. Conclusions.....	33
CHAPTER 3. A FORCE BALANCE PERSPECTIVE OF THE 2018 KĪLAUEA VOLCANO SUMMIT COLLAPSE EVENTS	35
Abstract.....	35
3.1. Introduction.....	36
3.2. Background	36
3.2.1 Kīlauea volcano	36
3.2.2 The 2018 Kīlauea summit collapse.....	38
3.2.3 Caldera collapse dynamics	40
3.3. Data.....	40
3.3.1. GPS network.....	40
3.3.2. Defining a representative GPS event.....	42
3.4. Model.....	44
3.4.1. Force balance configuration	44
3.4.2. Magma pressure.....	48
3.4.3. Stress distribution	51
3.5. Results.....	53
3.6. Relating stress and magma pressure.....	55
3.7. Discussion and conclusions.....	56

CHAPTER 4. EFFECTS OF VARIATIONS IN LAVA CHANNEL GEOMETRY ON FLOW DYNAMICS, EVOLUTION, AND LENGTHS	60
Abstract.....	60
4.1. Introduction.....	61
4.2. Background	62
4.3. Observations of active flows from Kīlauea, 2018	66
4.3.1 Methods of data analysis.....	66
4.3.2 Selected features	67
4.4. Model for flow evolution.....	71
4.4.1 Model background.....	71
4.4.2 Model for channel width variations.....	78
4.5. Results.....	87
4.6. Discussion	92
4.7. Conclusions	97
CHAPTER 5. CONCLUSIONS	98
APPENDIX: CESSATION TEMPERATURE	100
REFERENCES	103

TABLE OF TABLES

Table 2.1.....	30
----------------	----

TABLE OF FIGURES

Figure 1.1.....	3
Figure 1.2.....	4
Figure 1.3.....	6
Figure 2.1.....	10
Figure 2.2.....	14
Figure 2.3.....	17
Figure 2.4.....	20
Figure 2.5.....	22
Figure 2.6.....	23
Figure 2.7.....	25
Figure 2.8.....	26
Figure 2.9.....	29
Figure 3.1.....	37
Figure 3.2.....	39
Figure 3.3.....	41
Figure 3.4.....	43
Figure 3.5.....	45
Figure 3.6.....	49
Figure 3.7.....	50
Figure 3.8.....	52
Figure 3.9.....	54
Figure 3.10.....	57
Figure 4.1.....	64
Figure 4.2.....	68
Figure 4.3.....	70
Figure 4.4.....	72
Figure 4.5.....	75
Figure 4.6.....	76
Figure 4.7.....	77

Figure 4.8.....	82
Figure 4.9.....	83
Figure 4.10.....	86
Figure 4.11a.....	88
Figure 4.11b.....	89
Figure 4.11c.....	90
Figure 4.11d.....	91
Figure 4.12.....	93
Figure 4.13.....	96

LIST OF ABBREVIATIONS AND SYMBOLS

<u>Abbreviations/Symbols</u>	<u>Definitions</u>
C_p	specific heat capacity of lava, J kg ⁻¹ K ⁻¹
dx	length of control volume, m
F_f	frictional force, N
F_{litho}	lithostatic force, N
F_m	magma force, N
F_{net}	net force, N
$F_{\Delta P}$	magma pressure force, N
f	fraction of exposed lava core
G	shear modulus, Pa
g	acceleration due to gravity, m s ⁻²
HMMR	Halema‘uma‘u reservoir
h	reservoir depth, m
	lava flow thickness, m
L	lava flow length, m
m	mass of the control volume, kg
P	magma pressure, Pa
P_{litho}	lithostatic pressure, Pa
P_m	magma pressure
Q	lava volume flow rate per unit channel width, m ² s ⁻¹
r	reservoir radius, m
R	radial coordinate
R_1	secondary radial coordinate
R_2	secondary radial coordinate
SCR	south caldera reservoir
t	time, s
T_o	initial lava core temperature, K
T_{core}	temperature of lava core, K

u	velocity of the flow, m s^{-1}
V	volume, m^3
w	width of flow, m
x	horizontal axis distance along the flow, m
y	vertical axis
y_{crit}	distance from center of channel to incandescent margin, m
ε	lava emissivity
θ	angular coordinate angle through which column rotates (time dependent)
θ_I	secondary angular coordinate
θ_l	secondary angular coordinate
μ	dynamic viscosity of lava (constant), Pa s
ν	Poisson's ratio kinematic viscosity of lava, Pa s
ρ	density, kg m^{-3}
σ	Stefan-Boltzmann constant, $5.670373(21) \times 10^{-8} \text{ W m}^{-2} \text{ K}^{-4}$
σ_x	horizontal normal stress, Pa
σ_{xlith}	horizontal lithostatic stress, Pa
σ_{xtot}	total horizontal stress, Pa
σ_y	vertical normal stress, Pa
σ_{ylith}	vertical lithostatic stress, Pa
σ_{ytot}	total vertical stress, Pa
τ	shear stress, Pa
τ_{crit}	critical shear stress, Pa

COMMENTS ON THE PREPARATION OF HAWAIIAN TEXT

*Pa‘i ‘ia ma ka pela Hawai‘i i ho‘onohonoho ‘ia e ke kōmike pela o ka ‘Ahahui
‘Ōlelo Hawai‘i o 1978.*

The spelling of Hawaiian terms in this work is in accordance with standardized Hawaiian orthography given by the recommendation of the ‘Ahahui ‘Ōlelo Hawai‘i spelling project of 1978.

CHAPTER 1. INTRODUCTION

1.1 Dissertation overview

This dissertation investigates volcanic processes observed at Kīlauea volcano, Hawai‘i, with an emphasis on the extraordinary 2018 summit collapse and rift eruption. Here in the introductory chapter, a brief background is provided to give the geologic setting of the Hawaiian archipelago and Kīlauea volcano. Chapter 2 investigates a prominent style of deformation observed at Kīlauea summit, deflation-inflation (DI) events. These events are best recorded in the summit tiltmeter network, which detects tilt of the ground surface at microradian scales, and can be used to constrain the location and dimensions of the summit reservoirs [*Cervelli and Miklius, 2003; Poland et al., 2014; Anderson et al., 2015*]. Proposed models for the cause of DI events are investigated using geodetic models and statistical analyses for model comparison.

Chapters 3 and 4 focus on two separate, yet related, aspects of the 2018 Kīlauea summit collapse and rift eruption. Chapter 3 focuses on the caldera collapse events between May 29 and August 2 when the GPS observations settled into a consistent, nearly daily pattern. A force balance approach is used to address the relationship between magma pressure of the draining reservoir and shear stresses on the caldera ring faults. Understanding how these parameters are connected provides insight to the mechanisms triggering caldera collapse. Our results show that shear stresses and magma pressure are inversely related by a constant of proportionality dependent on the geometry of the magma reservoir. Analysis of the stresses suggests that failure propagates along the fault over time, and that fault strength is the main factor controlling collapse.

Chapter 4 shifts attention from the summit of Kīlauea to the lower East Rift Zone (ERZ) eruption, which was likely being supplied by the draining of magma that caused the summit collapse events. Aerial video monitoring of the active channelized lava flows that developed provided an excellent dataset that encouraged this study of lava flow surface crust disruption. These flows exhibited variations in channel width and direction that affected their radiative heat loss. Our theoretical heat loss model suggests that narrowing channel widths disrupt surface crust

at the flow margins, causing enhanced cooling which can significantly influence the core temperature of the flow, and ultimately the distance that it can travel. Chapter 5 summarizes the dissertation conclusions and possibilities for future work.

1.2 Hawaiian volcanoes

The Hawaiian archipelago is a relatively linear chain of volcanic islands, atolls, and seamounts spanning ~2400 km in the Pacific Ocean at the southeastern end of the Hawaiian-Emperor chain (Fig. 1.1). Islands form as the Pacific plate passes slowly over a mantle plume, resulting in typically older and more weathered islands to the northwest and younger, volcanically active islands to the southeast [Wilson, 1963, Decker, 1987; Sharp and Clague, 2006]. In the initial growth of an island, magma rises from depth through the lithosphere into shallow reservoirs where it is stored or transported before eruption [Tilling and Dvorak, 1993]. The stages of island growth consist of an initial submarine stage that begins on the ocean floor eventually emerging above sea level, a subaerial shield building stage as eruptions continue above the ocean surface, erosion, weathering, formation of coastal reefs, rejuvenation volcanism, and finally an atoll stage that sinks below sea level to become a seamount [Stearns, 1946; Macdonald et al., 1983; Moore and Clague, 1992]. Not all volcanic islands pass through every growth stage, but the order of the cycle is generally followed.

1.3 Kīlauea volcano

The southeastern end of the Hawaiian archipelago consists of eight main volcanic islands. From west to east, and oldest to youngest, they are Ni‘ihau, Kaua‘i, O‘ahu, Moloka‘i, Lāna‘i, Kaho‘olawe, Maui, and Hawai‘i (Fig. 1.1) [Macdonald et al., 1983]. The island of Hawai‘i is comprised of two submarine shield volcanoes, Māhukona, the oldest, and Lō‘ihi, the youngest and still in the submarine shield building stage, and five subaerial volcanoes, which from oldest to youngest are Kohala, Maunakea, Hualālai, Maunaloa, and Kīlauea [Moore and Clague, 1992] (Fig. 1.2). Kīlauea volcano is in the shield building stage; it is situated on the southeastern flank of Maunaloa Volcano (Fig. 1.3), and is one of the most active volcanoes in the world. The magmatic system interaction between Kīlauea and Maunaloa is complex and it remains unclear how their relationship affects eruptive activity [Miklius and Cervelli, 2003; Trusdell, 2011].

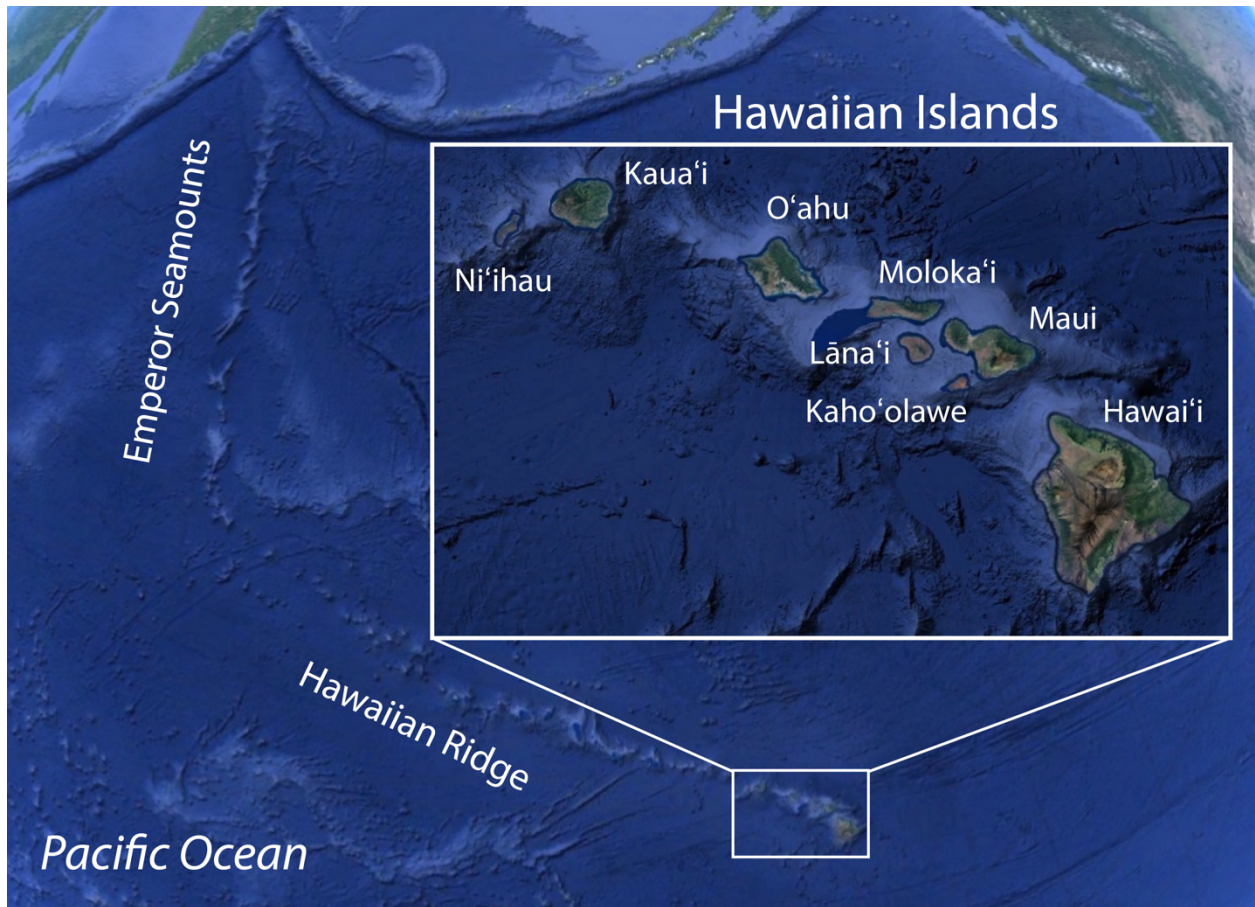


Figure 1.1. Google Earth images of the Hawaiian-Emperor seamount chain and the Hawaiian Islands. The eight main Hawaiian islands from oldest to youngest are Ni'ihau, Kaua'i, O'ahu, Moloka'i, Lāna'i, Kaho'olawe, Maui, and Hawai'i.

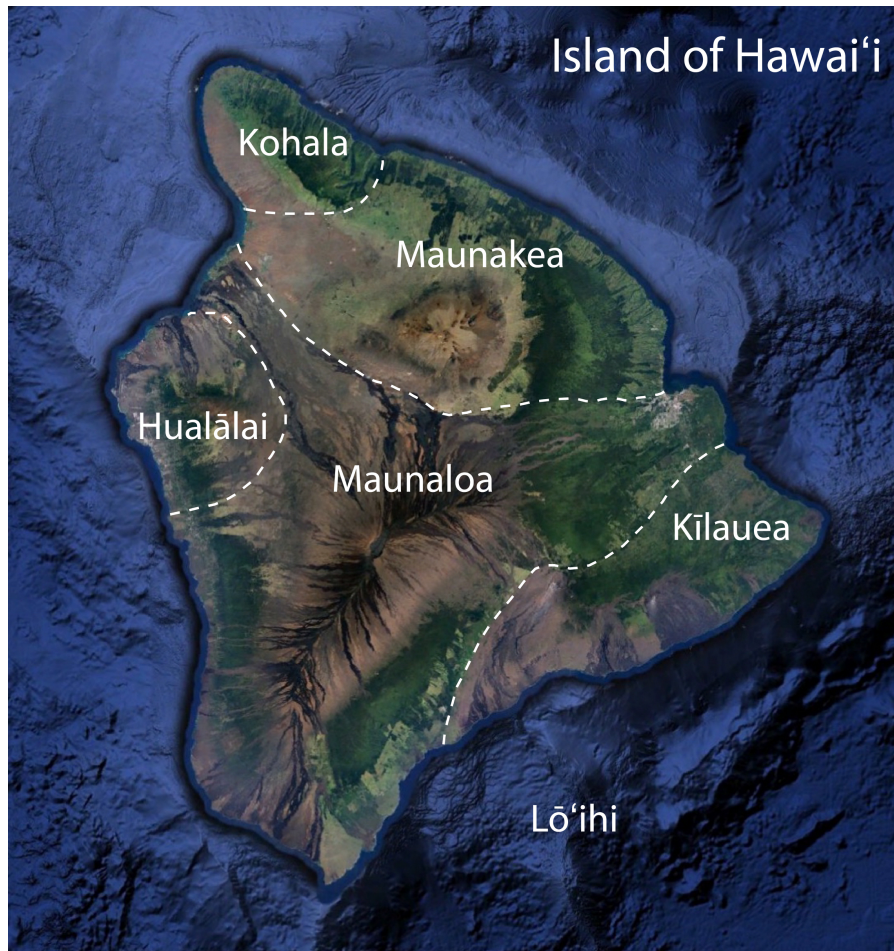


Figure 1.2. Google Earth image of the island of Hawai'i. The five subaerial volcanoes that comprise the island are from oldest to youngest, Kohala, Maunakea, Hualālai, Maunaloa, and Kīlauea. Lō'ihī is a submarine volcano.

Kīlauea is supplied with basaltic magma that rises from the upper mantle to shallow (1–4 km depth) reservoirs, where it is stored, erupted, or transported along the rift zones [e.g., *Eaton and Murata*, 1960; *Fiske and Kinoshita*, 1969; *Wright*, 1984; *Baker and Amelung*, 2012; *Poland et al.*, 2014; *Wright and Klein*, 2014]. Structurally Kīlauea is characterized by a main summit caldera, the Southwest and East Rift Zones, and a south flank defined by a large fault system resulting in slow seaward motion (Fig. 1.3). There are considered to be two long term magma reservoirs at the summit, one south of the caldera at ~3 km depth, and another below the Halema‘uma‘u crater within the caldera at ~1 km depth [*Tilling and Dvorak*, 1993; *Pietruszka and Garcia*, 1999; *Cervelli and Miklius*, 2003; *Poland et al.*, 2014; *Anderson et al.*, 2015]. Eruptions have occurred primarily at the summit or along the rift zones, and are likely fed by conduits connected to the summit storage reservoirs [*Holcomb* 1987; *Cervelli and Miklius*, 2003]. The correlation of pressure perturbations at the summit and along the ERZ suggests that the two systems are linked by a relatively well-established plumbing system [*Cervelli and Miklius*, 2003].

Kīlauea is a well-studied and monitored volcano with dense networks of geophysical instrumentation, including tiltmeter and Global Positioning System (GPS) networks, that have provided a foundation for the work presented here [*Decker et al.*, 2008; *Kauahikaua and Poland*, 2012]. Unprecedented activity occurred recently (in 2018, one year prior to the completion of this dissertation manuscript) at Kīlauea when it experienced the largest summit caldera collapse and eruptive activity at the lower ERZ in ~200 years [*Neal et al.*, 2019]. The Pu‘u ‘Ō‘ō vent along the ERZ, which had been erupting almost continuously since 1983, collapsed at the end of April after an accumulation of magma caused an over pressurization of the system. This led to the opening of 24 eruptive fissures in the lower ERZ producing lava fountains feeding channelized lava flows that ultimately reached the ocean [*Neal et al.*, 2019]. Meanwhile at the summit, the lava lake that had existed within Halema‘uma‘u crater since 2008 drained, causing nearly daily caldera collapse and explosion events between May and August, punctuated by Mw > 5 earthquakes. The strong monitoring networks in place at the time of the activity resulted in huge datasets that provide many opportunities for thorough investigations, some of which will be highlighted in this dissertation. Activity ended in early August 2018, and Kīlauea is currently not

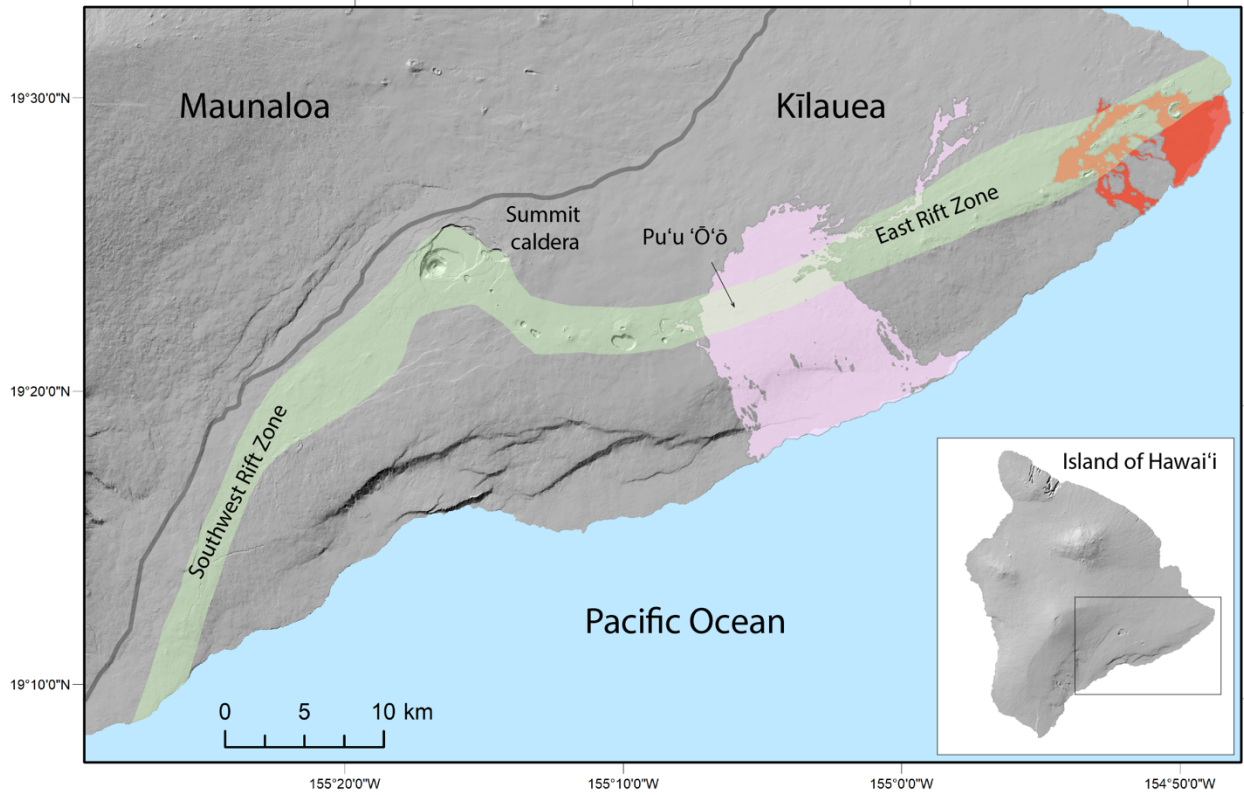


Figure 1.3. Map showing Kīlauea Volcano with major structural features and lava flows erupted 1983–2018 from Pu'u 'Ō'ō vent (pink), and in 2018 from the lower East Rift Zone (red). Bottom right: Map of island of Hawai'i showing location of Kīlauea.

erupting. A water pond has developed at the bottom of the new Halema‘uma‘u crater within the summit caldera. The water pond appeared near the end of July 2019 and continues to rise at the writing of this work.

CHAPTER 2. IMPLICATIONS OF DEFLATION-INFLATION EVENT MODELS ON KĪLAUEA VOLCANO, HAWAI‘I

Submitted for review as:

Anderson, A.N., Foster, J.H. and Frazer, N. (in review) Implications of Deflation-Inflation Event Models on Kīlauea Volcano, Hawai‘i. Submitted to Journal of Volcanology and Geothermal Research.

Abstract

Surface deformation of volcanic areas can reveal information about subsurface magma reservoirs and how magma is transported between them, which is an important part of volcano monitoring for hazard mitigation. One prominent style of deformation observed at Kīlauea volcano, Hawai‘i, is episodic deflation-inflation (DI) events, which are recorded in surface deformation data and characterized by deflation of the summit region over hours to days followed by rapid re-inflation. The exact cause of DI events is unknown; however, a commonly proposed explanation is that a temporary blockage occurs in the conduit connecting the south caldera magma reservoir to the shallower Halema‘uma‘u reservoir, thus interrupting the influx of magma. This model is investigated by testing the hypothesis that during the deflationary phase of a DI event, the volume of magma blocked from reaching the Halema‘uma‘u reservoir is added to the south caldera reservoir. Using a mass balance approach and geodetic modeling, the expected deformation (tilt) pattern was predicted for the reservoirs and compared to tilt observations from 16 large (>4 μ rad magnitude) DI events between 2010 and 2012. While predicted tilts due to inflation from the south caldera reservoir are strong enough to potentially be detected, they disagree with tilt observations. Selected DI events show that tilt vectors change in both magnitude and azimuthal direction over the course of deflation, resulting in a complex deformation pattern inconsistent with the simple model of a blockage between two chambers.

2.1. Introduction

Episodic deformation caused by pressure perturbations within a volcano's magmatic system can reveal important information about magma storage and transport necessary to volcano monitoring for hazard mitigation [e.g., *Voight et al.*, 1998; *Yamashina et al.*, 1999 *Cervelli and Miklius*, 2003; *Anderson et al.*, 2010, 2015; *Genco and Ripepe*, 2010; *Poland et al.*, 2014]. At Kīlauea volcano, Hawai'i, episodic deformation has been related to eruptive activity [*Swanson et al.*, 1979; *Wolfe et al.*, 1987], and investigated through modeling of geodetic deformation sources in order to make interpretations about the shallow magmatic system configuration [*Dvorak and Okamura*, 1983; *Dvorak and Dzurisin*, 1997]. In the 1990s a new type of episodic deformation, summit deflation-inflation (DI) events, was observed [*Heliker and Mattox*, 2003] and has since been a frequent signal associated with the summit region, recorded especially well by the summit tiltmeter network. A common hypothesis for these events is that a blockage occurs within the magmatic plumbing system, temporarily cutting off the supply of magma into the shallow summit reservoir while magma continues to exit through a conduit to the eruption site [*Cervelli and Miklius*, 2003; *Anderson et al.*, 2015]. This results in the summit deflation. DI events are most commonly associated with activity in the shallow Halema'uma'u reservoir (HMMR), but their relationship with the deeper south caldera reservoir (SCR) is not often discussed in detail. The SCR is thought to be directly connected to the HMMR, which implies that the SCR should also be affected by these events. In a comprehensive study on DI events, *Anderson et al.* [2015] note that while DI events have not previously been known to manifest in the SCR, potential deformation related to the SCR during the events could go undetected, and that certain types of events could be caused by blockages deeper within the magmatic system.

The work presented here investigates the role of the SCR during DI events. This will provide insight to the cause of DI events and therefore the magmatic plumbing system dynamics of Kīlauea. We explore the implications of the model for DI events proposed by *Cervelli and Miklius*, [2003]. Under the assumptions of this model, we use a geodetic model to determine the expected extent of SCR related tilt deformation during DI events, and test if that deformation is

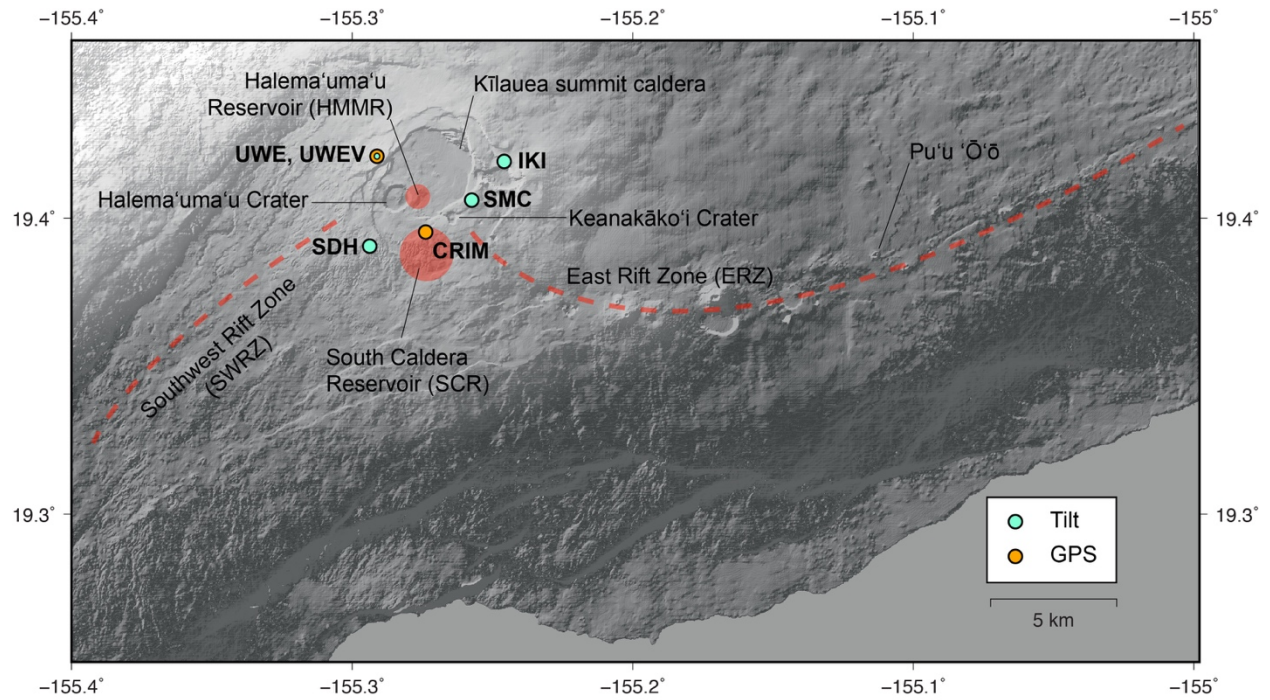


Figure 2.1. Kīlauea volcano with locations of instruments and geologic features discussed in this study. Size and location of reservoirs are approximate.

detectable over the contribution from the HMMR. We compare model predictions with tilt observations for 16 large (>4 μ rad magnitude) DI events that occurred between January 9, 2010 and January 5, 2012.

2.2. Background

2.2.1 Existing model of Kīlauea summit

Kīlauea volcano (Fig 2.1) is located on the island of Hawai‘i on the south flank of Mauna Loa volcano, and is characterized by a main summit caldera, the Southwest Rift Zone (SWRZ), and East Rift Zone (ERZ) [Holcomb, 1987; Fisk et al., 1993]. The magmatic plumbing model consists of magma being supplied from depth and rising to one or more long-term summit magma reservoirs [Eaton and Murata, 1960; Tilling and Dvorak, 1993]. The SCR is generally considered to be the main storage area and location of long-term deformation, sitting at a depth of ~ 3 km below the southern caldera region [Delaney et al., 1990, 1993; Cervelli and Miklius, 2003; Baker and Amelung, 2012]. The Halema‘uma‘u magma reservoir (HMMR) is a shallower and smaller storage area located in the region east to southeast of the Halema‘uma‘u crater that existed prior to May 2018, as suggested by studies of deformation [Fiske and Kinoshita, 1969; Dvorak and Okamura, 1983; Johnson, 1992; Cervelli and Miklius, 2003], gravity, [Dzurisin et al., 1980; Johnson et al., 2010] and seismicity [Ohminato et al., 1998; Almendros et al., 2002; Chouet et al., 2010; Dawson et al., 1999; Battaglia et al., 2003; Okubo et al., 2014]. A third recognized storage area is beneath the Keanakāko‘i crater zone. This region has been found to be periodically active in the last few decades [Dvorak and Okamura, 1983; Klein et al., 1987; Yang et al., 1992; Poland et al., 2014] with historic eruptive activity [Peterson and Moore, 1987; Duffield et al., 1982], but its connection to the other zones is unclear. Storage areas have also been proposed in the SWRZ with a connection to the summit [Holcomb, 1987; Fisk et al., 1993; Myer et al., 2008; Baker and Amelung, 2012; Poland et al., 2012]. A magmatic connection exists from the summit to the ERZ based on the correlation of summit draining to eruptive activity along the ERZ, where Kīlauea had been erupting almost continuously mainly from Pu‘u ‘Ō‘ō between 1983 and May 2018 [Swanson et al., 1979; Wolfe et al., 1987; Owen et al., 2000; Heliker and Mattox, 2003; Poland et al., 2009b; Montgomery-Brown et al., 2010; Baker and Amelung, 2012; Lundgren et al., 2013]. The exact nature and location of the connection between

the summit and the ERZ is uncertain. The correlation of pressure perturbations at HMMR and slightly later at Pu‘u ‘Ō‘ō [Cervelli and Miklius, 2003] indicate a relatively direct connection between the HMMR and ERZ, while seismic observations indicate a deeper connection [Klein et al., 1987].

2.2.2 Previous deformation modeling

Previous studies have used a variety of geodetic datasets to model the location, size, and depth of the main summit magma reservoirs at Kīlauea [Cervelli and Miklius, 2003; Baker and Amelung, 2012; Poland et al., 2012]. Cervelli and Miklius [2003] suggested a shallow source east of Halema‘uma‘u crater 500–700 m deep based on four tilt events (2000–2002), and a deeper source ~3.5 km deep, based on repeated leveling and GPS data (1996–2000). Anderson et al. [2015] used inverse modeling of tilt data for ~500 DI events between 2000 and 2013 and determined they were caused by pressure perturbations in a source east of Halema‘uma‘u crater with a volume approximately 1 km³ (radius between 500 m and 1000 m) no deeper than ~1500 m. Baker and Amelung [2012] used interferometric synthetic aperture radar data from 2000 to 2008 to model a spherical source northeast of Halema‘uma‘u crater ~2 km deep, and in the south caldera region, a penny-shaped crack sill [Fialko et al., 2001] at a depth of 2.7–4.7 km with a radius of 1.3–4 km. Poland et al. [2012] used radar interferometry data to model a point source 2.9 km deep south of the caldera and a rectangular sill ~4 km deep in the Southwest Rift zone region for the period 2003 to 2007. In a review paper, Poland et al. [2014] proposed a general model of the summit that combined existing geodetic models that agrees with petrologic, geophysical, and geologic data. This model included a shallow reservoir 1–2 km below the center of the caldera near Halema‘uma‘u, a deeper source ~3 km below the south caldera, and a magma storage area beneath Keanakāko‘i crater that is occasionally active. Because extensive work has already been done to model these reservoirs, we use previously estimated reservoir parameters for our models.

2.2.3 Deflation-inflation events

DI events are characterized by radial deflation of the summit area lasting hours to days, followed by a nearly instantaneous transition to rapid inflation, with deformation appearing

radially outwards from a point within the caldera region east and southeast of Halema‘uma‘u crater. While the exact processes responsible for DI events are unclear, it is assumed that the deflation signals are caused by outflux from the summit temporarily exceeding magma input [Anderson *et al.*, 2015]. DI events can propagate down the ERZ after occurring at the summit, and have been recorded as matching, time-delayed signals at a tiltmeter located at Pu‘u ‘Ō‘ō, implying a pressure connection between the summit and ERZ vent [Cervelli and Miklius, 2003].

DI pressure changes measured by tiltmeters were also found to be correlated with the height of the level of the summit lava lake open between 2008 and 2018 within Halema‘uma‘u crater [Orr *et al.*, 2012; Patrick *et al.*, 2013; Patrick and Orr, 2013]. Lava lake surface heights at Kīlauea have been related to deformation and used as a pressure gauge for the associated magma reservoir [Tilling, 1987; Johnson, 1992; Denlinger, 1997; Segall *et al.*, 2001]. Anderson *et al.* [2015] used the tilt and lava lake level relationship to estimate the relationship between volume and pressure changes, and to refine the geometry of the summit magma reservoir. Seismic tremor has also been associated with DI events [Cervelli and Miklius, 2003, Dawson *et al.*, 2004] and other tilt-signals [Ohminato *et al.*, 1998].

2.3. Motivation: Implications of DI model scenarios

Pressure perturbations causing DI events have been attributed to a temporary blockage that interrupts the influx of magma within the shallow magmatic system [Cervelli and Miklius, 2003; Anderson *et al.*, 2015]. The location of the blockage and the configuration of magma pathways will influence the resulting pressures in the magma reservoirs. Figure 2.2 illustrates four such scenarios and their implications for the system. In all the configurations, magma is supplied from depth to the SCR where it is then transported through a conduit to the HMMR. Magma can drain to the ERZ from either the HMMR (Fig. 2.2A and 2.2B) or from the SCR (Fig. 2.2C and 2.2D). For each of these cases, the blockage can occur between the conduit connecting the SCR and the HMMR (Fig. 2.2A and 2.2C), or between the SCR and its magma supply from depth (Fig. 2.2B and 2.2D).

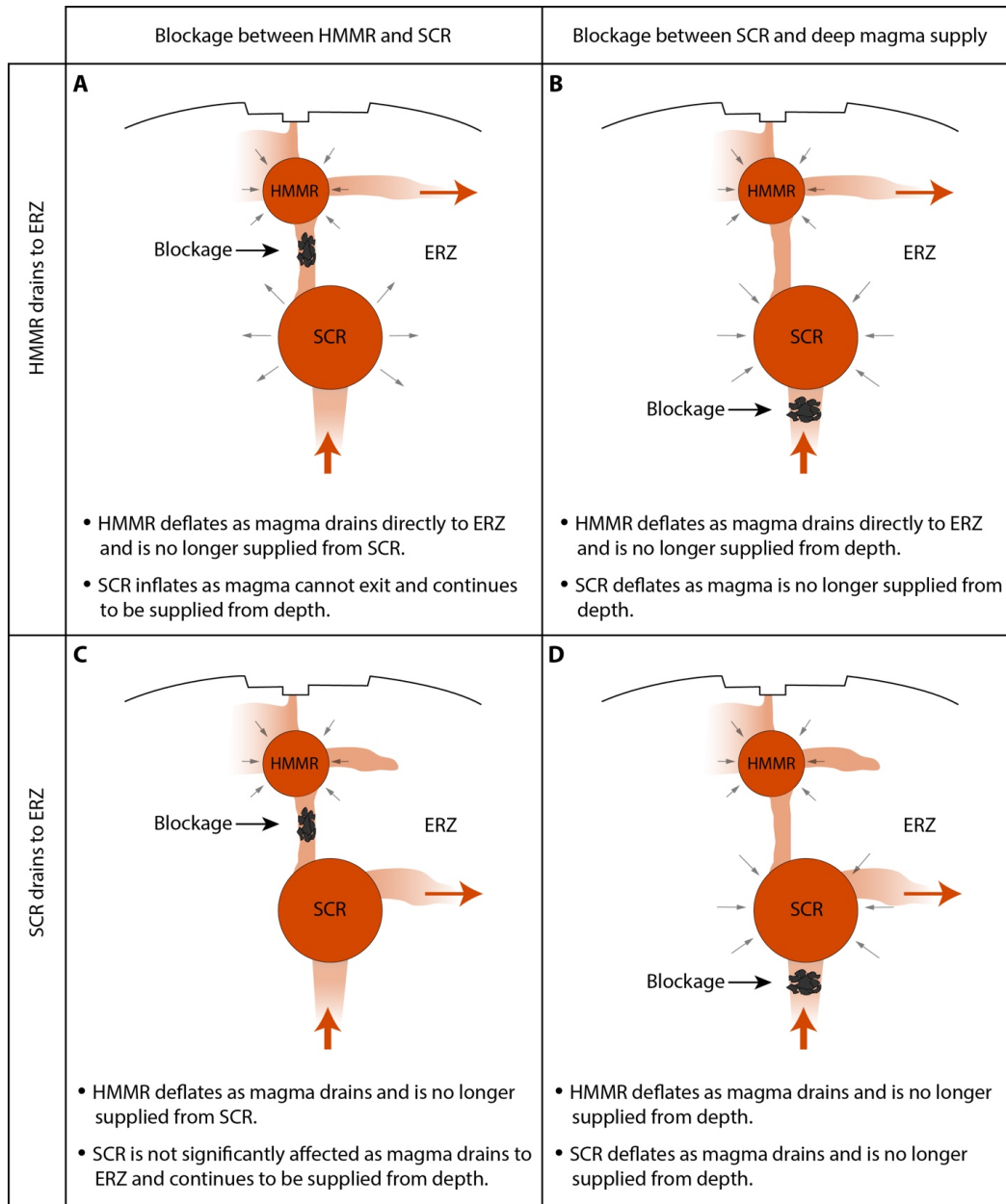


Figure 2.2. Schematic cross sections of Kīlauea’s magmatic plumbing system showing locations of magma pathways and blockages and their implications on reservoir volumes during DI events. Relative sizes and distances are not to scale. HMMR = Halema‘uma‘u reservoir, SCR = south caldera reservoir, ERZ = East Rift Zone.

The summit configuration proposed by *Poland et al.* [2014] does not include a conduit directly connecting the HMMR to the ERZ, and instead, based on seismic data, favors a connection from the SCR to the ERZ (Fig. 2.2C and 2.2D). If the blockage occurs in the conduit between the reservoirs, then magma in the HMMR should be able to rapidly drain somewhere other than the ERZ when its supply is cut off, producing the deflationary signal. If the blockage occurs deeper below the SCR, then pressure changes during DI events would be expected to be the same in both reservoirs for both scenarios shown in Figure 2.2B and 2.2D.

The two options for the ERZ connection (Fig. 2.2A and 2.2C) were discussed by *Cervelli and Miklius* [2003] in relation to DI events caused by a blockage between the reservoirs. They support a direct connection from the HMMR to the ERZ (Fig. 2.2A and 2.2B) because of the correlation between pressure changes in the HMMR and slightly later at Pu'u 'Ō'ō. In this scenario, the pressure head in HMMR continues to drive magma outflux, causing rapid deflation at HMMR as its volume decreases. The deflation is expected to follow an exponential-like decline as the falling pressure differential drives a proportionately lower flux rate [e.g. *Lengliné et al.*, 2008]. The removal of magma continues until the HMMR pressure head is too low to overcome the resistance to flow. At some point the blockage is breached or removed, and the influx of magma from the SCR resumes. As HMMR is now at a lower pressure than SCR there is a rapid re-inflation until the pressure levels reach an equilibrium [e.g. *Haney, et al.*, 2016].

One key and relatively unexplored corollary for this model is the impact “upstream” of the blockage. If the blockage occurs in the connection between SCR and HMMR such that magma cannot leave the SCR by any other means, and the small pressure increase does not exceed the pressure head driving magma from depth into the SCR, then some “blocked” magma, similar to the volume lost from HMMR, would be expected to be added to the SCR. This corollary therefore predicts that the volume (and therefore pressure) within the SCR would increase during a DI event (Figure 2.2A). The motivation for this work comes from the implications of this particular scenario.

In this study we test the model that DI events are caused by a blockage between the SCR and the HMMR under conditions that magma supply is constant from depth to SCR over DI time-scales, magma compressibility is small enough to be ignored [Anderson *et al.*, 2015], and magma must flow from SCR to HMMR and does not leave the system from the SCR by any other means (i.e., magma does not flow directly to ERZ, SWRZ or deep storage). We follow the assumption of Cervelli and Miklius [2003] and Anderson *et al.* [2015] that magma is lost from the HMMR to the ERZ or some part of the summit magma system, while acknowledging that this connection is not well understood. If this model is correct and the above conditions are met, then a volume of magma similar in magnitude to that lost from the HMMR during a DI event should be added to SCR. Thus we test the hypothesis that a volume increase in SCR during the deflationary phase of a DI event produces detectable tilt deformation at the surface.

In the following sections we test for SCR inflation using the approach shown by the flow chart in Figure 2.3. First, the tilt is predicted for a given volume increase in SCR using an analytical geodetic spherical source model [McTigue, 1987] under a range of SCR depths and radii. The predicted tilt magnitudes will reveal whether some combination of reservoir depth and radius produces detectable signals. Second, the tilt is predicted for a simultaneously deflating HMMR and inflating SCR using two geodetic sources representing each magma reservoir with a predefined depth and radius. This will give the expected deformation pattern for the scenario shown in Figure 2.2A. Using this same geodetic model, tilt data are analyzed from the 16 largest DI events between 2000 and 2012. An algorithm is used to search for the reservoir volume changes that best fit the observations. Three different models are tested, and tilt predictions are compared with the observations. Finally, we perform statistical analysis for model comparison. In our analysis we calculate the overall difference in volume from onset to end time during the event, rather than the nature of the kinematic evolution.

2.4. Data

DI events are best recorded by the summit tiltmeter network (Fig 2.1), operated by the U.S. Geological Survey (USGS) Hawaiian Volcano Observatory (HVO) [Cervelli and Miklius, 2003; Anderson *et al.*, 2015], but other, generally larger, events are also recorded in global

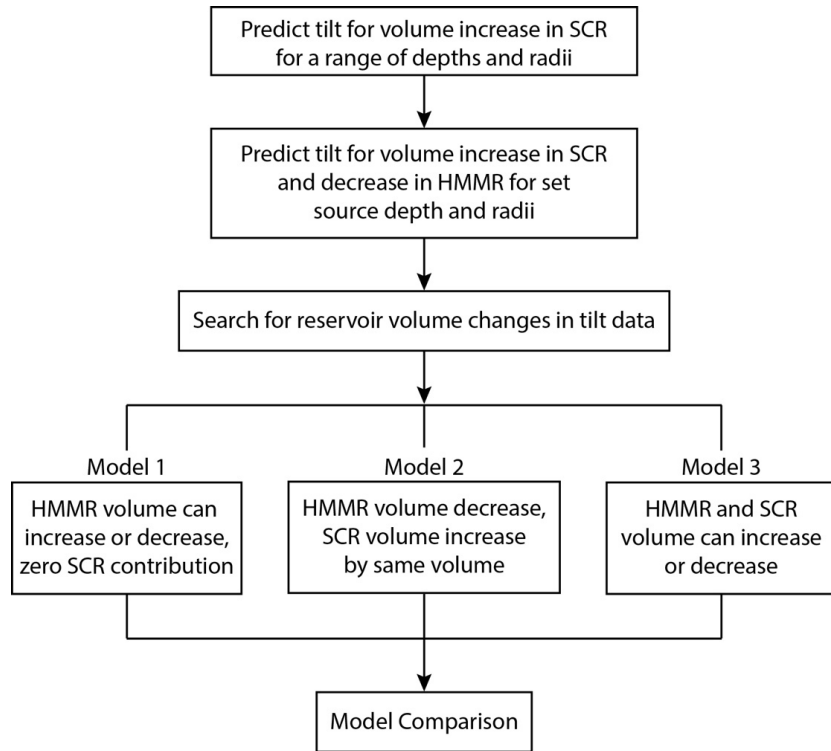


Figure 2.3. Flow chart showing modeling steps followed in this study. HMMR = Halema‘uma‘u reservoir, SCR = south caldera reservoir. All tilt predictions use a spherical geodetic source to represent magma reservoirs.

positioning system (GPS), interferometric synthetic aperture radar (InSAR), and strain-meter data [Cervelli and Miklius, 2003; Dawson et al., 2004; Baker and Amelung, 2012; Poland 2012]. HVO tiltmeters record at a 1-minute sampling rate and telemeter data back to the observatory. We use data from four summit tiltmeter sites surrounding the caldera that record DI events: UWE, SDH, SMC, and IKI. The IKI site records events less clearly than the others, and a rotational offset at the SMC tiltmeter has been suggested [Cervelli and Miklius, 2003; Anderson et al., 2015] because tilt azimuths from this site are slightly discordant with those recorded at the other sites. The HVO maintains a catalogue of ~ 500 hand-picked DI events between the period January 1, 2000 to December 31, 2013 that identify the times of the onset of deflation, onset of inflation, and the end of rapid inflation. We used this catalogue to identify the DI events larger than $4 \mu\text{rad}$ after 2010; the period when the full tilt and GPS observational network was operating. Events larger than $\sim 4 \mu\text{rad}$ have stronger signal to noise ratios, and the potential of being detected in GPS data. Ignoring events with missing data left 16 events for analysis. Outliers in the tilt data were cleaned using a median filter, and a diurnal signal estimation [Weron, 2010] was applied to reduce periodic noise for each of the selected time windows. The tilt data were then low-pass filtered and decimated down to a 5-minute sample rate which is sufficient to resolve the temporal details of the DI events. Large magnitude DI events are also recorded by the network of GPS receivers on Kīlauea operated by HVO, Stanford University, and the University of Hawai‘i. Kinematic GPS solutions were produced from 30 s sample data files. These were cleaned, low-pass filtered, and decimated down to 30 minutes for the time windows of the DI events.

2.5. Predicted tilt from modeling geodetic sources

2.5.1 Magma reservoir deformation during DI events

The deformation produced by a volume change in a magma reservoir can be examined using geodetic modeling to determine if any combination of model parameters (source depth, radius, and volume change) for the SCR exists that would result in detectable DI tilt signals. For a spherical magma chamber, the pressure and volume change can be related by $\Delta V = \pi \Delta P r^3 / G$, where ΔV is the change in volume, ΔP is change in pressure, r is radius, and G is the elastic shear modulus [Segall, 2013]. Reorganizing the equation, the pressure can be solved for given a radius

and change in volume. The pressure is used as an input parameter of the model sources and used to predict the tilt.

Previous studies have estimated magma reservoir volume changes necessary to produce a given amount of tilt [Anderson *et al.*, 2015; Dvorak and Dzurisin, 1993]. The volume of blocked magma during DI events was estimated by Anderson *et al.* [2015], by multiplying the magma supply rate (assumed to be constant) by the length of time of the blockage (the deflationary phase of the DI event). For a DI event lasting 3 days and a magma supply rate of 6 m³/s [Poland *et al.*, 2012], the volume of blocked magma was found to be up to 1.5 Mm³, which could produce up to ~2 cm of uplift and ~5 μrad of tilt for a SCR at 4 km depth. Dvorak and Dzurisin [1993], determined a conversion factor between tilt and volume to be 0.00045 km³ = 1 μrad of tilt at the UWE tiltmeter. The average deflation magnitude of DI events in our study is 4.8 μrad, which results in a volume of 2.2 Mm³ using the conversion factor that we take as an upper limit.

We modeled a spherical geodetic source [McTigue, 1987] for depths 500–5000 m and radii 400–4000 m set at the approximate horizontal location of the SCR determined by Poland *et al.* [2012]. The tilts were predicted at each of the four summit tiltmeters for a 1.5 Mm³ volume increase in the SCR (Fig. 2.4). For a source at the previously estimated depth range of 2.5–4 km, the largest predicted tilts are between ~7 and 20 μrad to the west at site SDH. The north component at site SDH predicts only 0.2–0.6 μrad of tilt since the location of the tiltmeter is directly west of the source location. Tilts predicted at site SMC are between 6 and 20 μrad to the north and 4 and 14 μrad to the east. At site UWE, predicted tilt magnitudes are between 2.5 and 5 μrad to the north and 1.6 and 3.2 μrad to the west, with similar magnitudes at site IKI. The average sensitivity of tiltmeters at HVO is ~0.1 μrad [Dzurisin *et al.*, 2007], and the deflation magnitudes of ~500 DI events cataloged by HVO are between 0.4 μrad and 8.5 μrad, implying that DI related perturbations as small as 0.4 μrad can be detected, and that realistic changes in tilt magnitudes are not likely greater than ~8.5 μrad. Comparing these values with our results suggests that volume changes of the predicted magnitude range in the SCR alone would produce detectable deformation at all four tiltmeter sites, and particularly at sites SDH and SMC.

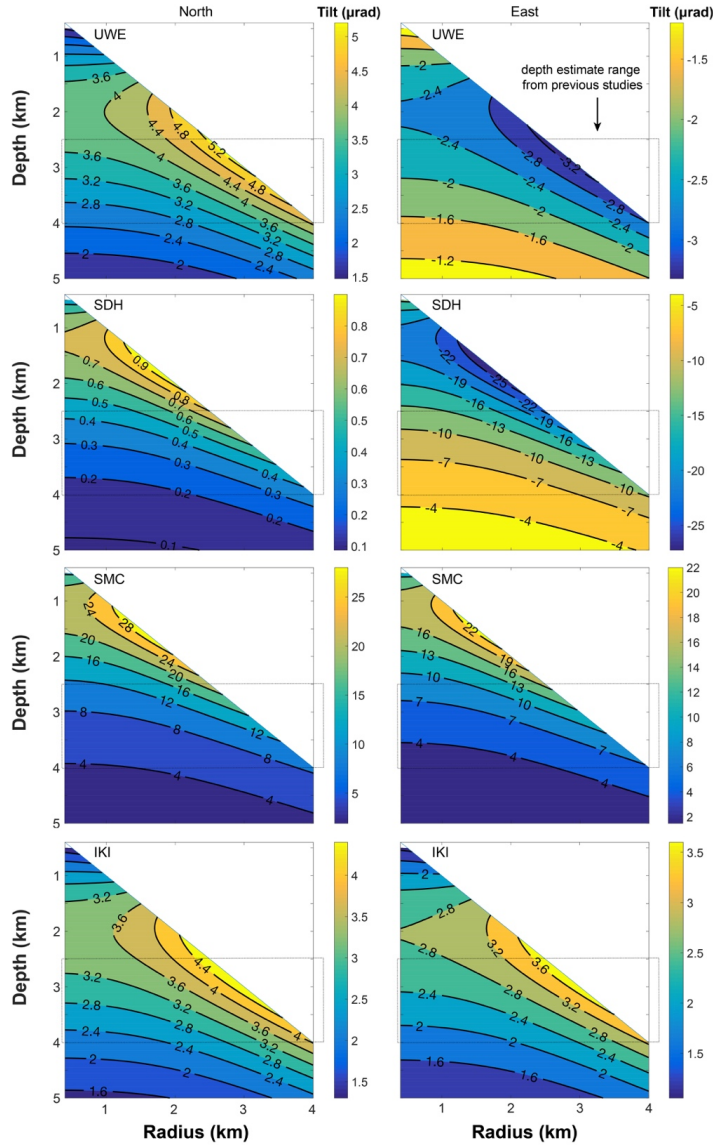


Figure 2.4. Predicted north and east components of tilt (black contour lines) at the locations of the four summit tiltmeters for a 1.5 Mm^3 volume increase in a spherical geodetic source located at the SCR horizontal location with depths 0.5–5 km and radii 0.4–4 km. All tilt values given in μrad . Tilt increases from dark blue to bright yellow. Only physically plausible reservoir depth and radius combinations are shown (source radius cannot be greater than depth). Dashed box outlines approximate depth range estimates of SCR from previous studies.

2.5.2 Deformation for volume increase in SCR and decrease in HMMR

The overall pattern of deformation during DI events implied by the scenario in Figure 2.2A is produced by a volume decrease in the HMMR and simultaneous volume increase in the SCR. Both summit magma reservoirs were modeled to predict the deformation for a volume decrease in the HMMR and simultaneous volume increase in the SCR to test if SCR related deformation is detectable over HMMR deformation. The model configuration consists of two spherical sources [McTigue, 1987], with the HMMR at 700 m radius and 1000 m depth, and SCR at 800 m radius and 3000 m depth. These parameters were selected based on plausible values (non-intersecting reservoirs and reservoir size not exceeding depth) from previous geodetic studies [Poland, 2012; Anderson *et al.*, 2015; Baker and Amelung, 2012, Cervelli and Miklius, 2003]. Volume changes of 0.35 Mm^3 are used, as this volume produces tilts most similar in magnitude to the observations in this study. Each source deformation was predicted separately while requiring that the equivalent volume of magma removed from the HMMR is added to the SCR. The overall predicted deformation pattern was obtained by adding the deformation produced by both sources [Lisowski, 2006].

The effect of the SCR pressure increase on the overall deformation is evident in the mapped predictions, with SCR related tilt causing a rotation of the overall tilt vectors away from the HMMR tilt vector directions (Fig. 2.5). The combined pattern of deformation shows ~ 30 degrees of rotation at tiltmeter sites SDH and SMC away from the SCR source location, such that the predicted vectors no longer point to a single source at the HMMR, as is observed for DI events [Cervelli and Miklius, 2003; Anderson *et al.*, 2015]. The influence of the SCR on the overall deformation pattern is most extreme in the east-west component of the SDH tiltmeter, which is located almost directly west of the approximate SCR location. Here, the predicted tilt from the HMMR is $2.8 \mu\text{rad}$ to the east, and the predicted tilt from the SCR is $2.0 \mu\text{rad}$ to the west, resulting in an overall tilt of $0.9 \mu\text{rad}$ to the east. At UWE the predicted HMMR tilt is $4.5 \mu\text{rad}$ to the south and $4.6 \mu\text{rad}$ to the east, while the SCR contribution is $0.7 \mu\text{rad}$ to the north and $0.47 \mu\text{rad}$ to the west. Combining these gives an overall tilt of $3.8 \mu\text{rad}$ to the south and $4.2 \mu\text{rad}$ to the east. The SCR contribution is greater than the average noise of tiltmeters ($0.1 \mu\text{rad}$) and

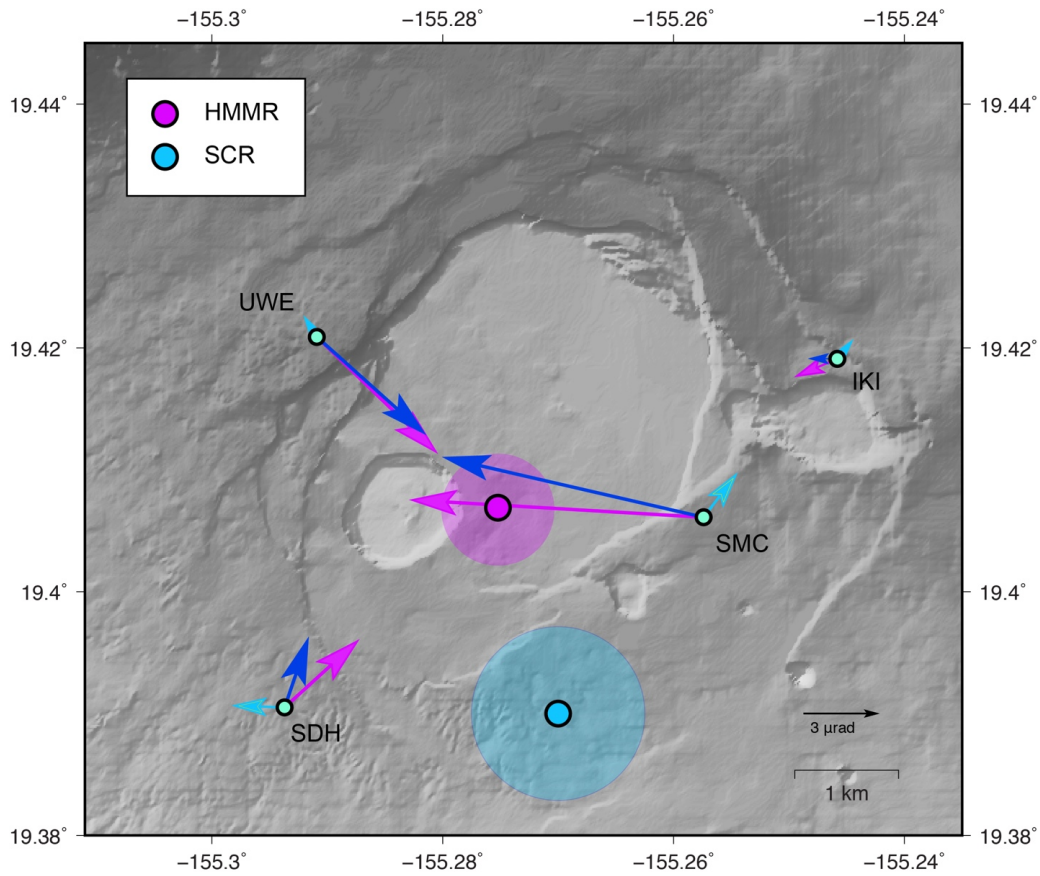


Figure 2.5. Model predictions of tilt at Kīlauea summit for spherical sources representing HMMR decreasing in volume by 0.35 Mm^3 (pink vectors), SCR increasing in volume by the same amount (light blue vectors), and the total resulting tilt produced by adding both deformation signals (dark blue vectors). Shading around source locations indicates approximate reservoir size.

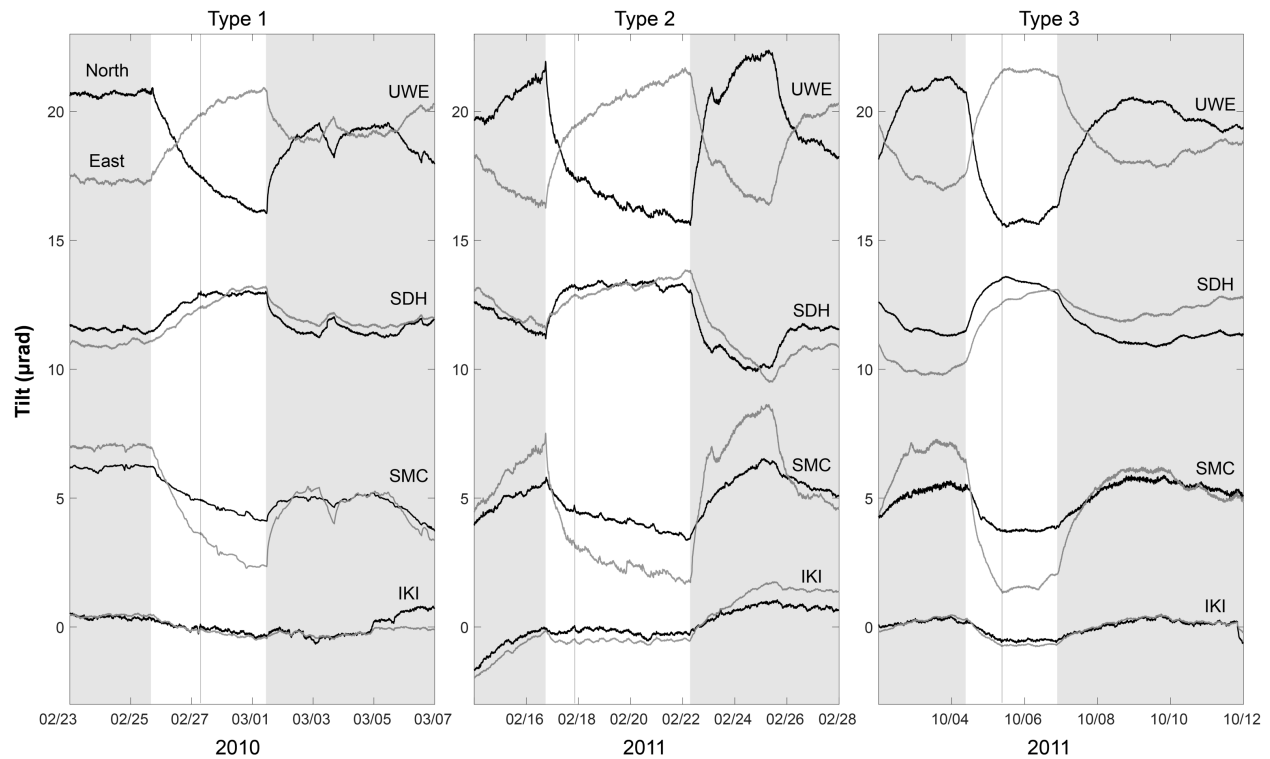


Figure 2.6. North (black) and east (gray) tilt recorded on four tiltmeters (note variation in signals at each instrument). Examples of three DI events described in text showing differing characteristic patterns. Note the change in rate of deflation at various sites, indicated by vertical lines delineating Parts 1 (P1) and Parts 2 (P2) as defined in this study. P1 = onset of initial deflation through end of initial deflation rate, P2 = end of initial deflation rate to onset of rapid inflation.

above the threshold of the smallest DI event magnitude ($0.4 \mu\text{rad}$), and therefore likely has a detectable influence on the overall tilt signal, although the HMMR signal is greater in magnitude.

2.6. Selected DI event observations

2.6.1 Characterizing events

We analyzed the 16 largest ($>4 \mu\text{rad}$ magnitude) DI events between 2010 and 2012 to test if tilt vectors at the summit sites suggested inflation from the SCR region. The selected events were categorized by HVO as U-type events based on their decreasing rate of deflation over 1–3 days, however the temporal evolution of the deflationary phase is variable among events (Fig. 2.6). Four events were characterized by well-defined exponentially decaying signals, and seven events consisted of two distinctly separate deflation phases, each exhibiting nearly linear tilt rates. The remaining events showed tilt beginning to increase slightly during the secondary phase before the onset of rapid inflation, which appears as a parabola-shaped time series.

For all events, the observed deflation signal was divided into two separate phases: an initial rapid deflationary phase (Part 1) followed by a secondary phase smaller in magnitude (Part 2) representing a lower rate of deflation. The onset of rapid inflation marks the end of the entire deflationary phase of the event. We chose to identify two separate phases of the deflationary period because the nature of the signals appears to be distinct and therefore may not be controlled by the same physical processes. Dividing these phases also allowed the tilt vectors for each phase to be viewed separately and provide a more detailed analysis than measuring a single magnitude of deflation over the entire event. The transition between Part 1 and Part 2 was hand-picked from the tilt data. Part 1 (initial deflation) is similar for all events, however, the temporal evolution of Part 2 (secondary phase) is variable. The signal to noise ratio in GPS data is lower than the tilt; however, the distinction between Parts 1 and 2 can still be observed at certain sites, for example, in GPS line-length changes across sites UWEV and CRIM in the north and east components (Fig. 2.7), confirming the transition to slower rates of deformation observed in the tilt data. GPS data in the vertical component were too noisy to detect a clear signal over these short time periods.

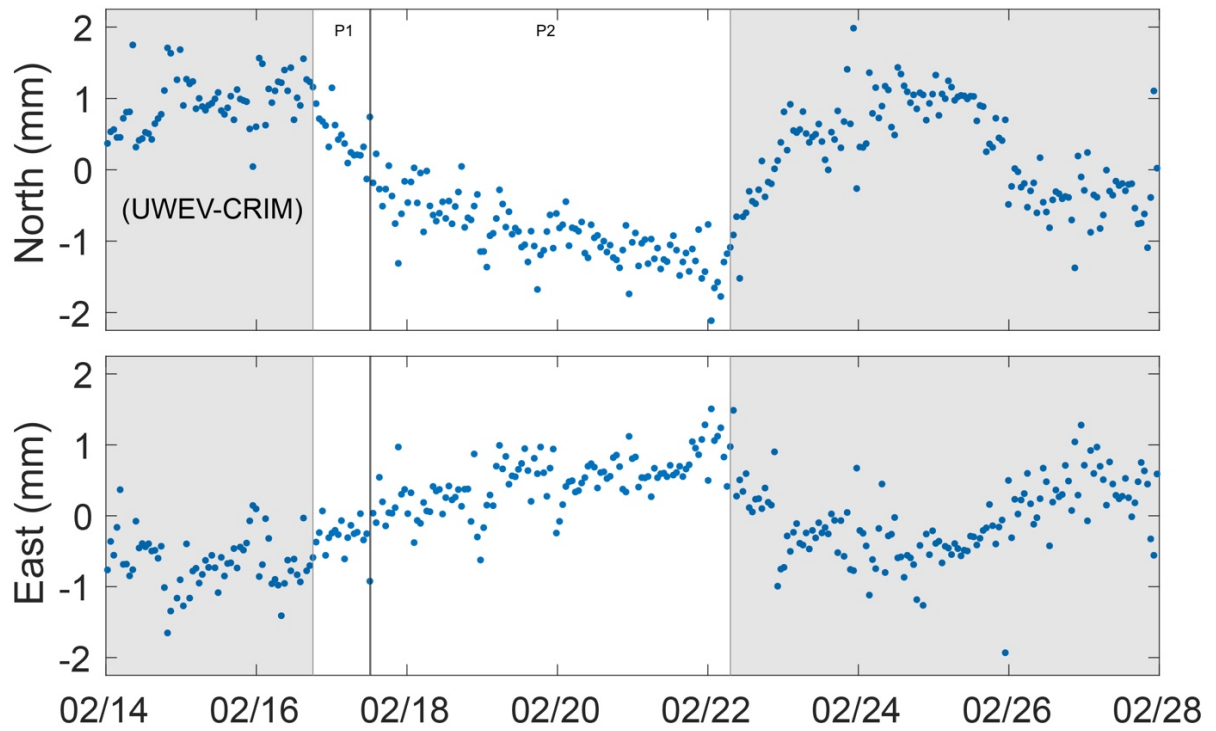


Figure 2.7. DI event recorded in GPS line-length changes across summit sites UWEV - CRIM in March 2011. Vertical line separating Part 1(P1) and Part 2 (P2) was hand-picked from tilt data. Note change in rate of deformation between parts 1 and 2 in the north displacements.

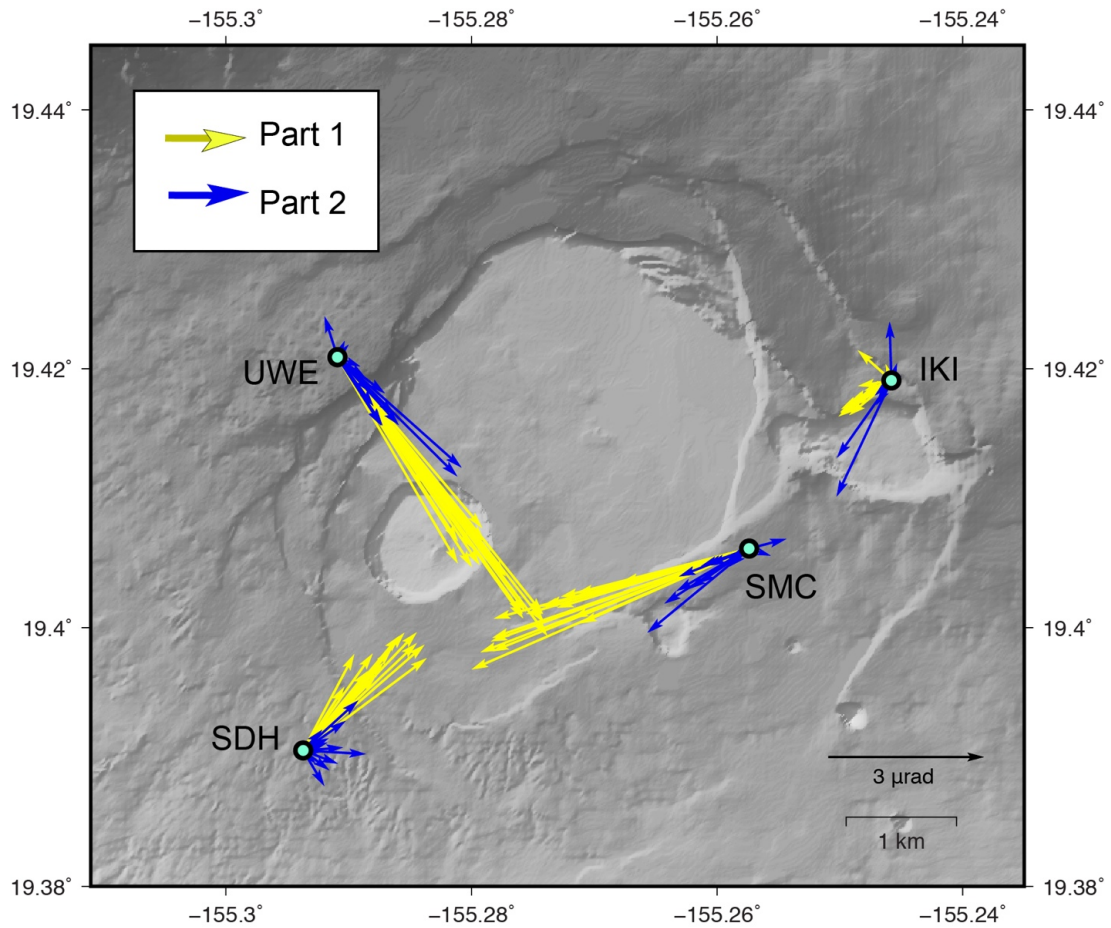


Figure 2.8. Tilt observations for the 16 largest DI events between 2010 and 2012. Each event is divided into two parts: initial phase (Part 1) and secondary phase (Part 2). Note the decrease in magnitude, and difference in azimuthal direction of Part 2 compared to Part 1.

When viewed spatially, tilt vectors for Part 1 point to a region east to southeast of Halema'uma'u crater within the caldera (Fig. 2.8), consistent with previous studies. For Part 2, the magnitudes of tilt-vectors decrease, and azimuths tend to rotate away from the orientation of the initial deflation phase. At UWE, four of the Part 2 vector azimuths are consistent with the Part 1 azimuths, but the remaining vectors rotate slightly in the counterclockwise direction, which is what is predicted for an inflating SCR. Interestingly, the Part 2 vectors at SDH and SMC tend to rotate to the south, pointing towards the SCR, which is a rotation in the opposite direction of the predicted tilts for an inflating SCR. The range of Part 2 vector azimuths is most extreme at SDH, where vectors rotate clockwise up to ~120 degrees from their initial positions. At IKI, although the DI events are less clear, a difference between Part 1 and 2 azimuths can still be observed.

2.6.2 Modeling events and model comparison

We searched for the volume change in the reservoirs that minimized the misfit between the model solutions and the observations in a least-squares sense. The model configuration consisted of two spherical sources as described in Section 2.5.2, with constant source depth, radius, and horizontal location. Only the pressure (volume) in each source was allowed to vary. Three models were tested: Model 1) The HMMR allowed to freely increase or decrease in volume with zero contribution from the SCR, Model 2) The HMMR allowed to freely decrease in volume, and the SCR defined as increasing in volume by the same amount, and Model 3) Both the HMMR and the SCR allowed to independently increase or decrease in volume. The inputs were the observed steps in magnitude from the beginning and end of Part 1 and Part 2 for the north-south and east-west components at all sites, and the associated errors.

Tilts were predicted for each of the modeled pressure solutions and compared with observed data to find the residuals between them. The AICc (Akaike Information Criterion with correction for small sample sizes) was calculated to identify the minimum AICc, indicating the preferred model. Because we are primarily concerned with how our candidate models compare with each other, we construct the delta AICc by subtracting the minimum AICc from all values. For each time period, the lowest delta AICc is Model 3. Model 1 gives the second lowest AICc

for each period, which is consistent with previous studies proposing that DI events manifest in the HMMR without observed contribution from the SCR [Cervelli and Miklius, 2003; Anderson *et al.*, 2015]. Model 2, which forces the SCR to increase by the same volume as the HMMR decrease, consistently gives the highest delta AICc of any model, indicating this model should be rejected as an explanation for the observed signals.

These results support Model 3, a two-reservoir model with unconstrained pressure changes in the SCR, as the most representative model for the data. The AICc test absorbs the statistical impact of additional free parameters in describing the observations, which implies that the SCR pressure changes are not modeling random noise, but are describing a coherent signal that is at least similar to the signal expected from magma pressure changes in the SCR. The predicted pressure changes in the HMMR and SCR for Model 3 have Pearson's correlation coefficients of $r = -0.2029$ for Part 1, $r = -0.2075$ for Part 2, $r = -0.0861$ for Part 1 in the HMMR and Part 2 in the SCR, and $r = -0.5787$ for Part 1 in the SCR and Part 2 in the HMMR (Fig. 2.9). All correlation coefficients except that between the SCR during Part 1 and the HMMR during Part 2, are smaller than the critical value necessary to be considered significantly nonzero at the 0.05 level, and all coefficients are insignificant at the 0.01 level. The lack of correlation between HMMR and SCR for the matching time periods (HMMR Part1 vs SCR Part1, and HMMR Part 2 vs SCR Part 2) suggests that the relationship between the reservoirs is more complex than the simple conduit connection implied by Cervelli and Miklius. Otherwise, a nonzero correlation would be expected: a positive correlation given an open conduit, and a negative one given a blockage between them. The lack of correlation between HMMR during Part 1 and SCR during Part 2 also rules out the case where the reservoirs have different characteristic response times to changes in flux [Lengliné *et al.*, 2008]. This situation could have been an explanation for the lack of visible signal during Part 1 at SCR as the larger SCR responds more slowly to a net flux change. But in this case we would expect to see the signal from SCR accumulating through the entire period, especially during Part 2, when there is little masking signal from HMMR. The uncorrelated pressure signals during those time periods, indicate that reservoir activities in the HMMR and SCR are unrelated to each other during DI events.

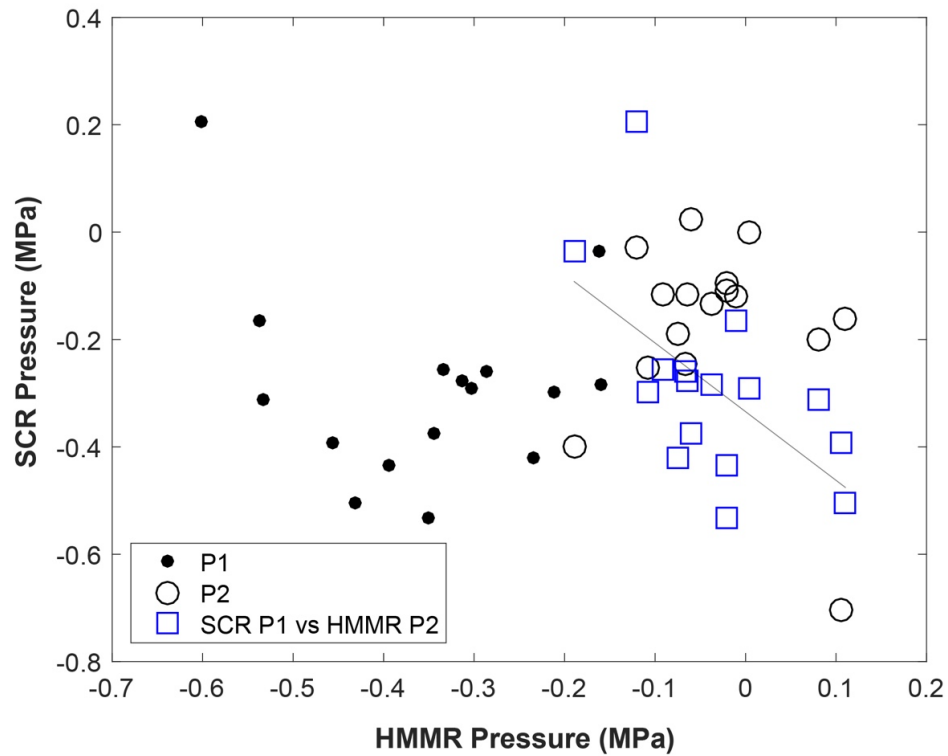


Figure 2.9. Predicted pressure changes in the HMMR versus SCR for Model 3 during Part 1 (P1), Part 2 (P2) and for SCR P1 versus HMMR P2. Pearson’s correlation coefficients are: P1, $r = -0.2029$; P2, $r = -0.2075$; and SCR P1 vs HMMR P2, $r = -0.5787$. Gray trend-line shown indicates the best fit least-squares linear correlation between SCR P1 vs HMMR P2 (slope = -1.2794).

The negative correlation between the SCR during Part 1 and the HMMR during Part 2 implies that for a given pressure (volume) increase or decrease in the SCR during Part 1, the pressure in the HMMR tends to change in the opposite direction during Part 2. The correlation trend-line for SCR vs HMMR pressures has a slope of -1.2794 . This is equivalent to a slope of approximately -2 for SCR to HMMR volume changes. The average change in volume in the SCR during Part 1 is 0.155 Mm^3 , and 0.013 Mm^3 in the HMMR during Part 2, which gives a ratio of 12:1, much larger than would be expected for the observed correlation trend of ~ 2 . The range in predicted relative volume changes makes it difficult to hypothesize a single representative process that characterizes all events. Therefore, it remains plausible that this correlation may be a result of statistical analysis and does not represent a physically realistic scenario.

Table 2.1.

Delta AICc results for three models tested: Model 1) HMMR allowed to freely increase or decrease in volume, zero contribution from SCR; Model 2) HMMR allowed to freely decrease in volume, the SCR set to increase in volume by same amount; Model 3) Both HMMR and SCR allowed to freely increase or decrease in volume.

Period	Model 1	Model 2	Model 3
Part 1	94.78	197.54	0
Part 2	180.3	205.29	117.45
Entire event	233.28	290.19	160.47

2.7. Discussion

Analysis of deformation implied by the configuration of Figure 2.2A during DI events provides insight to Kīlauea’s shallow magmatic system configuration as well as the processes driving magma reservoir activity. *Cervelli and Miklius* [2003] modeled a source east of Halema‘uma‘u crater that fit tilt observations for four DI events, and *Anderson et al.* [2015] analyzed 500+ DI events modeling a source in the same area. Our results favor a model with unconstrained pressure changes in both the HMMR and SCR, although Part 1 of the events are

much more strongly associated with the HMMR than with the SCR. The AICc values also show that all models we tested describe Part 1 of the DI events better than Part 2. The better fit of the models may be because the tilts during Part 1 are larger in magnitude, have higher signal to noise ratio, and are more similar in orientation for all events than the variation exhibited during Part 2. This decrease in magnitude and inconsistency in azimuthal rotation suggests changes within the system that are not sufficiently described by the SCR alone.

The more complex deformation pattern during Part 2 may be a result of activity within other storage zones. Migrations of deformation centers at Kīlauea's summit have previously been documented, and it is suggested that they result from the interconnection of magma storage and transport areas that activate in response to accumulation or withdrawal of magma over time [Fiske and Kinoshita, 1969; Dieterich and Decker, 1975; Schimozura, 1981; Ryan *et al.*, 1981; Yang *et al.*, 1992; Lockwood *et al.*, 1999]. Although recent decades have seen major activity mostly confined to the Keanakāko'i region, and the upper Southwest Rift Zone, it is possible the signals we observe in Part 2 are associated with small-scale pressure variations within some combination of these other zones.

The apparent relocation of the main source of deflation from east of Halema'uma'u crater to south of the caldera observed between Parts 1 and 2 of some of the DI events, could reflect a migration of magma to another part of the system. Wright and Klein [2014] note that for many volcanic events at Kīlauea, such as those causing the varying Fisk and Kinoshita [1969] inflation centers from 1966 to 1967, deflation vectors may rotate clockwise from UWE. They interpret this rotation as initial draining of the northern region of the magmatic system, followed by draining of areas in the south. At SDH and SMC, the tilt vector rotations towards the SCR location could reflect a similar draining of the eastern Halema'uma'u magmatic region during Part 1, followed by subsequent draining in the south during Part 2. The slight counterclockwise rotations generally observed at UWE during Part 2, however, are not consistent with draining of the SCR, and instead would imply inflation of a nearby source to the south. If these rotations at UWE were caused by HMMR inflating slightly, it could be expected that the inflation would be

detected at the other tiltmeter sites [Mogi, 1958; Lisowski, 2006], but this is not clearly observed as evidenced by the majority (13 of 16) of predicted pressures for Model 3 indicating deflation. *Dvorak and Okamura* [1983] suggested that the apparent exponential decay rate of summit tilt signals is controlled by magma flow rates and other similar properties, and that volcano rheology and migration of subsidence centers are not controlling factors. *Anderson et al.* [2015] suggested that U-type DI events could be caused by a different type of blockage or a blockage deeper in the system than between the SCR and HMMR. We agree that this interpretation could be plausible. If the blockage occurs deeper than SCR, HMMR would rapidly deflate when magma leaves the system to the ERZ, assuming it is not supplied by SCR at a faster rate. During rapid HMMR deflation, magma would still be moving from the SCR to HMMR because of the pressure difference between them, but HMMR would not necessarily inflate since magma is being output to the ERZ at a higher rate than the recharge. *Baker and Amelung* [2012] proposed a similar top down model configuration. This model fits tilt observations for the most part, except for the counterclockwise rotation at UWE.

The overall deformation pattern may also be influenced by a misfit that has been suggested for the SMC tiltmeter, which generally points south of the approximate HMMR location [*Anderson et al.*, 2015]. The UWE tiltmeter could be detecting localized signals such as smaller magmatic storage zones, hydrological or hydrothermal system changes, stresses from faulting, or responses to rheological properties around the caldera rim, while the tilt signals at site SDH could be affected by local effects in the south caldera region [*Dvorak and Okamura*, 1983; *Lockwood et al.*, 1999].

It is possible that SCR inflation during Part 1 may still be undetected, but this seems unlikely as the same amount of magma blocked would theoretically produce a large enough signal to be detected. If the best fitting model for Part 1 only includes HMMR deflation, the question remains of where the magma blocked from HMMR is stored if a blockage occurs between SCR and HMMR. Tilt observations over the course of the DI events reflect a more complex deformation pattern than the transfer of volume through a conduit connecting reservoirs implied by Figure 2.2A. With the constraint of only four tiltmeters, a two-source geodetic model

may not be able to accurately predict the complex deformation pattern. DI events are currently ongoing at Kīlauea and further analysis can provide insight to how these events manifest.

The results suggesting a possible correlation between reservoirs over the two parts of the deflation phase imply that for lower pressures in SCR during Part 1, pressures are higher in the HMMR during Part 2. This may imply blockages in the system that have partially breached before completely opening, such that a fraction of the magma is transported into the HMMR during Part 2 before the blockage is fully breached during the rapid inflation. Partial blockages may also help to explain the variation in magnitude and degree of orientation of the tilt vectors for each event.

2.8. Conclusions

Our results are inconsistent with the reservoir configuration proposed by *Cervelli and Miklius* [2003] and shown in Figure 2.2A, suggesting a direct connection from HMMR to the eruption site at Pu‘u ‘Ō‘ō, and a direct connection between the SCR and HMMR which is temporarily blocked during DI events. Inflation of the SCR that would be expected during the HMMR deflation was not detected in our analysis. A blockage occurring below the SCR (Fig. 2.2B, 2.2D) would imply deflation in both the HMMR and SCR during a DI event, but our results do not show a correlation between deflation in the reservoirs over the time periods analyzed.

Our results are also inconsistent with the configuration proposed by *Poland* [2012], which consists of a direct connection between the SCR and HMMR, and the connection to Pu‘u ‘Ō‘ō coming from the SCR. This configuration implies that a blockage between the SCR and HMMR (Fig. 2.2A, 2.2C) should generate little signal from HMMR, unless there is a “sink” for its magma somewhere locally, for which we are unaware of supporting evidence. As with the *Cervelli and Miklius* [2003] configuration, if the blockage is below SCR both reservoirs should experience similar pressure drops, which is not supported by our analysis.

Although our results do not provide us with a preferred candidate for the reservoir configuration and DI process, they do suggest that the HMMR and SCR do not have a simple

connection between them, and that the summit reservoirs are instead perhaps more like the earlier conceptual models of the system consisting of a number reservoirs with their own source conduits connecting in some complex way to the deep magma source.

CHAPTER 3. A FORCE BALANCE PERSPECTIVE OF THE 2018 KĪLAUEA VOLCANO SUMMIT COLLAPSE EVENTS

In preparation for submittal as:

Anderson, A.N., Foster, J.H. and Martel, S.J. (in preparation) A Force Balance Perspective of the 2018 Kīlauea Volcano Summit Collapse Events. To be submitted to Journal of Volcanology and Geothermal Research.

Abstract

Between May and early August 2018, Kīlauea volcano, Hawai‘i, experienced a series of major caldera collapse events that were recorded by a network of geodetic instrumentation. Deformation signals displayed remarkable consistency for the events, which occurred almost daily, and were associated with $M_w > 5$ earthquakes. The caldera collapses are considered to be caused by nearly constant draining of the summit magma reservoir, which increased stresses acting on the caldera ring faults, and culminated in earthquakes and collapses. In this work, we develop a simple force balance configuration relating magma pressure to shear stresses on the caldera ring faults in order to explore the mechanisms preceding collapse. We model the mean of the stacked events recorded in GPS data using a penny-shaped crack to represent a deflating sill-shaped magma reservoir. Adopting a value of 3 GPa for the shear modulus, we find a best-fitting sill depth of 1250 m, radius of 750 m, and total pressure drop of ~ 18 MPa. Stress distributions on the wall of the caldera block are predicted using a two-dimensional pressurized crack model with a $2/\pi$ correction applied to scale to three dimensions. For the deflation period leading up to collapse, we estimate the evolution of magma pressure and average shear stress derived from the force balance and pressurized-crack configurations. Our results reveal that both methods predict similar average shear stresses (~ 5 MPa at the time of failure). Analysis indicates that failure propagates along the fault, suggesting that fault strength is likely the controlling parameter for these collapse events.

3.1. Introduction

Caldera collapses are generally interpreted to be the result of draining magma reservoirs that supply volcanic eruptions or intrusions. They have been documented at basaltic volcanoes across the world (e.g. Kīlauea in 2018, Bárðarbunga in 2014-2015, Piton de la Fournaise in 2007, Miyakejima in 2000, and Fernandina in 1968) [Macdonald *et al.*, 1970; Simkin and Howard, 1970; Geishi *et al.*, 2002; Longpré *et al.*, 2007; Michon *et al.*, 2007; Gudmundsson *et al.*, 2016; Neal *et al.*, 2019]. In these cases, the collapses have evolved similarly. They are characterized by cyclic patterns of deflation culminating in sudden motion during the collapse [Geishi *et al.*, 2002; Michon *et al.*, 2007; Gudmundsson *et al.*, 2016; Neal *et al.*, 2019]. Understanding the pressure changes in magma reservoirs and stresses on caldera faults during caldera collapses can provide insight to the mechanisms driving the events.

The 2018 caldera collapse of Kīlauea volcano was its largest in ~200 years and exceptionally well monitored by a variety of instruments [Neal *et al.*, 2019], making it ideal for studying collapse processes. In this study, we use a force balance approach to investigate the processes driving the Kīlauea summit collapse events by relating magma reservoir pressure to shear stresses on the caldera ring faults. We attempt to understand the relationship between the draining reservoir and fault strength as controlling factors during collapse. To do this, we develop and explore a simplified two-dimensional force balance configuration for the caldera. A crustal deformation model is then used with global positioning system (GPS) data to model the deflating magma reservoir, and analytical equations are used to calculate stresses on the fault walls. The models for magma pressure and fault stresses are related to gain insight into the evolution of the collapse events.

3.2. Background

3.2.1 Kīlauea volcano

Kīlauea is a basaltic shield volcano located on the southeast side of the island of Hawai‘i (Fig. 3.1) and is considered to be one of the most active volcanoes in the world. Magma is supplied from the mantle to the shallow magmatic system below the summit caldera, where it is stored, erupted, or transported along the rift zones [Poland *et al.*, 2014]. Prior to the recent lower

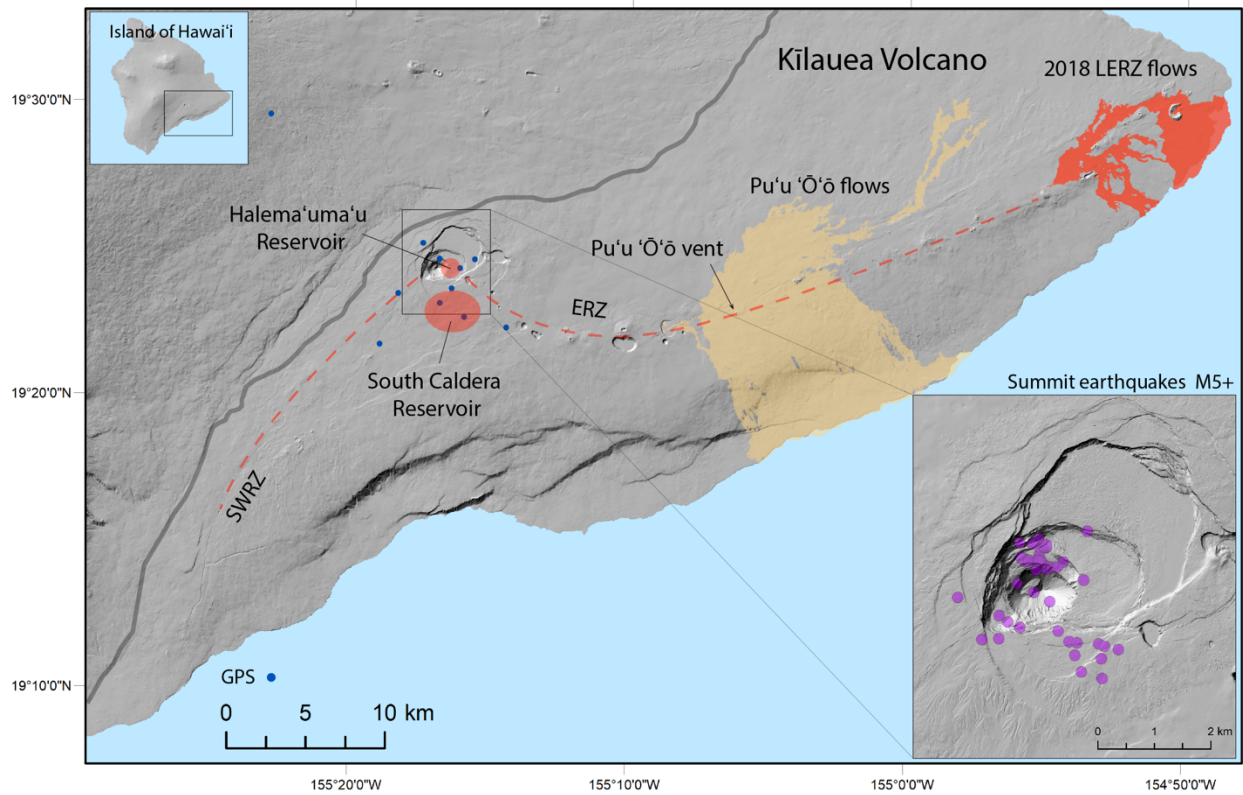


Figure 3.1. Map showing the location of Kīlauea Volcano on the island of Hawai‘i and relevant geologic features. SWRZ: Southwest Rift Zone, ERZ: East Rift Zone, LERZ: Lower East Rift Zone. Inset map on the bottom right is a magnified view of the summit after the 2018 collapse events, with the locations of the $M_w > 5$ earthquake epicenters (purple dots).

East Rift Zone (LERZ) eruption and summit collapse in 2018, a lava lake existed in the Halema‘uma‘u crater within the caldera since 2008, and effusive activity took place predominantly at the Pu‘u ‘Ō‘ō vent along the East Rift Zone (ERZ) since 1983. Surface deformation recorded in geodetic data starting in the 1990s was characterized mainly by subsidence, with inflation occurring from 2003 to 2007 likely due to an increase in magma supply [Poland *et al.*, 2014]. The configuration of the summit magma sources has been investigated in previous studies and is considered to include two main reservoirs, a shallow one east of Halema‘uma‘u crater at ~1 km depth and a deeper, larger one south of the caldera at ~3 km depth [Tilling and Dvorak, 1993; Pietruszka and Garcia, 1999; Cervelli and Miklius, 2003; Poland *et al.*, 2014; Anderson *et al.*, 2015]. Measurements from the GPS network have helped to provide information about the geometry and activity of Kīlauea’s summit magma system.

3.2.2 The 2018 Kīlauea summit collapse

Although Kīlauea is often thought of as a source of gentle effusive-style eruptions, the summit of Kīlauea experienced explosive activity during its caldera building stages in ~1500, during a historic Hawaiian war period in 1790, and after subsidence of an active lava lake in Halema‘uma‘u crater in 1924 [Decker *et al.*, 1984; Swanson *et al.*, 2014]. The 1924 explosions were hypothesized to be caused by mixing of groundwater with hot host rock [Decker *et al.*, 1984]. In early May 2018, Kīlauea summit began to subside as the magma system drained, simultaneously feeding a fissure eruption in the LERZ. The first of several explosive events at the caldera began on May 16, with slope failures widening the vent of the former lava lake. Deflation and explosions at the summit continued intermittently through the end of May, while the walls of Halema‘uma‘u crater slumped inward. Regular summit collapse events within the caldera began on May 29 and continued almost daily until August 2, resulting in a consistent pattern in the GPS data (Fig. 3.2). The events were characterized by Mw 5.2 to Mw 5.4 earthquakes, and appear as rapid (lasting a few seconds), radially outward GPS displacements around the caldera, followed by gradual deflationary (radially inward) GPS displacements and escalating earthquake swarms until the next collapse and Mw > 5 earthquake. Seismicity decreased abruptly following the large earthquakes as the cycle began again. During each of the collapse events the caldera floor dropped several meters, enlarging Halema‘uma‘u crater. The

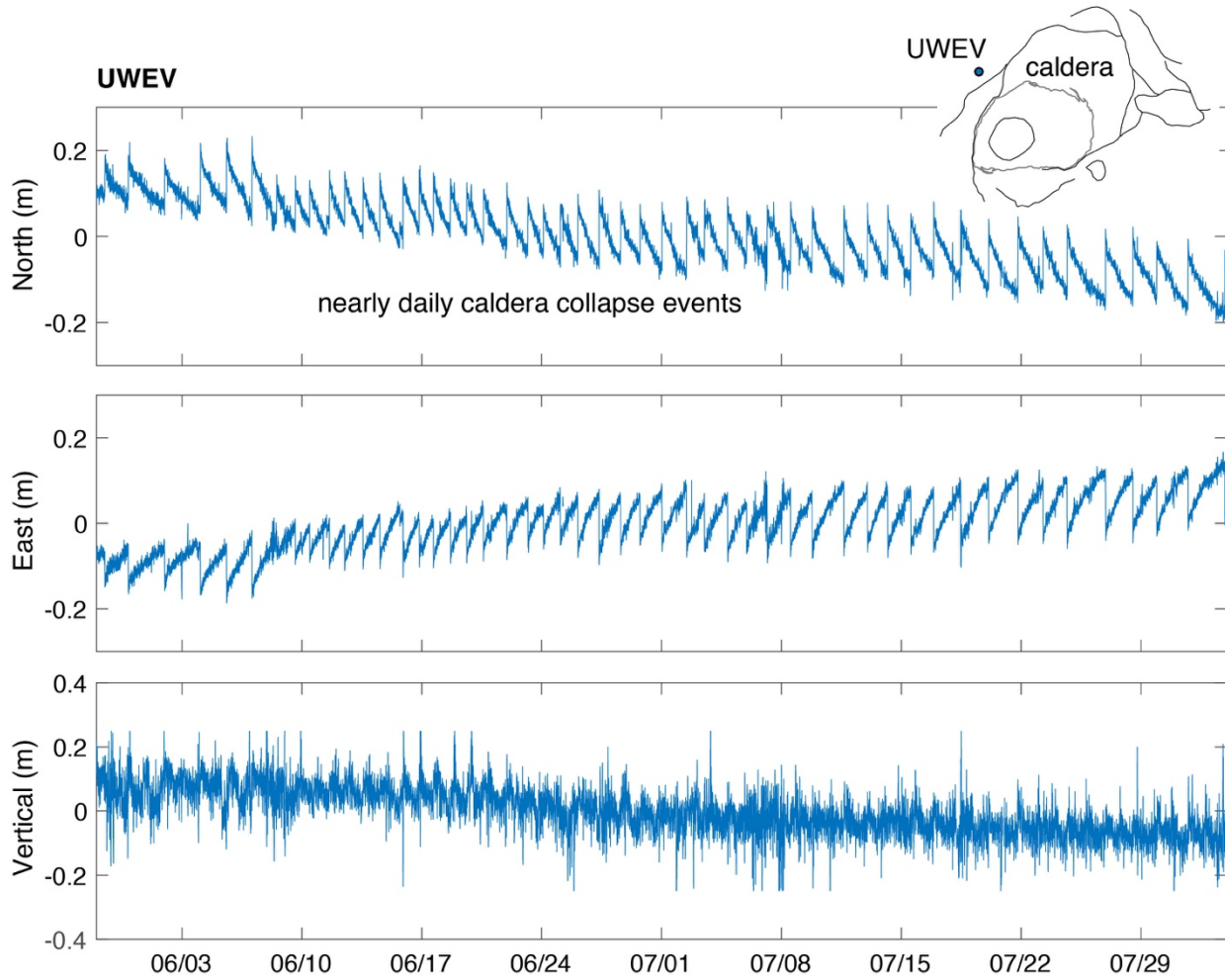


Figure 3.2. Displacement components during the Kīlauea caldera collapse events recorded at the summit the UWEV GPS station between May 29 and August 2, 2018. Map shows location of UWEV station on Kīlauea caldera.

cumulative effect was to deepen the caldera locally by more than 500 m [Neal *et al.*, 2019]. By the end of July 2019, a small water pond had developed at the bottom of the new Halema‘uma‘u crater floor; this pond continues to rise at the time of writing.

3.2.3 Caldera collapse dynamics

The dynamics of caldera collapse events globally, including at Kīlauea in 2018, have been previously explained by a piston analogy, where the collapsing column of caldera rock acts as a piston over a pressurized magma source [e.g., Roche *et al.*, 2000; Kumagai *et al.*, 2001; Gundmundsson *et al.*, 2016]. In this scenario, the rock column (the piston) is initially stable and supported by the magma reservoir, and seismicity in the surrounding edifice is low. As magma drains, the pressure in the reservoir decreases, causing subsidence of the summit, increased stress on the caldera ring faults, and earthquake swarms. The rock column is then supported by some combination of magma reservoir pressure and friction on the surrounding faults, so when pressure drops and the summit deflates, the shear stresses on the faults increases. Finally the rock column collapses due to its own weight when the shear strength of the faults is exceeded. After collapse, the rock column stabilizes, again supported by the reservoir pressure, and the process begins again. This cyclic pattern is observed in both deformation and seismic data, including at Kīlauea [Simkin and Howard, 1970; Geishi *et al.*, 2002; Michon *et al.*, 2007, 2008; Neal *et al.*, 2019]. Figure 3.3 depicts a sketch of the collapse process for the Kīlauea collapse sequences on which this study is based.

3.3. Data

3.3.1. GPS network

Kīlauea volcano is well monitored by seismic and deformation networks maintained and operated by the Hawaiian Volcano Observatory (HVO), in collaboration with the University of Hawai‘i, and Stanford University. At the time of the 2018 eruption, sites from the continuous GPS network were logging 1 Hz data and these were processed to obtain 1 position per second data for the period of summit collapse events from May 29 to August 2. The 1 Hz data provide a high temporal resolution that allows us to examine the collapse events at fine time scales.

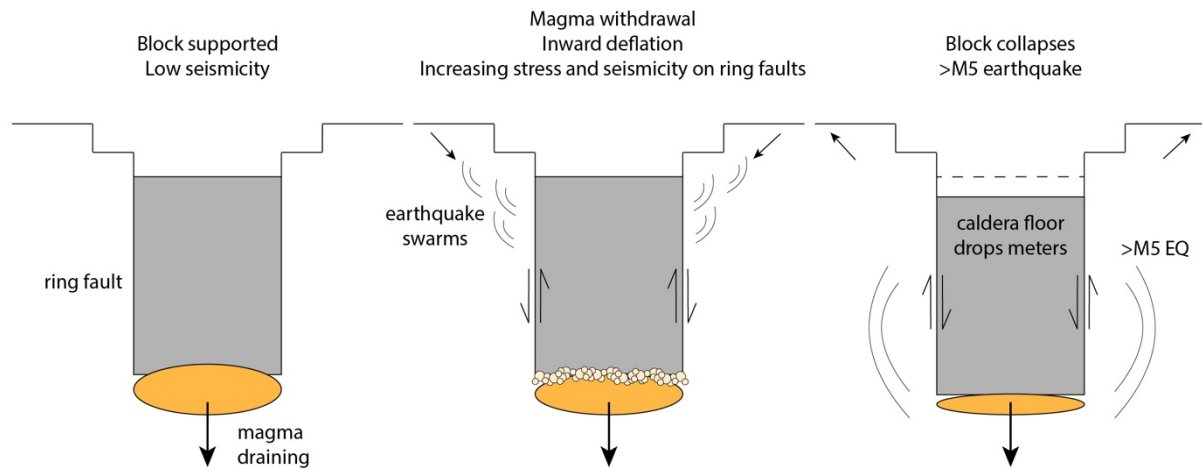


Figure 3.3. Schematic diagram for stages of Kīlauea caldera collapse events modified from USGS HVO published graphic. The block is initially supported by the magma sill and there is low seismicity, but magma is draining. As magma withdrawal continues, inward deflation occurs, with increasing stress and seismicity. Finally, the block collapses resulting in Mw > 5 earthquake and dropping of the caldera floor by several meters.

We used the TRACK kinematic processing module [Herring, 2009] within the GAMIT/GLOBK (<http://geoweb.mit.edu/gg/>) GPS processing software package. The closest GPS site on Maunakea, RADF, was adopted as the reference site, as it was largely unaffected by the collapse events. Data from the GPS sites were processed in baseline mode using the ionospheric independent linear combination. The rate of change of atmospheric delay was constrained to the equivalent of 18 mm in 1 hour.

Additional sites away from the Kīlauea summit were processed to constrain the signals from the summit sites by minimizing effects of noisy data. During the events beginning on May 29, the GPS site NPIT located on the rim of Halema‘uma‘u crater within the caldera sank tens of meters as the floor of the caldera began to subside, and eventually stopped recording completely around June 17. The CALS GPS station east of the former Halema‘uma‘u crater began recording a few days prior to this. Seismic data is taken from the HVO earthquake catalog. We selected a dataset comprised of all $M_w > 5$ earthquakes located within a ~ 2 km radius of the center of Halema‘uma‘u crater as the reference events for the timing of each collapse (Fig 3.1).

3.3.2. Defining a representative GPS event

Between May 29 and August 2, the GPS deformation signals displayed remarkable consistency for the summit collapse events (Fig. 3.2). Because of the uniformity of this pattern, we defined a single representative event for each GPS site by stacking all the events over the time period and taking the mean (Fig 3.4). We used the times of the large ($M_w > 5$) summit earthquakes to isolate individual events and define the start of the cycle, and then scaled the duration of each event so that they all had the same normalized time. The median value for the deflation duration of all the events was 32 hours. Rapid horizontally outward displacements recorded at sites surrounding the caldera accompany the time of the earthquake and reflect the sudden motion when the collapse occurs. These displacements are not included in the representative deflation event, and are not modeled in this study.

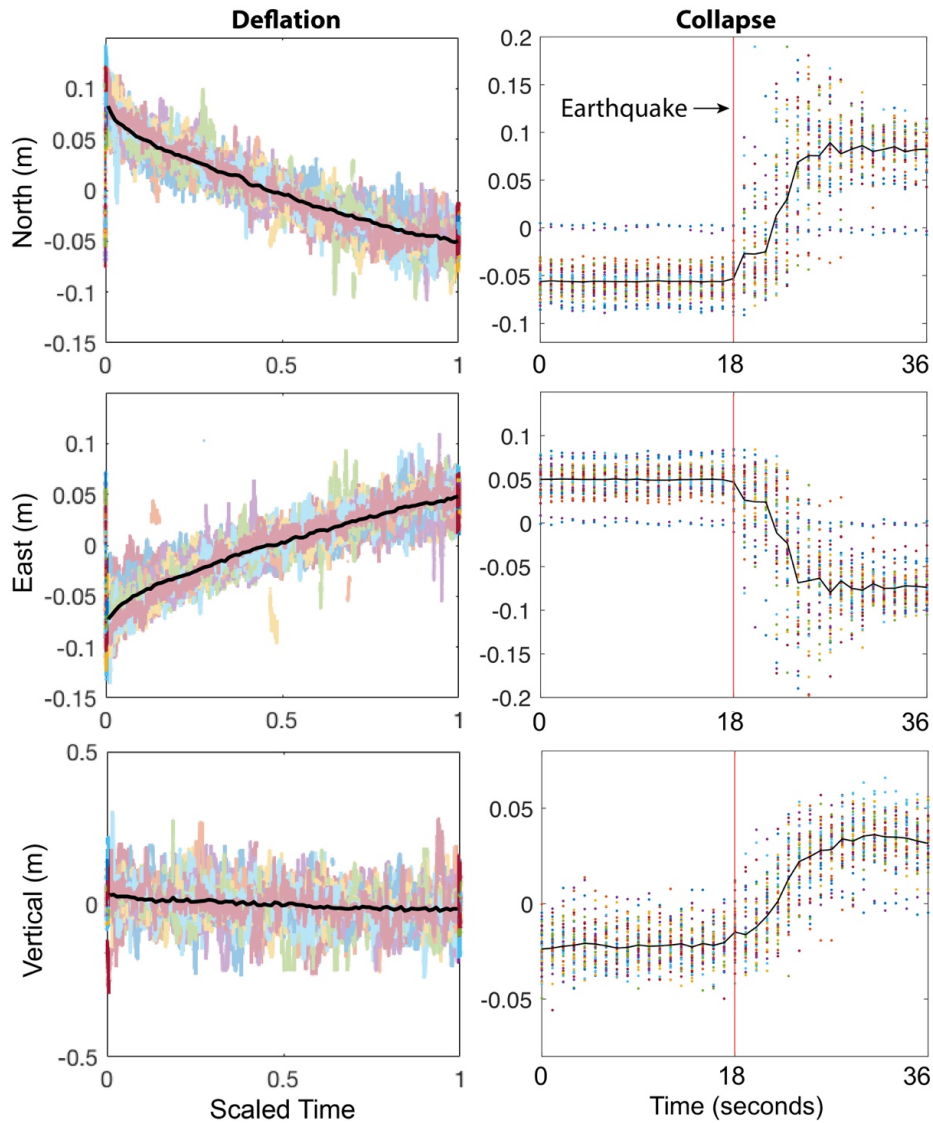


Figure 3.4. Mean signal (black line) of displacement components from stacks of gradual deflations (left column) and outward motions during collapse (right column) recorded at UWEV summit GPS station for the collapse events (49 deflation periods and 50 $M_w > 5$ earthquakes) between May 29 and August 2, 2018. Individual events are shown in different colors in the background. Deflation time series are scaled by setting the onset time of the $M_w > 5$ earthquake to zero and the end time at the next consecutive earthquake to one. Red line indicates time of the $M_w > 5$ earthquake.

3.4. Model

The deflation and episodic collapse events at the caldera were likely related to nearly continuous draining of magma from the summit magma reservoirs to the LERZ [Neal *et al.*, 2019]. The model for the collapse event cycle considers that the column of rock (block) above the magma reservoir at the start of a cycle is completely supported by the magma reservoir below (Fig. 3.3). As magma drains, the ring faults bounding the caldera gradually support more of the weight of the block, increasing the vertical shear stress on the fault and eventually triggering earthquake swarms on these and other nearby faults. Finally, the block collapses due to its own weight resulting in a $M_w > 5$ earthquake.

The goal of our model analysis is to relate the underpressure of the magma reservoir to the average stresses on the caldera ring faults during the deflation period of the collapse events. This involves three steps. 1) A simplified force balance model that describes the key forces acting on the column of rock within the caldera, comprised of gravitational forces, frictional forces due to shear stresses on the caldera ring faults, and the force resulting from the magma source pressure acting over the base of the block. 2) A deformation model for a volcanic sill that gives the source pressure change during deflation [Fialko *et al.*, 2001]. 3) A model for the stress distribution on the faults due to the magma source, based on the analytical solutions for the stresses produced by a two-dimensional pressurized crack in an elastic solid [Sneddon, 1946]. In section 3.4.1 we describe the model setup and develop our initial equations. Next, we find the critical magma pressure when collapse occurs using a deformation model of GPS data in section 3.4.2. We use this best-fitting magma pressure to calculate the two-dimensional stress distribution around the caldera at the time of collapse (section 3.4.3).

3.4.1. Force balance configuration

Our force-balance model represents the rock column of the collapsing caldera interior as a cylindrical block of radius r and height h sitting snugly in a cylindrical space directly above a penny-shaped shaped magma reservoir with the same radius (Fig. 3.5). The block has cross sectional area πr^2 , and density ρ . The average downward force F_{litho} at any given point within the block along its depth is equal to the lithostatic stress acting perpendicular to the horizontal

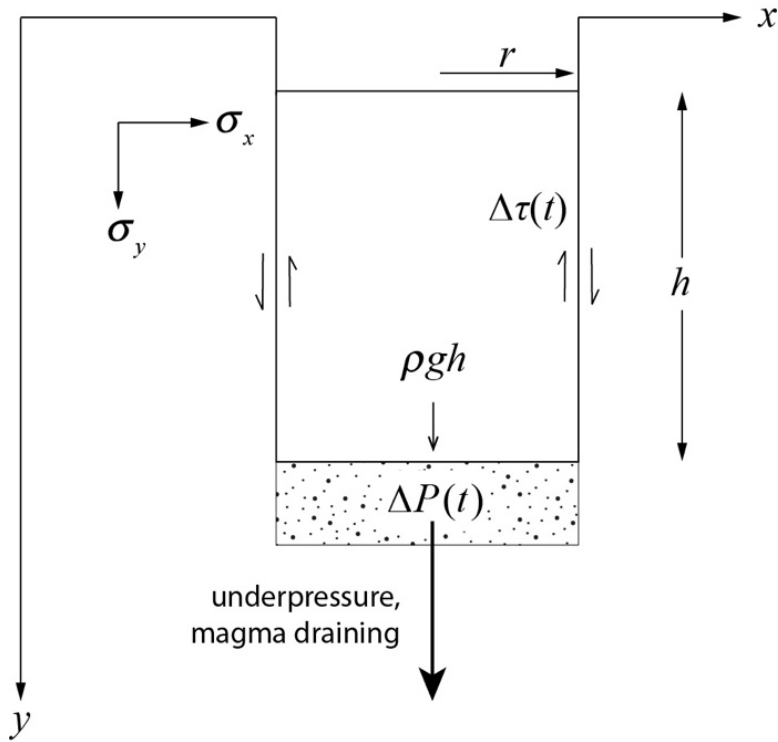


Figure 3.5. Schematic diagram showing the geometry of the model for the caldera block during deflation of the collapse events. A cylindrical column of rock of radius r and height h at lithostatic stress ρgh (at depth h) is supported by a sill-shaped magma reservoir at depth h . The magma pressure is $\Delta P(t)$, and shear stress on the ring faults is $\Delta \tau(t)$; both vary with time.

surface of the block, times its cross sectional area. This force is the weight of the block, given by:

$$F_{litho} = \rho gh(\pi r^2) \quad (3.1)$$

where g is the acceleration due to gravity and h is depth equal to the cylinder height. Since the forces on the column of rock must be equal if the column is in equilibrium, the stress at the base of the block due to its weight is also equal to ρgh . The weight of the block is balanced by a time-dependent upward force from the magma below F_m , which is determined by the pressure of the magma reservoir that acts on the base of the block. The magma reservoir pressure $P_m(t)$ at the base of the block decreases as magma drains from the system. This pressure is the sum of the lithostatic pressure P_{litho} at the source depth h (where $P_{litho} = \rho gh$) and an underpressure $\Delta P(t)$:

$$P_m(t) = P_{litho} + \Delta P(t) \quad (3.2)$$

We consider that P_{litho} is the initial magma pressure at the beginning of the deflation period, i.e. $\Delta P(t=0) = 0$. Multiplying the magma reservoir pressure by the basal area of the cylindrical block gives the upward force exerted by the magma F_m on the block:

$$F_m(t) = [P_{litho} + \Delta P(t)] \pi r^2 \quad (3.3)$$

The magma force F_m can be split into two separate contributions: the upward force from the lithostatic pressure, $P_{litho}\pi r^2$ and the downward force from the pressure drop, $F_{\Delta P}(t) = \Delta P(t)\pi r^2$, such that $F_m(t) = P_{litho}\pi r^2 + F_{\Delta P}(t)$. This notation is useful when summing the net force on the block. As magma drains from the reservoir, the shear stress $\Delta \tau$ on the sides of the caldera walls increase as the wall supports more of the weight of the block. The frictional force F_f on the wall is the product of the lateral surface area of the wall of the cylinder $2\pi r h$ and the average shear stress $\Delta \tau$,

$$F_f(t) = [\Delta \tau(t)] 2\pi r h \quad (3.4)$$

The net force acting on the cylindrical rock column is given by a force balance equation. The forces are $F_{\Delta P}$, F_{litho} , F_f , and $P_{litho}\pi r^2$. Letting $F_{litho} = P_{litho}\pi r^2$, the net force is

$$\begin{aligned} F_{net}(t) &= F_f(t) + F_{litho} - F_{\Delta P}(t) - F_{litho} \\ &= F_f(t) - F_{\Delta P}(t) \end{aligned} \quad (3.5)$$

Equation (3.5) shows that the net force on the caldera block is controlled by a combination of the frictional forces on the walls and the deflating reservoir. Assuming that the block remains stationary as magma drains, equation (3.5) can be set equal to zero, and the average shear stress on the walls of the cylinder (equation 3.4) can be solved for in terms of magma pressure, and the cylinder radius and height. From equations (3.3), (3.4), and (3.5), the average shear stress is shown to be related to magma reservoir underpressure by,

$$\Delta \tau(t) = \Delta P(t) r/2h \quad (3.6)$$

This expression for the evolution of shear stresses on the caldera walls holds as long as $F_{net}=0$, that is, until the time of the collapse event when motion occurs. Knowing the critical magma pressure drop at the time of collapse, the average shear stress on the cylinder wall can be calculated.

Our model assumes that the caldera rock column is a cylindrical block of uniform height and radius slipping along a uniform ring fault, although in reality the structure is much more complex with many faults of varying dimensions and locations. The analysis assumes that the reservoir depth (block height) h remains constant, even though the block is dropping. Therefore decreasing pressure is only a function of the changing underpressure. We do not account for magma compressibility, as it likely only has a small impact on the cycle we are studying

[Anderson *et al.*, 2015], though it may be much more important for the dynamic transient processes during the collapse.

3.4.2. Magma pressure

Displacements from a total of eight GPS stations were used (seven located around the caldera vicinity and one on Maunaloa) (Fig. 3.6) to constrain the modeling used to predict magma reservoir pressure changes during the collapse event deflation period. Displacements within the collapsing caldera at stations NPIT and CALS were so large (meters) for each event, that they were regarded as recording non-elastic responses. As a result, data from those two stations were not included in the model of magma underpressure.

We use a model of a horizontal penny-shaped crack [Fialko *et al.*, 2001] to represent a sill-shaped magma reservoir over the time period of the representative (mean) event. Our approach is to first model the total displacement over the entire deflation period, allowing all the sill parameters (horizontal location, depth, radius, and pressure change) to vary. The best-fit parameters that minimize the misfit between the model predictions and observations were found using a non-linear optimization algorithm that employs the Nelder-Mead method (Matlab© `fminsearch` function). Sill depth was constrained to be between 500 m and 2000 m, radius between 200 m and 2000 m, and pressure change between -100 MPa and 100 MPa. We assumed a constant Poisson's ratio of 0.25 and shear modulus of 3 GPa [Johnson, 1992; Anderson *et al.*, 2015]. The modeling inputs were the observed displacements between the onset and ending of deflation data for the mean of the stacked events at each of the GPS stations (Fig. 3.6).

Once the best fitting sill parameters were identified, we reran the model at finer time scales setting the best-fitting sill location, depth, and radius constant, only allowing the pressure to vary. The deflation time series was divided into 11 evenly spaced intervals. The number of intervals was selected such that displacement from the beginning to end of each interval provides the largest possible reliable signal with the shortest time span. We ran the model to find the pressure changes for each of the time increments, and then summed the results to produce a pressure time series over the entire deflation period (Fig. 3.7). The total pressure at the end of the

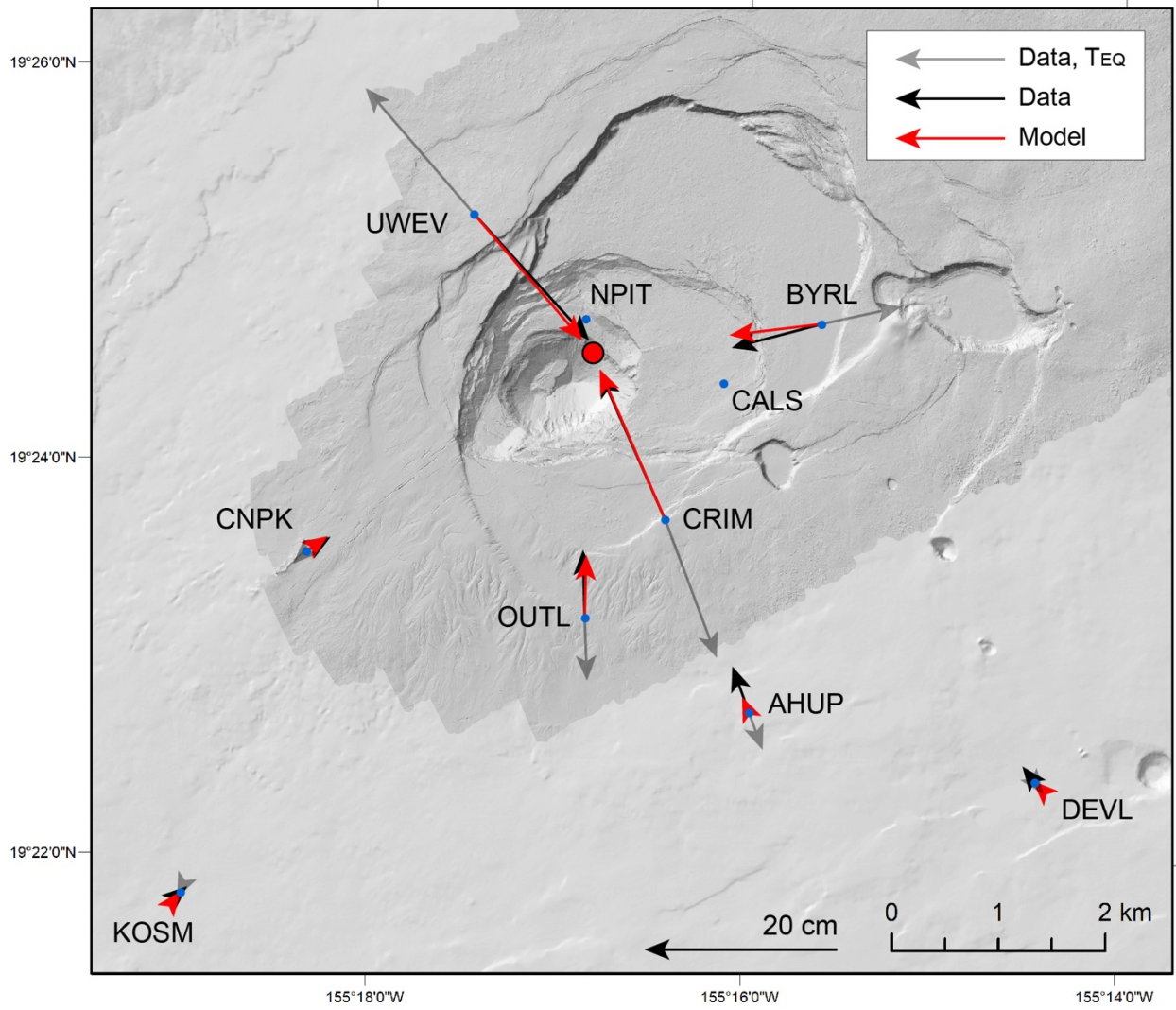


Figure 3.6. Mean deflations (black vectors) and outward motion (gray vectors) of the stacked GPS data and the best-fitting model (red vectors) for the nearly daily summit collapse events. Outward motion is the sudden displacement at the time of the earthquake (T_{EQ}) when collapse occurs. Time series of the deflation data and model predictions are shown in Figure 3.7. The horizontal location of the center of the best-fitting model is shown at a red dot. GPS sites are blue dots.

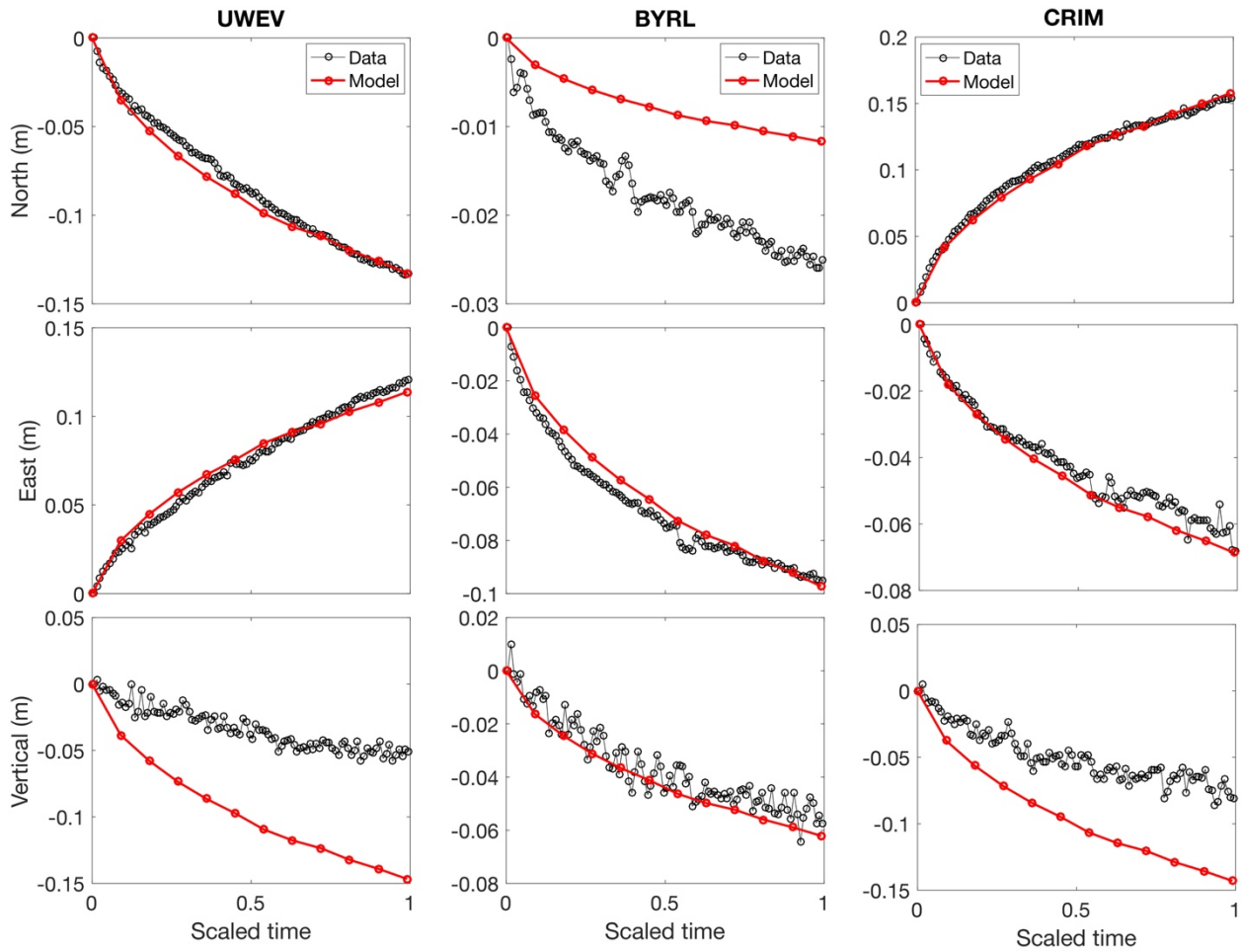


Figure 3.7. Time series of mean displacement components of the stacked GPS data (black) and the model predictions (red) for the best-fitting pressure changes during summit collapse events. GPS stations UWEV, BYRL, and CRIM surround the caldera; site locations are shown in Figure 3.6.

event represents the critical magma pressure at which collapse occurs, and is used to predict the stress distribution at that time.

3.4.3. Stress distribution

We calculated the stresses along the caldera walls by representing the deflating magma sill as a two-dimensional pressurized crack following *Sneddon* [1946]. He derived analytical solutions for the stress distribution in the interior of an infinite elastic solid due to the opening of a finite crack [*Griffith*, 1920] by an applied uniform pressure for a given time. In our analysis the crack is treated as the modeled magma sill from section 3.4.2, with radius r and magma underpressure ΔP at a given time. The normal stresses in the x and y directions (σ_x , σ_y), and the shear stresses (τ) were calculated on a grid representing a two-dimensional, vertical plane passing through the center of the sill, giving a cross sectional view of the stress distribution (Fig. 3.8). The x direction is the distance along the crack, and the y direction is the depth. The equations of the stress components for a two-dimensional crack of half-length $2r$ are:

$$\sigma_x + \sigma_y = 2\Delta P \left\{ \frac{R}{R_1^{1/2} R_2^{1/2}} \cos \left(\theta - \frac{\theta_1}{2} - \frac{\theta_2}{2} \right) - 1 \right\} \quad (3.7)$$

$$\sigma_y - \sigma_x = 2\Delta P \frac{R \sin \theta}{r} \left(\frac{r^2}{R_1 R_2} \right)^{3/2} \sin \frac{3}{2} (\theta_1 + \theta_2) \quad (3.8)$$

$$\tau = \Delta P \frac{R \sin \theta}{r} \left(\frac{r^2}{R_1 R_2} \right)^{3/2} \cos \frac{3}{2} (\theta_1 + \theta_2) \quad (3.9)$$

where R and θ are polar coordinates measured from the origin at the center of the crack (x, y), and (R_1, θ_1) and (R_2, θ_2) are secondary coordinates from each end of the crack, ($x=-r, y$) and ($x=+r, y$), respectively. These expressions are functions of depth (y) and along-crack distance (x), and determine the components of stress at any point in the medium. The sign convention is

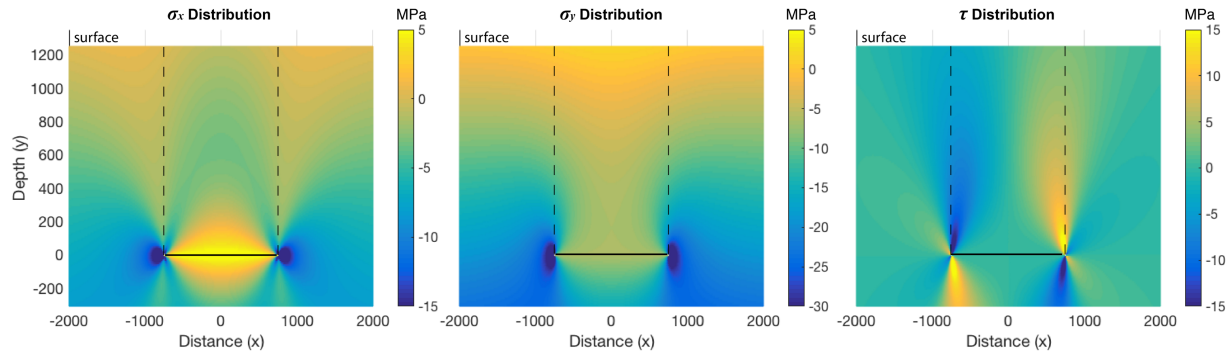


Figure 3.8. Modeled components of the total stress field (ambient field + stress perturbations associated with the crack). Stress perturbations of normal stresses σ_x , σ_y , and shear stress τ due to a pressurized crack (black horizontal line) with half-length = 750 m and depth = 1250 m, for a pressure change in the crack of ~ 18 MPa. The ambient stress field consists of lithostatic stresses that were added to the normal stresses only. Dashed vertical lines represent vertical faults of interest; stress profiles along these lines are shown in Figure 3.9.

consistent for all the stresses; negative values indicate compression and positive values indicate tension. The vertical profile along the crack tip represents the vertical fault that bounds the cylindrical block (Fig. 3.8). We assume that the stresses along this profile are the stresses acting on the fault (Fig. 3.9).

We acknowledge that using a two-dimensional crack model may be more limiting than a three-dimensional penny-shaped crack model, but this provides a first-order approach consistent with initial simplifications of our force balance analysis. Nevertheless, we apply a correction to the two-dimensional model to transform results into three dimensions by multiplying by a factor of $2/\pi$. [Sneddon, 1946]. We use this two-dimensional model to approximate the stresses produced by a deflating penny-shaped magma reservoir. The inputs are the best-fitting sill radius (as the crack half-length), and the resulting pressure changes predicted by the deformation model of the GPS data.

3.5. Results

From our pressure change deformation model (penny-shaped crack), the best-fitting model for the deflation period of a Kīlauea collapse event is a sill with a depth of ~ 1250 m below the surface, with a radius of ~ 750 m, and a pressure decrease of -18 MPa. The best-fitting horizontal location of this source is at the northeastern rim of the former Halema'uma'u crater near to where the lava lake had previously been observed (Fig. 3.6). Model-predicted displacements were obtained by re-running the penny-shaped crack model using the best-fitting pressures and parameters as inputs [Fialko *et al.*, 2001]. The model is able to fit the data for most of the sites in space (Fig. 3.6) and time (Fig. 3.7). Figure 3.7 shows predicted time series for GPS sites UWEV, BYRL, and CRIM, which surround the caldera. The north and east components at UWEV and CRIM fit very well with the mean observations, although the vertical is overpredicted by the model. At site BYRL, the east and vertical components fit best with the data and the model underpredicts displacement to the north. For sites located close to the source, movement on shallow faults may contribute to misfits between the model and data.

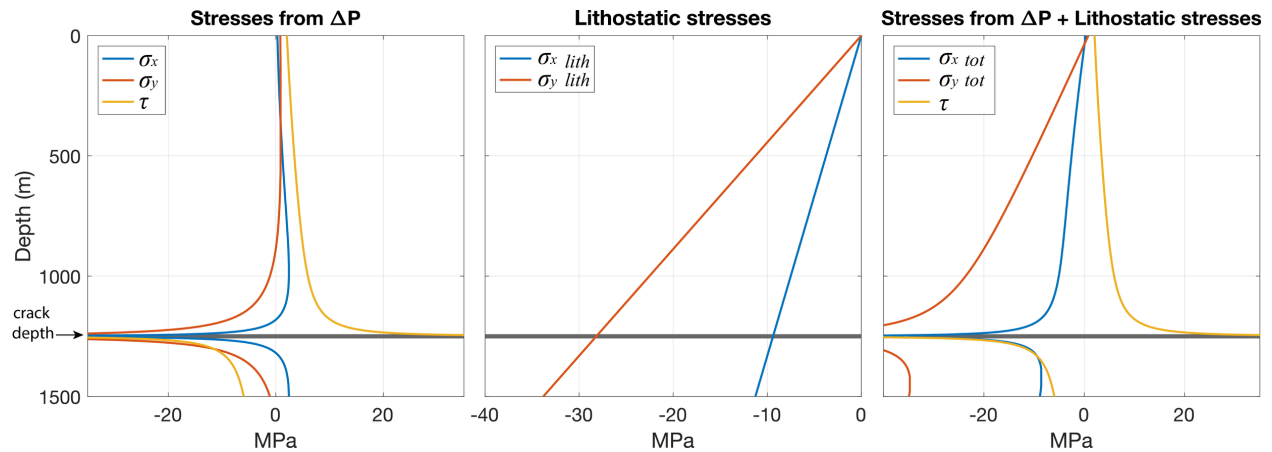


Figure 3.9. Modeled stress profiles for normal stresses σ_x , σ_y , and shear stress τ with depth along a vertical plane through the end of a pressurized two-dimensional crack located at 1250 m (horizontal gray line) with a pressure change in the crack of ~ 18 MPa. Left: predicted stress due to the pressure change ΔP in the crack only. Center: Lithostatic stress contribution for the normal stresses with $\rho g y \nu / (1 - \nu)$ for σ_x and $\rho g y$ for σ_y , where y varies with depth below the surface, and $\nu = 0.25$ and $\rho = 2300 \text{ kg m}^{-3}$. Right: Combined stresses due to ΔP and the lithostatic contribution; profiles are acquired from Figure 3.8. Note the sign convention for the stresses is tension-positive.

The total drop in magma pressure was used as an input to equations (3.7)–(3.9) to calculate the stress distributions in the vicinity of a pressurized crack (Fig. 3.8). The pressure is input as a negative value. The lithostatic stress contribution that varies with depth was added to the normal stress components only. The vertical lithostatic stress contribution ($\sigma_{y\ lith}$), is defined as ρgy , and the horizontal lithostatic stress contribution ($\sigma_{x\ lith}$) as $\rho gy\ \nu/(1-\nu)$, where y varies with depth below the surface ($y = 0$ at the surface and $y = h$ at the crack depth), ν is the Poisson's ratio of 0.25, and ρ is the rock density of $2300\ \text{kg m}^{-3}$. Lithostatic stresses are compressional and are therefore modeled as negative to be consistent with the tension-positive convention. We assume the lithostatic contribution to the shear stresses in the vertical plane is zero. We further assume that the vertical plane passing through the edge of the horizontal crack represents the vertical fault bounding the cylindrical block, thus the shear stresses along this profile represent the shear stresses acting on the fault. Figure 3.9 shows the modeled stresses along this profile for normal stresses σ_x and σ_y , ambient stresses σ_{xlith} and σ_{ylith} , total normal stresses σ_{xtot} , σ_{ytot} , and shear stress τ with depth along a vertical plane through the end of a crack located at the best-fitting depth of 1250 m and best-fitting pressure change of ~ 18 MPa. At the crack tips (or edges of the magma sill) the normal stresses decrease and shear stresses increase sharply with depth as the crack is depressurized (Fig. 3.9). Lithostatic stresses decrease linearly (consistent with the tension-positive convention) and are greater in the vertical direction. Combining the lithostatic stresses with the normal stresses due to the pressurized crack gives the total stresses.

3.6. Relating stress and magma pressure

In the case of the two-dimensional model, the shear stress distribution along a vertical plane intersecting the edge of the pressurized crack (Fig. 3.9) represents the shear stresses along the height of the bounding fault surrounding the cylindrical rock column. The average shear stress is found by taking the mean of this distribution. The three-dimensional solution is found by multiplying the resulting stresses due to the crack pressure change only, by $2/\pi$, and adding the lithostatic stress component to this. The rock column height is defined to be the depth of the sill.

The best-fitting pressure change increments from the penny-shaped crack model of the GPS data were summed to produce a magma pressure time series. Using these results, the evolution of average shear stress over time was calculated for each best-fitting pressure increment using the two and three-dimensional model solutions (Fig. 3.10). The shear stress evolution was also calculated using the force balance approach using equation (3.6). Figure 3.10 shows that both approaches result in increasing shear stress with decreasing pressure. The two-dimensional model consistently predicts higher shear stresses than those derived from the force balance equations, but the shear stresses with the correction for three dimensions fits the force balance curve closely. The average shear stress from the two-dimensional model at the time of collapse is ~ 8 MPa, while the force balance and three-dimensional shear stresses give a value of ~ 5 MPa.

3.7. Discussion and conclusions

The relationship between shear stresses and magma pressure is key to understanding the processes driving caldera collapse events at basaltic volcanoes [e.g., *Michon et al.*, 2007, 2009]. At Miyakejima in 2000, Piton de la Fournaise in 2007, and Kīlauea in 2018, deformation data reveal inward deflation around the caldera leading up to the collapse. This pattern likely reflects the continuous withdrawal of magma that decreases the pressure in the reservoir, and increasing stresses acting on the ring faults [*Ukawa et al.*, 2000; *Staudacher et al.*, 2008; *Michon et al.*, 2009; *Peltier et al.*, 2009; *Neal et al.*, 2019].

The 1Hz GPS data that we processed are particularly useful for investigating the deformation over the short time period of the earthquake and immediately following it. Although we did not model the earthquake and collapse related displacements, there are interesting observations revealed by this dataset. The mean displacement vectors of the stacked GPS data appear radially outward with almost the same orientation as the deflation displacement vectors. Sudden outward deformation during caldera collapse is considered to be caused by elastic rebound of the edifice as a result of the slip on the fault [e.g., *Michon et al.*, 2007, 2009]. Our analysis of the stresses (which are greatest near the crack tips) suggests that the fault likely begins to rupture at depth and propagates up over time; the 1Hz data reveal the duration of

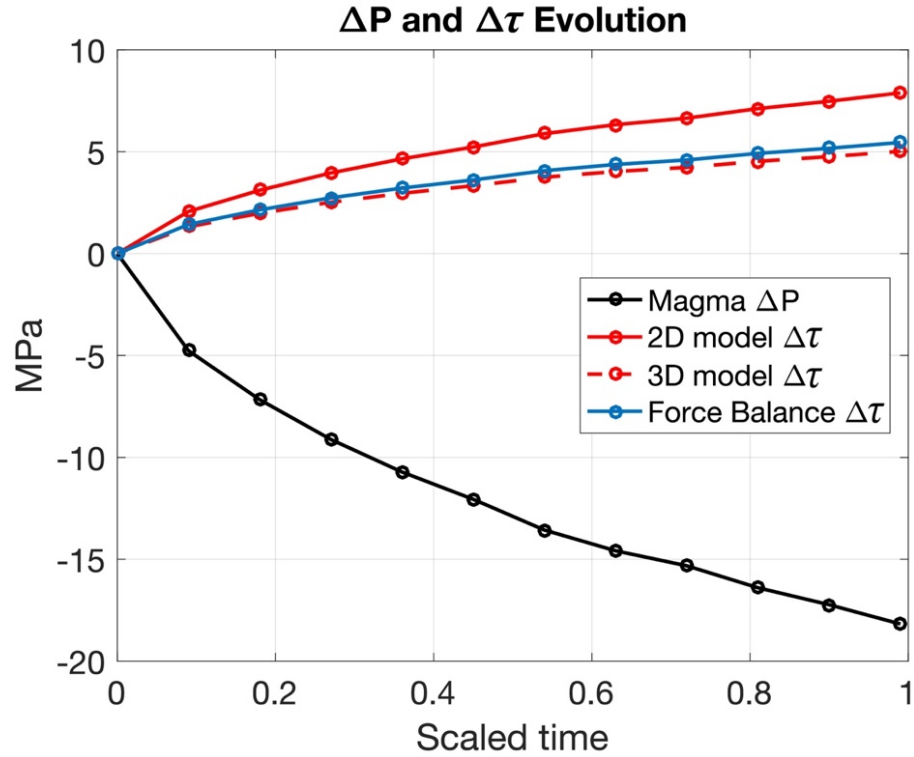


Figure 3.10. Magma pressure and shear stress evolution over deflation period of collapse events. Pressure changes were predicted using best-fitting sill parameters. Force balanced derived shear stress $\Delta\tau$ is calculated using equation 3.6. The 2D model $\Delta\tau$ is calculated from the mean of the shear stresses profile along the edge of a crack shown in Figure 3.9. The 3D model applies a three-dimensional correction to the 2D model by multiplying the resulting stresses by a factor of $2/\pi$.

collapse to be ~ 10 s. If the entire fault surface lost its shear strength instantaneously, and the caldera block collapsed in freefall, it would take only ~ 1 s, but these GPS data show that the block is not collapsing in freefall. The fact that the outward motion lasts for several seconds means that the fault is not failing instantaneously, but instead fails over a time interval consistent with the propagation speed of the front of the fault rupture.

Our analysis from modeling the deflation period between earthquakes produced two main results. First, the evolution of magma underpressure, based on the GPS data, decreases approximately exponentially over the time leading up to collapse and has an inverse relationship with the predicted average shear stresses. These are related by a constant of proportionality dependent on the depth and radius of the sill (height and radius of the cylindrical block). The exponential-like pressure decrease is a characteristic signal of a draining magma reservoir, which agrees with previous propositions from other volcanoes regarding the cause of deflation [Staudacher *et al.*, 2008; Michon *et al.*, 2007, 2009]. Evolution of shear stresses predicted from the force balance formulation are larger than those predicted by the analytical equations for a two-dimensional pressurized crack. The shear stresses corrected for the three-dimensional case using a scale factor, however, agree very well with the force balance results. The regularity of collapse events over this time period suggests a critical magma underpressure at which failure occurs, which these results suggest is ~ 18 MPa for a shear modulus G of 3 GPa. The second result is that the stress analysis indicates that the stresses are greatest at the crack tips (magma sill edges), and decrease along the length of the vertical fault. This indicates that failure likely begins at depth and propagates up with increasing time and underpressure, rather than occurring along the entire length of the fault at the same time. This is consistent with the 1Hz GPS data during the time of collapse, which suggests failure propagating along the fault. Within our analysis this indicates that the strength of the fault is likely to be the controlling factor for the failure and collapse.

The mechanisms driving these caldera collapse events are still not entirely understood. In reality the geometry of the system is far more complex than the simplifications we have made in this work, but we have shown that these simplified models provide useful insights into the

processes controlling collapses. Expanding the two-dimensional pressurized crack model to a full three-dimensional penny-shaped crack model could provide further insight to the stress distributions and material properties of the rock at the time of failure.

CHAPTER 4. EFFECTS OF VARIATIONS IN LAVA CHANNEL GEOMETRY ON FLOW DYNAMICS, EVOLUTION, AND LENGTHS

In preparation for submittal as:

Anderson, A.N., Fagents, S.A. and Baloga, S.M. (in preparation) Effects of Variations in Lava Channel Geometry on Flow Dynamics, Evolution, and Lengths. To be submitted to Bulletin of Volcanology.

Abstract

The downstream thermal and morphological evolution of channelized lava flows are influenced by a variety of factors that are important for understanding potential volcanic hazards for communities at risk. Three such factors are changes in underlying slope, changes in channel width, and lateral changes in flow path direction, which can disrupt the flow surface crust and cause enhanced cooling, significantly affecting the distance the flow can travel. A thermal model is developed and applied to examples of surface crust disruption observed in images of active Hawaiian lava flows from the 2018 eruption of Kīlauea Volcano. The current model estimates the evolution of core temperature of a flow along its length due to changes in surface crustal coverage caused by narrowing and widening of the channel. Conservation of volume requires a combination of changes in flow depth and velocity to accommodate a change in channel width. A width decrease is found to result in an increase in velocity and hence in the surface shear stresses, which act to inhibit formation of or destroy surface crust. The primary result is that a narrowing channel increases the surface area of exposed incandescent lava along the channel walls, where shear stresses are greatest. A widening channel decreases the surface area of exposed lava. These results are used in the thermal model to calculate changes in flow core temperature with distance, showing that even small changes in lava core exposure can have significant influences on flow rheology, and ultimately the final length and morphology of the flow.

4.1. Introduction

The dimensions and morphologies of lava flows are controlled by a variety of factors, including composition, effusion rate, erupted volume, heat loss, rheology, crystallinity, and topography. These key parameters and the extent to which cooling limits flow behavior have been discussed theoretically in many studies [e.g., *Walker, 1973; Pinkerton and Wilson, 1994; Griffiths et al., 2003; Cashman et al., 2006; Harris et al., 2009*]. These factors are important for understanding the potential volcanic hazards for communities at risk. Lava flows typically traverse variable topography with breaks in slope and changes in width and flow path direction, which can influence the lengths and dimensions of the flow [*Glaze et al., 2014*]. Lower viscosity lavas (e.g., basalts) can be more sensitive to these types of topographic effects than higher viscosity lavas such as dacites and rhyolites, which are predominantly influenced by larger-scale topographic changes.

When relatively fluid lava flows are sufficiently fed and persist long enough, a central channel confined by embanking levees develops. In general, lava flowing within the channel develops a progressively greater areal coverage of cooled surface crust and diminishing exposure of hot incandescent lava with distance, reflecting the balance between surface cooling and processes that act to disrupt the surface crust. Three influences on the fractional exposure of the hot component of channelized lava flows can be calculated theoretically. The effects of changes in width, lateral direction, and underlying slope on the formation of surface crust and thermal dynamics have recently been addressed by a small number of studies [*Cashman et al., 2006; Valerio et al., 2011; Glaze et al., 2014*]. *Cashman et al.* [2006] and *Valerio et al.* [2011] investigated the formation of crust due to bends in flow path direction, while *Glaze et al.* [2014] modeled the exposure of incandescent lava due to the turbulence generated by breaks in slope.

In this paper, we examine the influences on flow evolution of changes in channel width. Such changes can disrupt the surface crust, thus increasing the areal fraction of hot, radiating lava. We develop and apply a basic thermal model to examples of surface crust disruption observed in images of active lava flows. While some of the analysis builds on previous theoretical analysis and field studies [*Glaze et al., 2014*], new insights are now obtained from the

recent eruption of Kīlauea [Neal *et al.*, 2019]. The model we use here estimates the evolution of core temperature of the flow along its length due to changes in surface crustal coverage caused by channel width variations. Surface crust disruptions caused by lateral changes in flow path direction are also discussed qualitatively. We show that enhanced heat loss as a result of even small changes of lava core exposure can have a significant influence on flow rheology, and ultimately on the morphology and final dimensions of the flow.

4.2. Background

Lava flows cool by radiation and convection from the surface, and by conduction through their base, to channel walls and through crust [e.g., Murase *et al.*, 1970; Danes, 1972; Hulme, 1982; Dragoni, 1989; Crisp and Baloga, 1990; Cashman *et al.*, 1999]. At high temperatures, radiative losses exceed convective fluxes because of the T^4 dependence of radiative flux. Conductive losses to the base and walls of the channel are less significant than surface heat losses [Fagents and Greeley, 2001; Quarenì *et al.*, 2004].

Upon eruption, as an initially incandescent channelized lava travels away from the vent, the surface cools rapidly and starts to develop a solid crust over portions of the flow within seconds [Crisp and Baloga, 1990; Harris and Rowland, 2001; Harris *et al.*, 2009]. With time (distance) the exposed incandescent lava is confined to progressively smaller proportions of the total flowing surface area, presenting as cracks or hotter zones among cooler crustal components. The areal coverage of crustal material is controlled by the balance between cooling and factors that act to destroy the crust, such as shearing at the margins or transient changes in flow dynamics due to interaction with topography.

Figure 4.1 shows a typical configuration for a channelized lava, in which incandescent lava is clearly visible in the marginal shear zones flanking a central low-shear region of greater crustal coverage. Even if the fractional area of incandescent lava is small with respect to crustal coverage, radiative losses from those hot surfaces can be substantial [Dragoni, 1989]. Once a well-developed crust forms, radiative losses diminish and convective heat transfer from the upper surface is moderated by the rate of conductive heat transfer through the crust, which has a

low thermal conductivity [Cashman *et al.*, 1999]. A well-developed surface crust preserves the flow mobility by insulating the hot interior core of the flow, allowing it to travel significant distances until the lava supply ceases or the core cools sufficiently to inhibit further advance.

Lava flow emplacement models typically quantify the proportion of hot lava exposed at the surface as a fraction (f) of the total active lava area, which radiates at approximately the core temperature, surrounded by a negligibly radiating fraction ($1-f$) of flow crust [Pieri and Baloga, 1986; Baloga and Pieri, 1986; Crisp and Baloga, 1990]. Larger f values correspond to higher radiation rates, so that disturbances to the surface crust that increase f will lead to enhanced cooling, which can significantly affect the evolution of flow characteristics [Moore, 1987; Crisp and Baloga, 1990; Harris and Rowland, 2001]. In reality there is a range of lava temperatures at the flow surface [Wright *et al.*, 2003]; the treatment as two thermal components is a necessary simplification of nature.

Previous models have addressed the effects of changing surface crustal coverage on lava flows. The FLOWGO model of Harris and Rowland [2001] relates the fraction of crustal coverage to the flow velocity, with steeper slopes inducing increased velocities, which is inferred to lead to breakup of surface crust. The role of slope breaks in disrupting surface crust was examined by Glaze *et al.* [2014] using a mechanics model to estimate the rotational energy induced within the flow due to a sudden increase in slope, and to calculate the extent of crustal disruption resulting from the eddying flow. In both of these studies, the fraction of exposed lava core is used to quantify the radiative heat loss from the flow.

Narrowing of the channel is observed to cause brightening along the channel walls, indicative of crustal breakup (Fig. 4.1). In this case, conservation of the volume flux of lava through a narrower channel will lead to combination of a greater flow thickness, and higher velocity. We show in section 4.4.2.1 that the velocity increases substantially to compensate for this narrowing (the flow thickness less so), and that this increases surface shear stresses experienced by the flow towards the channel walls, again leading to breakup of crustal plates and increases in core exposure fraction f .

Lateral redirections in flow path direction also result in brightening of the channel near the bend apex where the surface crust is disrupted (Fig. 4.1). By analogy with fluvial systems, circulation within the flow caused by inward directed forces exerted by the outer channel wall on the lava results in higher velocities toward the outside bend. The increase in velocity increases the shear stresses which tear apart the crust and expose more of the hot flow core.

Cashman et al. [2006] built upon the work of *Griffiths et al.* [2003] by using polyethylene glycol (PEG) in analog simulations of lava channels to investigate the influence of changes in flow width and direction on crustal disruption. They argue that disruption of solidified crust is caused by local changes in flow acceleration due to these non-uniform channel features. They find that for lower effusion rates the surface of the flow crusts over, forming a solid roof, and that for higher effusion rates a mobile crust forms along the channel center separated from the walls by uncrusted shear zones. Within the shear zones, granulating material was observed to move vertically up and down the channel walls as the flow propagates, which is interpreted to be a consequence of thermal convection, with hot fluid rising and cooling at the surface forming new crust which then breaks, founders and sinks. They suggest that it is these thermally convecting cells that cause breakage of the surface crust at the shear zones. On the assumption that thermal convection is taking place, calculations of Rayleigh number are used to suggest that more vigorous thermal convection occurs in higher mass flux flows.

Here we consider the importance for lava crustal disruption of three-dimensional fluid dynamical effects that are known based on observations of active lava flows. We propose that the dynamics of the fluid itself should overwhelm any propensity towards thermal convection in inducing internal circulation. Complementary to the work of *Glaze et al.* [2014], we present a model that relates changes in the fraction of exposed incandescent lava within a channel to changes in the magnitude of shear stresses towards the channel walls as a flow experiences narrowing or widening of the channel. We also qualitatively address the effects of channel bends on surface crust disruption.

4.3. Observations of active flows from Kīlauea, 2018

We analyzed images obtained from Unmanned Aerial Vehicle (UAV) videos of the 2018 eruption of Kīlauea Volcano, Hawai‘i for channelized sections of the Fissure 8 lava flow (Fig. 4.1), acquired by USGS staff during eruption monitoring operations. Videos were taken during night flights on June 26 and July 22, 2018, and show portions of the lava channel with substantial width variations and a distinct $\sim 90^\circ$ bend. The illumination conditions and nadir viewing geometry make these videos ideal for analysis. The nadir view avoids the geometrical distortion inherent in images acquired at off-nadir viewing geometries, and the low lighting conditions highlight the contrast between the darker crustal material and the bright incandescent lava. Distinguishing between dark and bright areas of the flow is critical for obtaining the model parameter f , the fraction of exposed hot core. From this dataset we measured channel widths and lengths, and obtained estimates for f along the flow length. Channel dimension measurements were used as model parameter inputs, and measured f values were compared to model predictions of f .

4.3.1 Methods of data analysis

Selected video frames showing the regions of interest were imported into a vector graphics editor (Adobe Illustrator) and rectangular boxes of uniform downstream dimension were fitted across the channel width at numerous downstream locations. Each boxed station represents an incremental step in the model. The scale was obtained by registering images with USGS thermal maps produced during the time of the UAV flights, and Lidar data from July 2018, resulting in a conversion factor of pixels per meter. The channel widths and lengths at each station were measured in pixel distances and converted to meters. Because the videos were taken at night, only the shape of the channel margins could be used for georeferencing, thus we acknowledge that there is some uncertainty in the measured distances.

The boxed stations were cropped and analyzed in a raster graphics editor (Adobe Photoshop) to obtain values for f . For each station, the image contrast was increased to 100% and a threshold applied, which converts the image to a binary image with all pixels lighter than the threshold set to white, and all pixels darker than the threshold set to black. The white pixels

represent the exposed incandescent lava, and the black pixels represent cooler crust. The white pixel count was divided by the total pixel count to give a representative f value for each station. Real lava flows show a continuum of lava surface temperatures, reflecting varying degrees of crustal coverage, including dark rubble, red and orange viscoelastic “skin”, bright yellow and white hot flow interior, and a range of values in between. Thus the thresholding of the flow into two components necessarily simplifies the system by considering that the yellow to white pixels represent the exposed core.

4.3.2 Selected features

The June 26, 2018 UAV flight traveled along the channel length in the direction of the flow, maintaining a constant orientation and nadir view. This allowed for still frames to be extracted and merged to produce a composite view of the channel (Fig. 4.1). From the composite image we identified three locations exhibiting distinct variations in channel width and one location exhibiting a significant lateral redirection in flow path (90° bend). The July 22, 2018 flight remained stationary over a section of the channel exhibiting an increase channel width. Frames of these key locations were extracted from the videos for analysis.

4.3.2.1 Case 1

This section of the flow shows relatively constant widths upstream and downstream of a single distinct constriction in the flow width (Fig. 4.2a). The flow path direction is straight with no significant redirections. The widest stations downstream (14–20) are noticeably darker with less exposed bright yellow core and more dull red to black coverage. Margins of the flow at the narrowest stations (9–11) are visually bright but their fraction areal coverage compared to crust is not enough to cause significantly increased f values. Instead, the measured f values remain relatively constant at the constriction, and decrease as the width increases.

4.3.2.2 Case 2

The flow at this section shows small variations in channel width with distance with an overall trend of gradual narrowing and widening (Fig. 4.2b). The measured widths decrease and

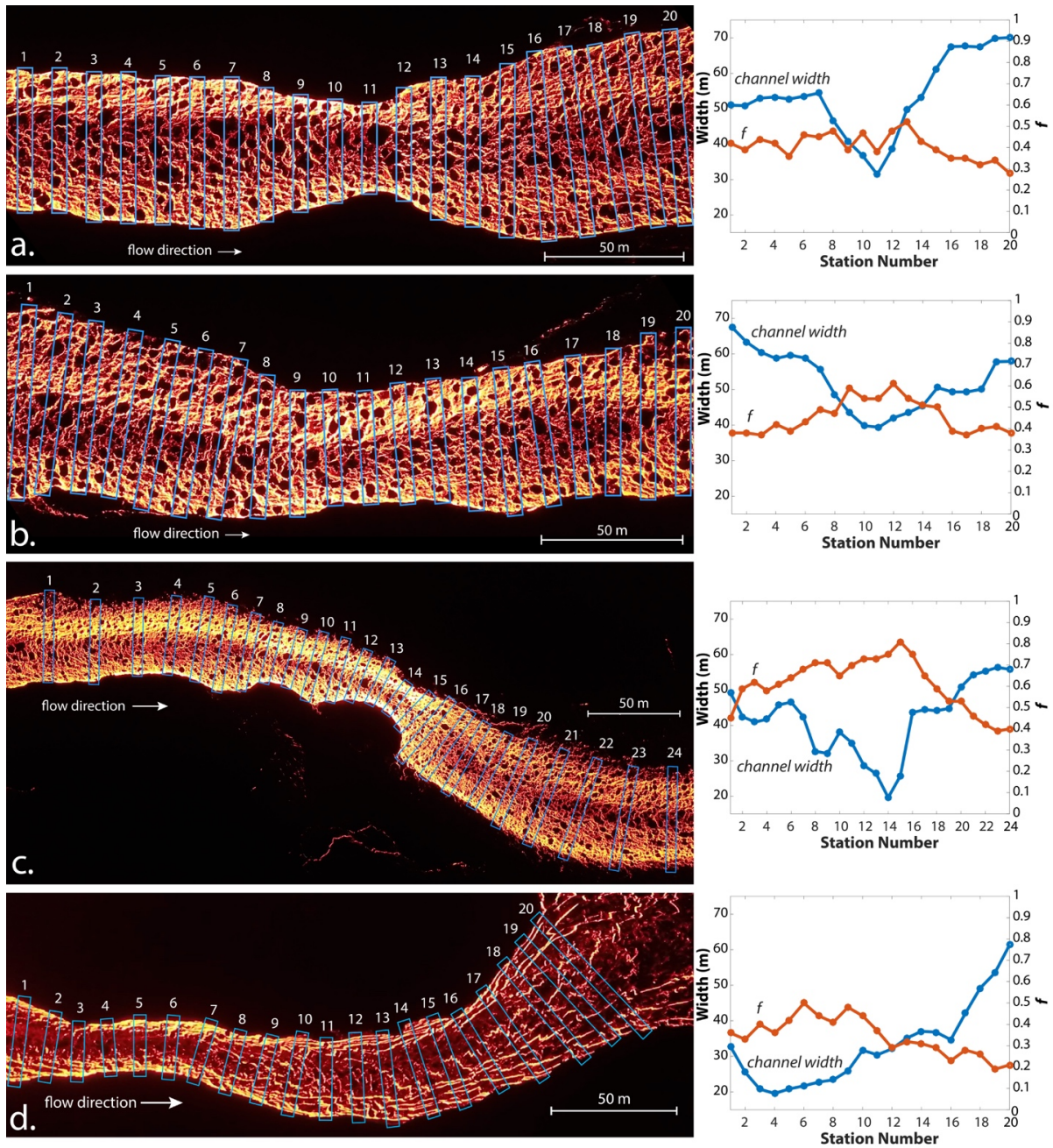


Figure 4.2. Left: Sections of Kīlauea lava channels, 2018, showing variations in channel width. Blue numbered boxes define stations used as model increments. Right: Measured channel width (blue) and average fraction (f) of exposed incandescent lava core (orange) determined by image analysis for each station. Station numbers correspond to images on left.

increase gradually, as opposed to the more abrupt constriction at the Case 1 and 3 locations. The narrowest stations (9–12) appear to be brighter yellow in color, and the crust at the center of the flow narrows with the narrowing channel width and widens as the flow width increases again. Crust at the center also appears more broken up at the narrow stations, exposing slivers of bright yellow core, whereas the crust at the wider stations is more coherent dark and red rubble with fewer noticeable yellow slivers. The measured f values represent well the observed increase in brightness at the narrowest stations of the channel; the f values increase as the channel narrows and decrease as the channel widens.

4.3.2.3 Case 3

One distinct constriction is observed in this section of the flow, with lesser variations in channel width exhibited upstream (Fig. 4.2c). Gentle redirections in flow path are superimposed on width variations though these are less obvious than the constriction. Protrusions from the confining channel levees cause the channel to narrow significantly at station 14, and then widen rapidly. The narrowest station is noticeably brighter than the wider stations, with the crust at the centerline also narrower and less cohesive than other surfaces of the flow. Crustal coverage resumes very shortly thereafter. The measured f values confirm the visual brightening, with the highest values corresponding to the narrowest stations. Again the f values are inversely correlated with the channel width measurements.

4.3.2.4 Case 4

The channel here begins narrow and then widens substantially (Fig. 4.2d). There are gentle bends superimposed on the flow direction but we consider these less significant than the variation in width. Crustal coverage at the center remains relatively coherent and narrows at the narrowest stations. The narrowest stations show bright yellow margins of exposed material, whereas the wider stations have only slivers of incandescent core exposed between plates of darker crusted material, and lack a well-defined zone of exposed core at the margins. The f values reflect this and are higher at the narrower stations and decrease as the flow widens.

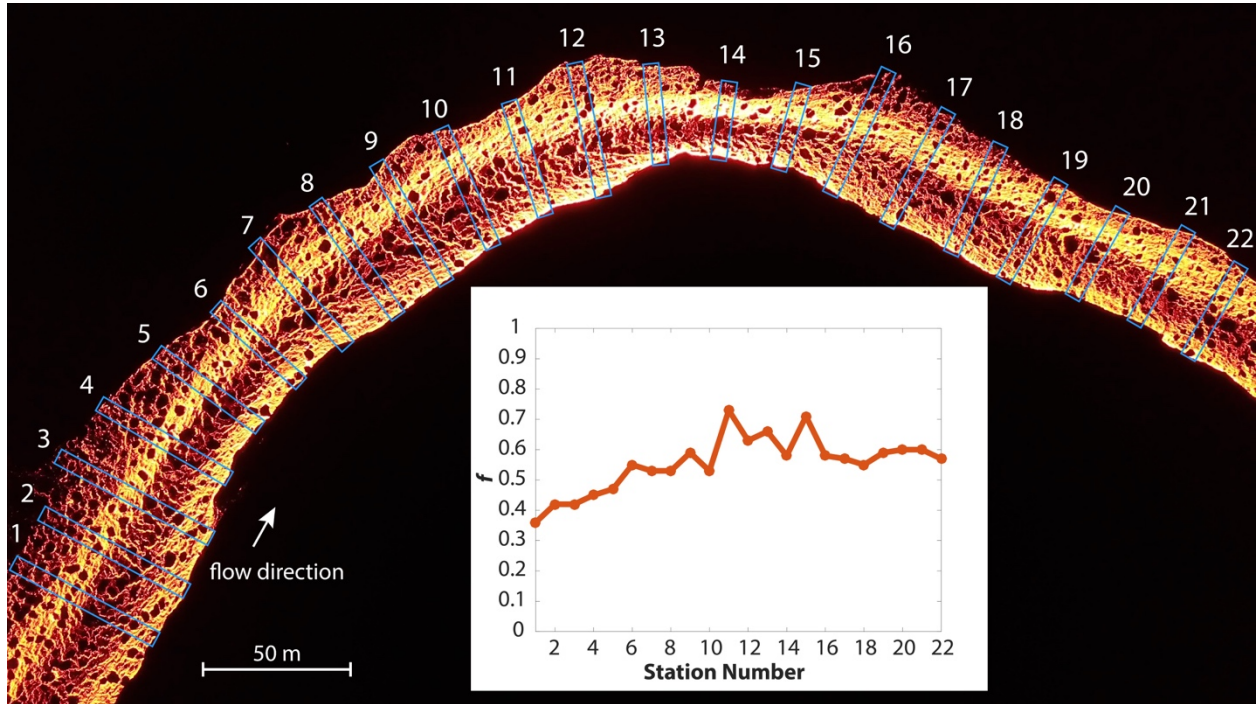


Figure 4.3. Bending segment of Kīlauea lava channel, June 26, 2018. Blue numbered boxes define stations used as model increments. Inset plot shows average fraction (f) of exposed incandescent lava core determined by image analysis for each station.

4.3.2.5 Case 5

The composite view of the lava channel from June 26, 1018 shows clearly the 90° bend in the flow path direction (Fig 4.1). This selection focuses on the apex of the bend, with stations 5–17 comprising the curved flow path and the remaining stations comprising the straighter flow path directions (Fig. 4.3). As the flow path is turning the central crust portion of the channel begins to shift noticeably towards the inner bank, exposing brighter material on the outer margin of the bend. This suggests that more shearing is taking place on the outer wall of the bend, possibly due to acceleration around the bend and interior circulation. There is a short reach of channel narrowing superimposed on the bend near station 14, which is also one of the brightest stations along the flow.

4.4. Model for flow evolution

4.4.1 Model background

The motivation for the model is to relate flow cooling due changes in crustal coverage to changes in channel geometry (i.e., at width changes or bends), and hence determine the implications for cooling and flow dimensions. To achieve this objective, we develop and solve an ordinary differential equation for the core temperature as a function of distance from the source. First, we present the relationships between key parameters used in the model setup for the case of flow in a straight channel of constant width, and in section 4.4.2 we adapt the model to account for variations in channel width.

The model initially considers a steady state flow having velocity u , and radiating at the lava core temperature T_0 primarily through a fraction f of exposed incandescent lava, surrounded by a negligibly radiating fraction $(1-f)$ of flow crust. We consider a control volume within the channelized lava flow having dimensions of height h , width w , and length dx (which remain constant in this scenario), such that the control volume is defined as $V = hwdx$ (Fig. 4.4), and the mass as $m = \rho hwdx$. The heat H contained with this mass of lava is obtained by multiplying by the specific heat of the basalt C_p and the temperature T , giving $H = C_p m T = \rho C_p T h w dx$. The time rate of change of the heat in the control volume is determined by thermal radiation from the

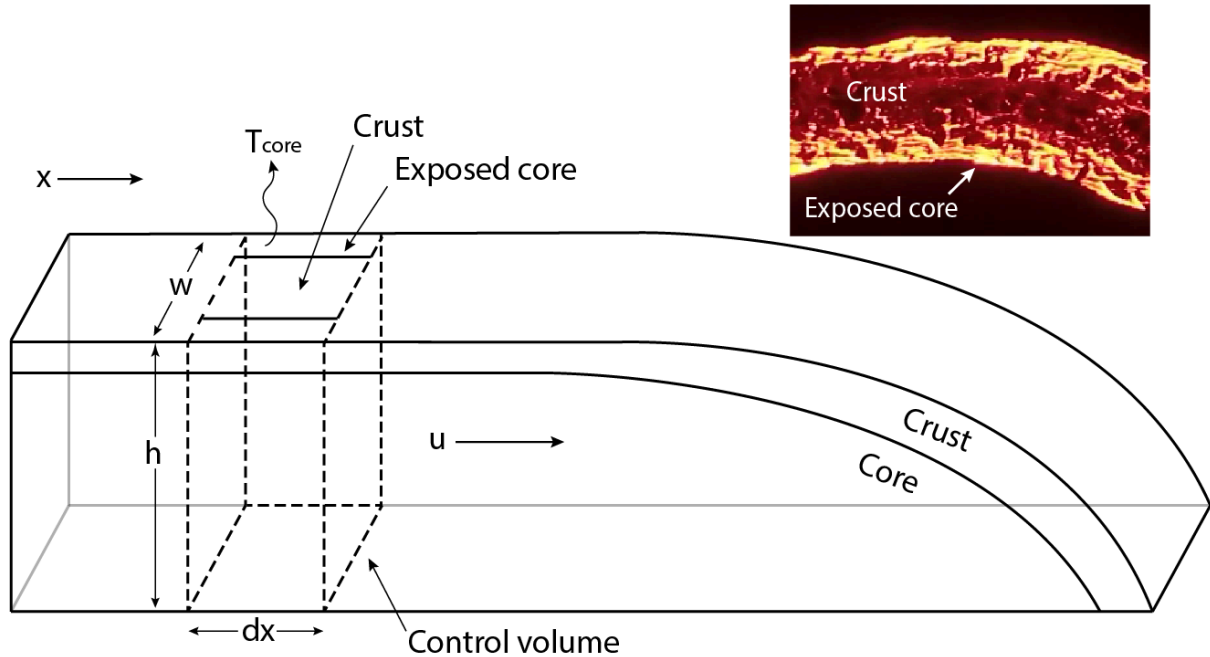


Figure 4.4. Cross sectional view of schematic lava flow showing control volume outlined by dashed lines, modified from *Crisp and Baloga* [1990]. Flow is traveling in the x direction with velocity u . Control volume dimensions are width (w), height (h), and length (dx). Surface of control volume shows fraction of exposed core radiating at temperature T_{core} with remaining fraction occupied by surface crust. Top right: Photograph of channelized lava flow from Kīlauea volcano, 2018. Note exposure of incandescent material along flow margins.

surface of the control volume (in J s^{-1}). The governing equation that expresses this heat balance is written as

$$\frac{dH}{dt} = \frac{d}{dt}(\rho C_p T h w dx) = \varepsilon T^4 f w dx, \quad (4.1)$$

where the radiative loss is given by the Stefan-Boltzmann law ($\varepsilon \sigma T^4$) through a fraction f of the upper surface at temperature T . Here ε is emissivity, σ is the Stefan-Boltzmann constant, and $w dx$ is the area of the upper surface. We assume that heat loss is dominated by radiation from the exposed the hot core (because of the T^4 dependence), and that any other heat loss is negligible in comparison. For the moment we also assume that f and w remain constant along the path of the flow.

Since we are interested in obtaining temperature as a function of distance x , and changes in the eruption temperature are usually very minor, we make the replacement for dt where $d/dt = u d/dx$, and $u = u(x)$ is the average velocity as a function of distance. Making this substitution gives the differential equation

$$\rho C_p h u \frac{d}{dx}(T(x) w) = -\varepsilon \sigma f T^4 w, \quad (4.2)$$

which can be solved to give

$$T(x) = T_0 \left[1 + \frac{3\varepsilon \sigma f T_0^3 x}{\rho C_p h u} \right]^{-\frac{1}{3}}, \quad (4.3)$$

which is the core temperature of the lava flow as a function of distance.

The solution in equation (4.3) determines the final length of the flow in terms of a “cessation temperature” T_{cess} that represents the bulk core temperature at which forward motion of the flow stops. (See Appendix for discussion of defining the cessation temperature.) This yields

$$T_{cess}(x) = T_0 \left[1 + \frac{3\varepsilon\sigma f T_0^3 L}{\rho C_p h u} \right]^{\frac{1}{3}}, \quad (4.4)$$

where L is the final length of the flow when the core temperature has reached the cessation temperature. Figure 4.5 shows how downstream flow temperature varies for different values of f , such that the cessation temperature is reached at difference distances. Equation (4.4) can be rearranged to give the final length of the flow for given cessation temperature and other flow properties:

$$L = \left[\left(\frac{T_0}{T_{cess}} \right)^3 - 1 \right] \frac{\rho C_p h u}{3\varepsilon\sigma f T_0^3}. \quad (4.5)$$

The length of the flow, as indicated by equation (4.5), depends on f (which controls radiative heat losses) and will also vary depending on cessation temperature T_{cess} , velocity u , and flow depth h . A lower cessation temperature will result in a greater flow length for a given f value with all other variables held constant, and disruptions that increase f will cause the flow length to decrease (Fig. 4.6).

In general, f will decrease with distance as the crust becomes more established. However, changes in channel geometry along the flow path (constrictions or bends) that disrupt surface crust will cause f to increase for some distance in response to each disruption. Figure 4.7 shows an example of enhanced cooling due to sudden increases in f at multiple locations along the flow path. We examine in detail the consequences of crustal disruption and changing f values in the following sections.

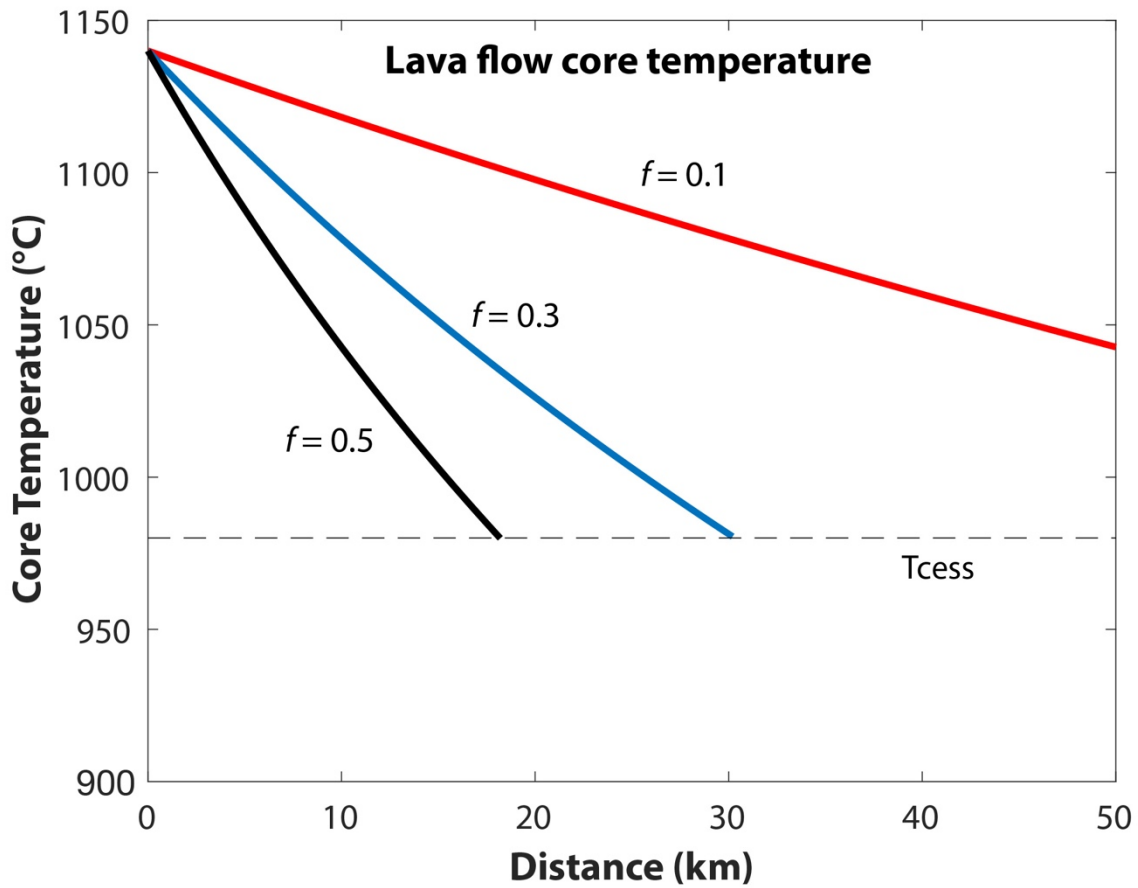


Figure 4.5. Theoretical temperature profiles along the length of a hypothetical flow for three different values of f . Red, blue, and black curves represent constant core exposure for $f = 0.05$, 0.3, and 0.5, respectively. Note that for higher values of f (larger areas of exposed core), the core temperature reaches T_{cess} at shorter distances.

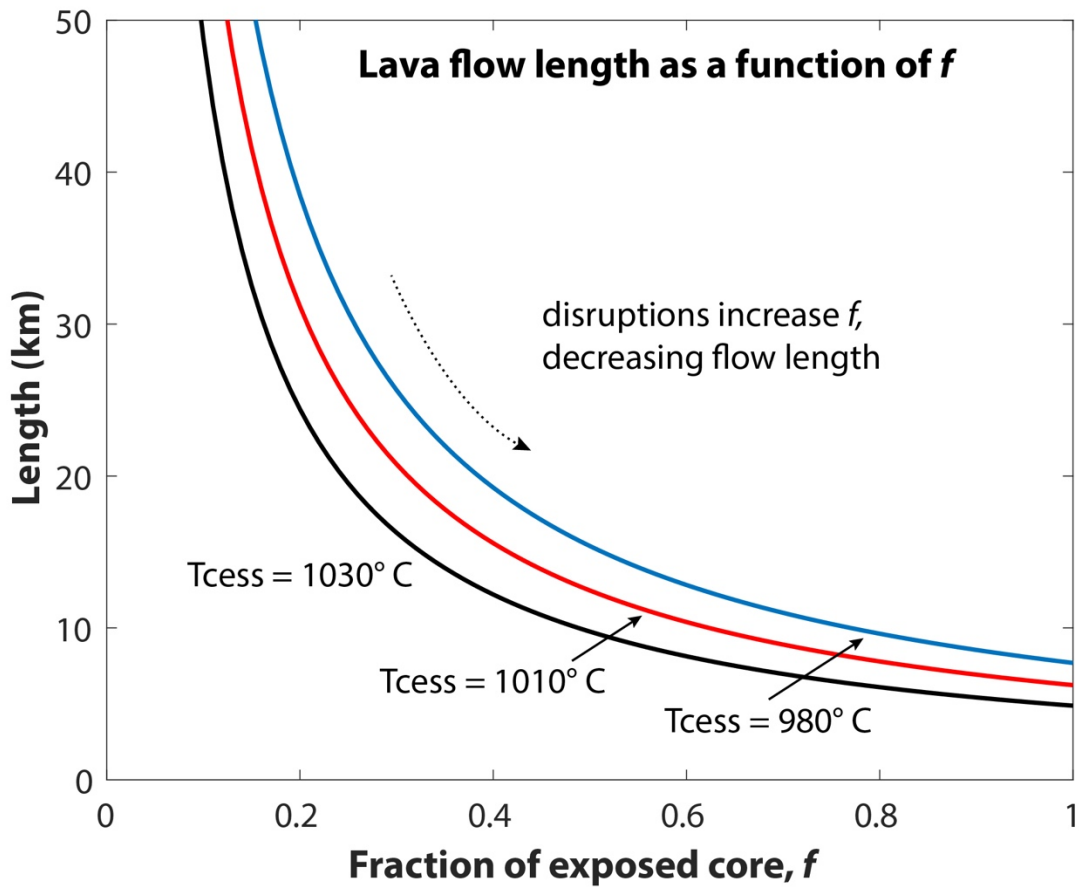


Figure 4.6. Total lengths of hypothetical flows as a function of the fraction of exposed core, f , for three different cessation temperatures (T_{cess}). Black, red, and blue curves represent T_{cess} values of 1030, 1010, and 980 °C, respectively. For a given value of f , flow length is shorter when the cessation temperature is higher. Dashed arrow shows how increases in f due to surface crust disruption would result in shorter flow lengths.

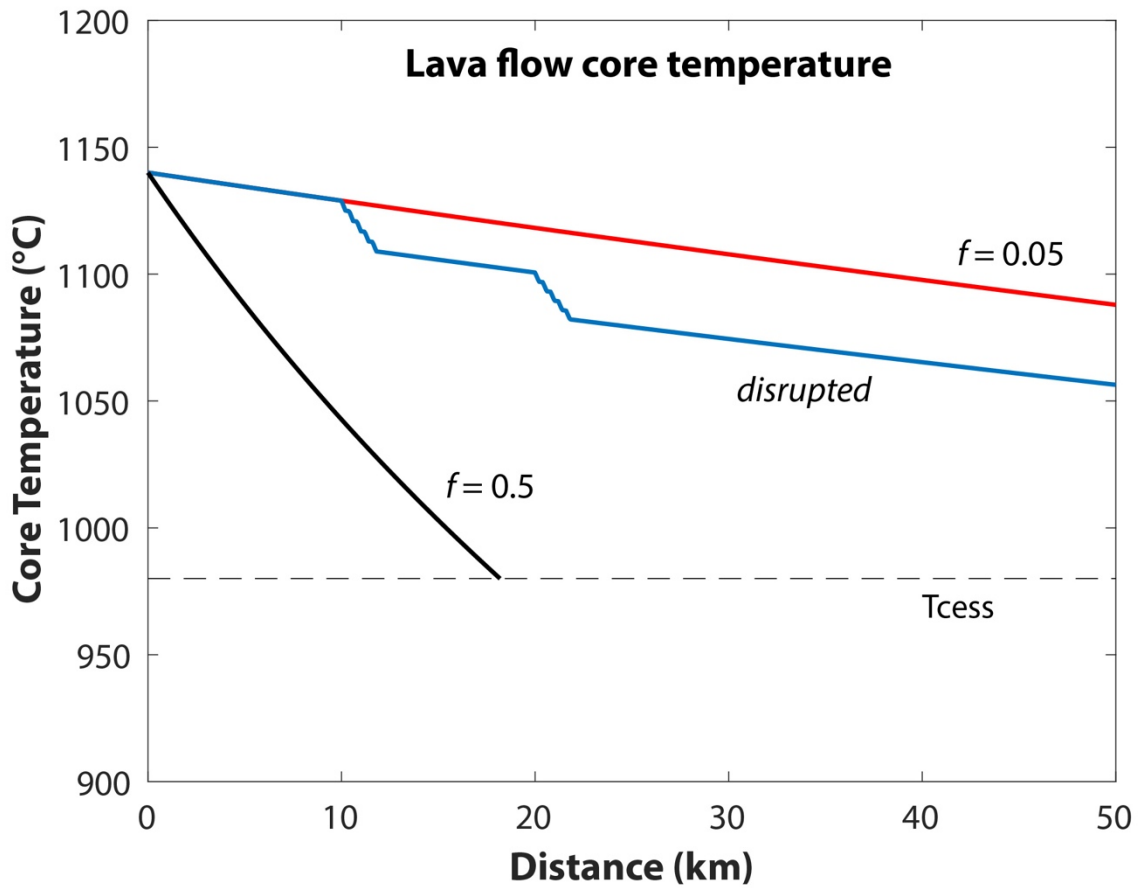


Figure 4.7. Temperature profiles along the length of a hypothetical flow for different values of f . Red and black curves represent constant core exposure for values of $f = 0.05$ and 0.5 , respectively. The blue curve shows the influence on the core temperature when the flow surface is disrupted. Five 100 m segments of disruption with $f = 0.9$ were inserted at 10 km and 20 km along length of a flow that otherwise had $f = 0.05$.

4.4.2 Model for channel width variations

The goal of this model is to estimate how the surface crustal coverage of a lava flow is influenced by narrowing and widening of the channel width with distance, and to determine the consequences for flow temperature and rheology. Within a channelized flow, bright incandescent shear zones along the channel wall represent the primary source of heat loss. When lava encounters an increase or decrease in channel width downstream, conservation of volumetric flow rate requires some combination of changes in flow depth and velocity to accommodate the change in channel width caused by the confining levees. The change in flow velocity is significant as it affects the surface shear stresses, which in turn affect the surface crustal coverage, manifested as variations in the widths of the marginal bright shear zones. Higher shear stresses will tend to break apart the insulating surface crust, whereas lower shear stresses will tend to preserve the crustal coverage. Because of the T^4 dependence of radiative heat loss, variations in the width of the incandescent margins can have a significant influence on the thermal budget of the lava flow and thus on the final dimensions and morphology.

The model considers laminar, Newtonian lava flowing at average velocity u , in a channel with depth h , and width w . The velocity is fixed at 0 m s^{-1} by a no-slip condition at the channel walls, and increases following a parabolic profile to a maximum velocity at the centerline of the flow. The channel is assumed to be symmetric about the centerline. The channel width is measured as distance y increasing from the channel center to the wall. Shear stresses are greatest at the channel walls, where the surface velocity gradient is steepest. As the average velocity increases, surface shear stresses also increase. The model assumes a critical shear stress at which surface crust is disrupted to expose incandescent lava close to the flow margins. Variations in channel width affect the flow velocity and hence the shear stresses, and therefore the proportions of surface crustal coverage and exposed lava.

The key to this approach is that the width is not a free variable; it is controlled by embanking topography created by earlier flow phases. Therefore, channel width is a known parameter that can be measured. The flow depth and velocity can then be solved in terms of the channel width and viscosity. The fraction of exposed lava is derived from equations for shear

stress and the velocity. The model considers two adjacent stations along the channel, denoted by subscript i and $i+1$. The solution for these two stations can then be applied as an iteration down flow for as long as the assumptions hold.

4.4.2.1 Channel width effects on flow depth and velocity

In steady state conditions, the volume flow rate Q of the lava flow is conserved. Using Jeffrey's equation, the volumetric flow rate for station i and station $i+1$ can therefore be set equal, as

$$Q = \frac{g \sin \theta h_i^3 w_i}{3\nu_i} = \frac{g \sin \theta h_{i+1}^3 w_{i+1}}{3\nu_{i+1}}, \quad (4.6)$$

where g is the acceleration due to gravity, θ is the angle of the underlying slope, and ν is the kinematic viscosity. Assuming that only channel width, flow depth, and viscosity differ between stations, equation (4.6) simplifies to

$$\frac{h_i^3 w_i}{\nu_i} = \frac{h_{i+1}^3 w_{i+1}}{\nu_{i+1}}. \quad (4.7)$$

The flow depth h_{i+1} , can be found by rearranging equation (4.7) to be

$$h_{i+1} = \left(\frac{\nu_{i+1} w_i}{\nu_i w_{i+1}} \right)^{1/3} h_i, \quad (4.8)$$

where flow depth h_{i+1} is expressed in terms of the flow depth h_i , and the viscosity and channel width at station i and $i+1$. The volumetric flow rate is also defined as the average flow velocity multiplied by the channel width and flow depth ($Q = u h w$). The same condition for conservation of flow rate can be applied, and flow rate at stations i and $i+1$ can be set equal:

$$Q = u_i h_i w_i = u_{i+1} h_{i+1} w_{i+1} . \quad (4.9)$$

Then the average flow velocity is given by rearranging equation (4.9), and using equation (4.8), as

$$u_{i+1} = \left(\frac{v_i}{v_{i+1}} \right)^{1/3} \left(\frac{w_i}{w_{i+1}} \right)^{2/3} u_i , \quad (4.10)$$

which yields the flow velocity u_{i+1} in terms of the velocity u_i , and the viscosity and channel width at stations i and $i+1$. Equations (4.8) and (4.10) show that a change in channel width is mostly taken up in a change in velocity (the width ratio w_i/w_{i+1} grows by an exponent of 2/3 in the velocity equation and only 1/3 in the flow depth equation). When the channel width decreases, the velocity increases, and when the width increases, velocity decreases. Flow depth increases when the channel narrows.

4.4.2.2 Channel width effects on shear stress and f

Shear stresses at the surface of a lava flow are dictated by the surface velocity profile. The shear stresses control the fraction of exposed lava, f , at the surface of the flow. A solution for f can be derived from the definition of shear stress to calculate f at each section along the flow length.

The velocity profile across the flow width is given by $u(y)$ where y is the distance from the centerline of the flow to the channel wall, and w is the total channel width. The velocity can be written for the case of laminar flow between parallel plates as,

$$u(y) = u_{\max} \left(1 - \left(\frac{2y}{w} \right)^2 \right) . \quad (4.11)$$

where u_{\max} is the maximum surface velocity at the center of the flow. Then the shear stress τ , from the centerline to the margin is related to the cross-flow velocity profile as,

$$\begin{aligned}\tau(y) &= \mu \frac{\partial u}{\partial y} = u_{\max} \mu \left[-\frac{d}{dy} \left(\frac{4y^2}{w^2} \right) \right] \\ &= u_{\max} \mu \left(\frac{-8y}{w^2} \right)\end{aligned}\tag{4.12}$$

Shear stresses increase from the centerline towards the margins, and are greatest at the shear zones where lava is flowing alongside the stationary channel walls. When shear stresses reach a critical value, the insulating surface crust tears apart exposing the incandescent lava below, resulting in bright margins along the channel walls. From equations (4.11) and (4.12), it can be shown that a narrower channel will result in a steeper cross-flow velocity profile (Fig. 4.8a), which increases the shear stress profile (Fig. 4.8b). We designate the distance from the center of the channel to the margin of exposed incandescent lava as y_{crit} (Fig. 4.9).

The fraction of exposed lava, f is then written as the difference between the channel half-width $w/2$ and y_{crit} , divided by $w/2$:

$$\begin{aligned}f &= \frac{\frac{w}{2} - y_{crit}}{\frac{w}{2}} \\ &= 1 - \frac{2y_{crit}}{w}\end{aligned}\tag{4.13}$$

The f value will be affected as y_{crit} changes due to changes in the magnitude of the shear stresses. This value for f assumes that incandescent lava is only exposed from the distance y_{crit} to the channel walls, and that the center of the channel to y_{crit} is covered by surface crust. However, real lava flows may exhibit a more complex pattern of crustal coverage at the surface due to other dynamical effects within the flow.

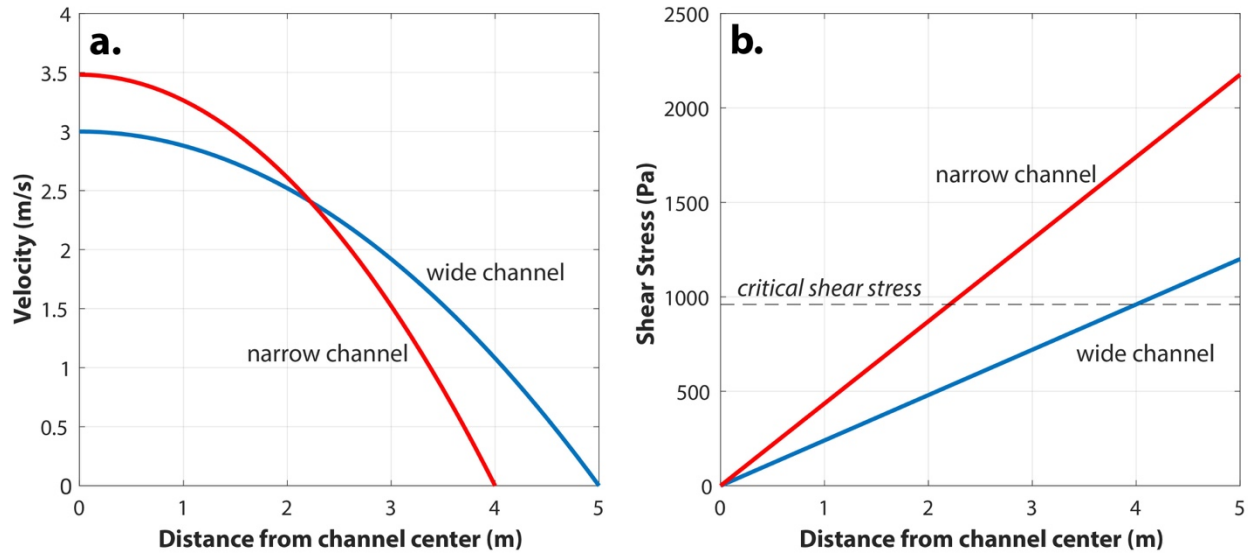


Figure 4.8. Theoretical velocity (a) and shear stress (b) profiles for wide (blue curves) and narrow (red curves) channels. Notice that the narrow channel intersects the critical shear stress at shorter distances from the channel center than the wide channel.

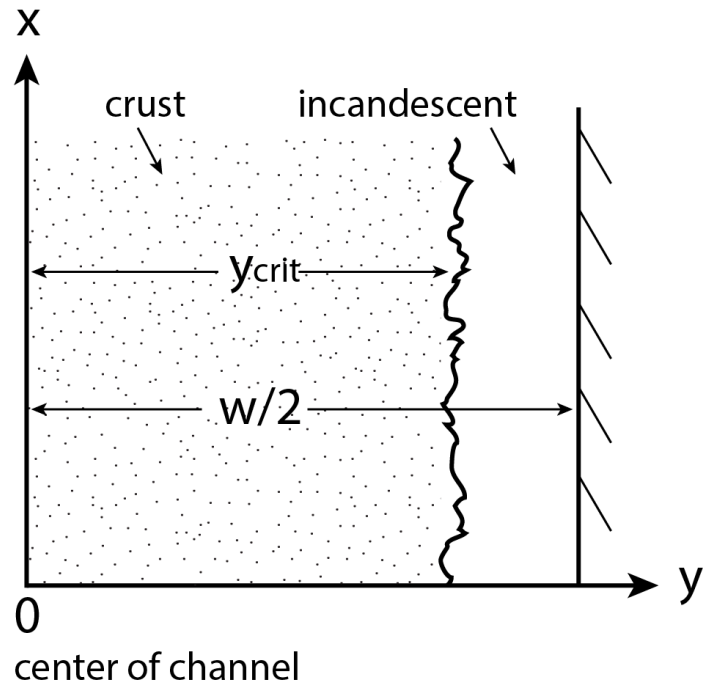


Figure 4.9. Schematic diagram of bisected lava channel showing crust at center and incandescent core material exposed at margins where crust is disrupted. Total channel width is w and y_{crit} is the distance from the channel center to the bright margin.

The critical shear stress is defined as the shear stress at which the surface crust becomes disrupted. The location y_{crit} across the channel is the distance at which the critical shear stress occurs. It can change due to the changes in channel width from station to station. If the critical shear stress remains constant, then it can be set equal from one station to the next to give,

$$\tau_{crit} = \frac{8y_{crit_i} u_{max_i} \mu_i}{w_i^2} = \frac{8y_{crit_{i+1}} u_{max_{i+1}} \mu_{i+1}}{w_{i+1}^2} \quad (4.14)$$

Solving equation (4.14) for y_{crit} at station $i+1$ gives:

$$y_{crit_{i+1}} = \frac{u_{max_i} \mu_i}{u_{max_{i+1}} \mu_{i+1}} \left(\frac{w_{i+1}}{w_i} \right)^2 y_{crit_i} \quad (4.15)$$

The relationship between the maximum velocity at the centerline and the vertically averaged flow rate is assumed to be constant. The velocity solution from equation (4.10) can be substituted into equation (4.15), and writing the dynamic viscosity μ as the product of kinematic viscosity and density $\rho\nu$ gives

$$y_{crit_{i+1}} = \left(\frac{v_i}{v_{i+1}} \right)^{2/3} \left(\frac{w_{i+1}}{w_i} \right)^{8/3} y_{crit_i} \quad (4.16)$$

Equation (4.16) expresses y_{crit} at the current station $i+1$ in terms of viscosity, channel width, and y_{crit} at the previous station i . Now, recalling the definition of f from equation (4.13), y_{crit} can be written in terms of f and w as,

$$y_{crit} = \frac{w}{2}(1-f) \quad (4.17)$$

The definition of y_{crit} given by equation (4.17) can then be used in equation (4.16) and simplified as

$$f_{i+1} = 1 - \left[\left(\frac{v_i}{v_{i+1}} \right)^{2/3} \left(\frac{w_{i+1}}{w_i} \right)^{5/3} (1 - f_i) \right], \quad (4.18)$$

which gives a solution for f at the $i+1$ station of the flow in terms of the previous f value, and the viscosity and channel width. This f value is used as an input to the temperature calculation (equation 4.3), along with the flow depth and velocity, to give the new core temperature.

4.4.2.3 Calculating core temperature

The model sets up initial parameters for calculating the core temperature at each station along the length of the flow. Channel width and the distance between each station are designated as model inputs. Equation (4.3) is used with a predefined initial temperature, flow depth, velocity, and f , to calculate the core temperature at the next station. This temperature is used to obtain the melt viscosity, which is calculated from the *Giordano et al.* [2008] model using major oxide compositions of a representative sample of the 2018 Kīlauea Fissure 8 lava flow. Viscosity is used as an input to calculate the flow depth (equation 4.8) and flow velocity (equation 4.10). Finally, f is calculated from equation (4.18). The newly calculated temperature, flow depth, velocity, and f become the new inputs used to recalculate the core temperature. The model continues incrementally for each station along the flow. Outputs are the predicted temperature, viscosity, flow depth, velocity, and f values along the flow length.

Figure 4.10 shows model outputs for two theoretical channel configurations, one with constant channel width (black curve) and f (Fig. 4.10a) and the other with a constriction in the channel (red and blue curves) (Fig. 4.10b). In the width variation case, the model predicts that f will increase when the channel narrows and decrease when the channel widens again. The primary result is demonstrated by the temperature profiles for the constant width and varying

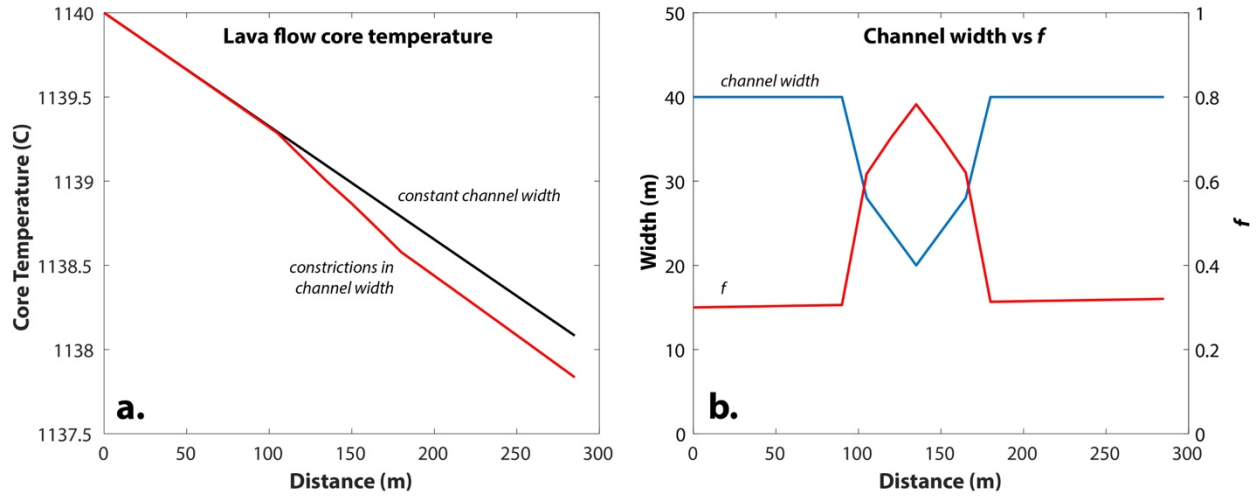


Figure 4.10. (a.) Theoretical temperature profile for a channel with constant width and f (black curve) and for a channel with a width constrictions (red curve). Notice that the temperature drops at shorter distances along the flow than for the constant width case. (b) Channel width (blue curve) and predicted crustal coverage f (red curve).

width channels (Fig. 4.10a). Because the fraction of hot core increases when the channel narrows, the core temperature drops more rapidly than when the width and f remain constant.

4.5. Results

Model outputs for each case of channel width variations (Cases 1–4; Fig. 4.2) show how predicted core temperature decreases and viscosity increases with distance, and that flow velocity and flow depth increase as channel width decreases, and decrease as channel width increases (Fig. 4.11a–d). Figures 4.11a–d compare the predicted fractions of exposed core f with the values measured from the image analysis. We also ran the model using the measured f values only, to compare the temperature, viscosity, velocity, and flow depth results. Because the velocity and flow depth equations are not directly dependent on f , the results are essentially the same for both cases. Temperature and viscosity, however, are affected by differing measured and predicted f values (Fig. 4.11).

In Case 1 (Figs. 4.2a, 4.11a), the predicted f values agree with the measured values at the first seven stations while width is still constant. However, when the channel narrows the predicted f values increase and the measured values do not change significantly. As the channel widens again, the predicted and measured f values both decrease, but the predicted values are lower than those measured. When the model underpredicts f , the model temperature and viscosity (red curves) change more slowly than the values calculated based on the measured f (black curves).

In Case 2 (Figs. 4.2b, 4.11b), the predicted and measured f values exhibit the same trend of increasing as the channel narrows and decreasing as the channel widens, but there is a 0.1–0.2 offset between the predicted and measured f values (Fig. 4.11b). The model outputs agree with the trend of crustal coverage although the fraction of exposed core is overpredicted for the entire length of the segment. This overprediction affects the temperature and viscosity, and the higher predicted f values cause the temperature to decrease and the viscosity to increase more rapidly than those derived from the measured f values.

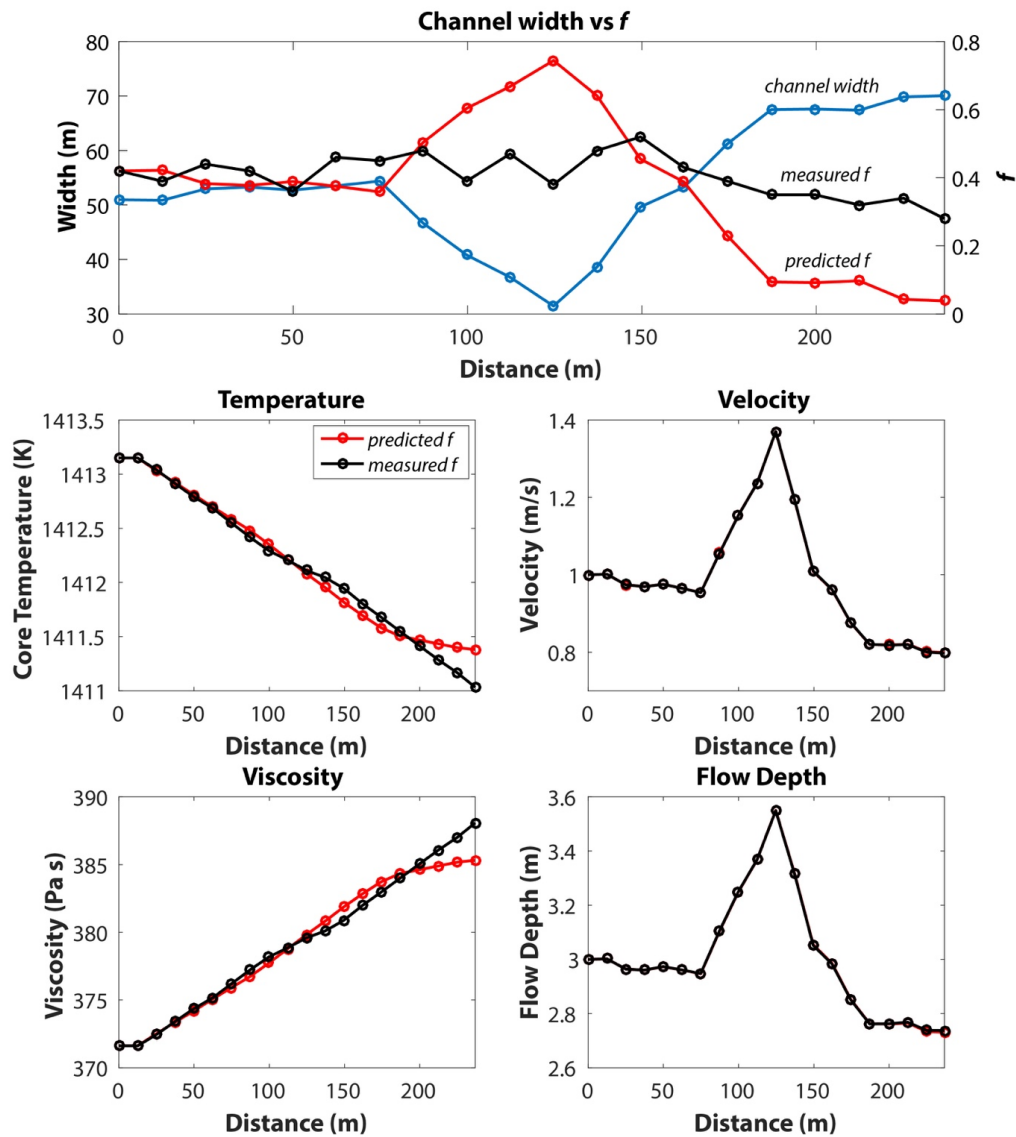


Figure 4.11a. Case 1 model outputs showing predicted fractions of hot core (f) compared to measured values versus measured channel widths with distance, and temperature, viscosity, flow velocity, and flow depth versus distance for predicted (red curves) and measured (black curves) f values. Measured f values remain relatively constant until gradually decreasing as the flow widens after the constriction near station 11. The predicted f values increase at the constriction and decrease rapidly as the flow widens.

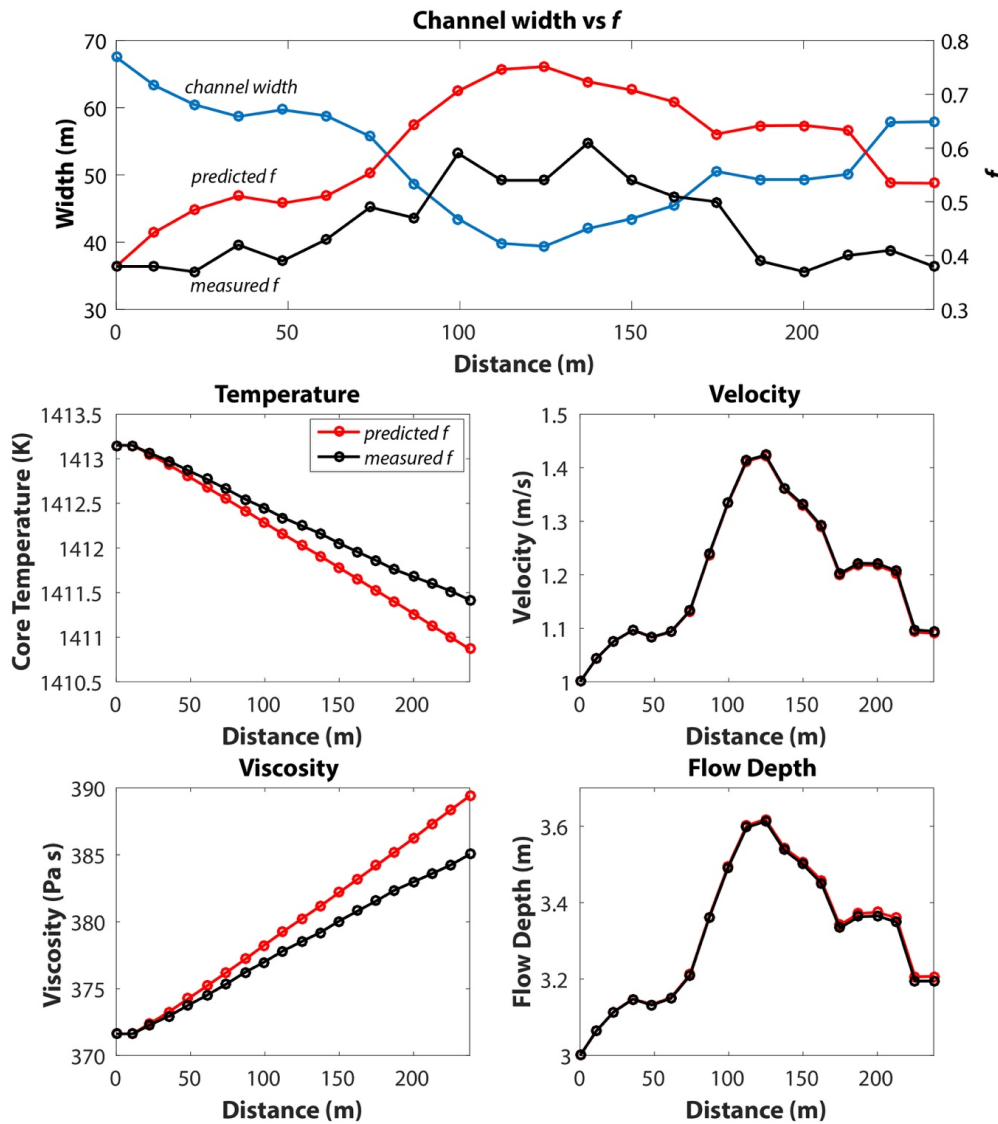


Figure 4.11b. Case 2 model outputs showing predicted fractions of hot core (f) compared to measured values versus measured channel widths with distance, and temperature, viscosity, flow velocity, and flow depth versus distance for predicted (red curves) and measured (black curves) f values. The model overpredicts f for the entire length of the flow although the general trend agrees well with the measured values.

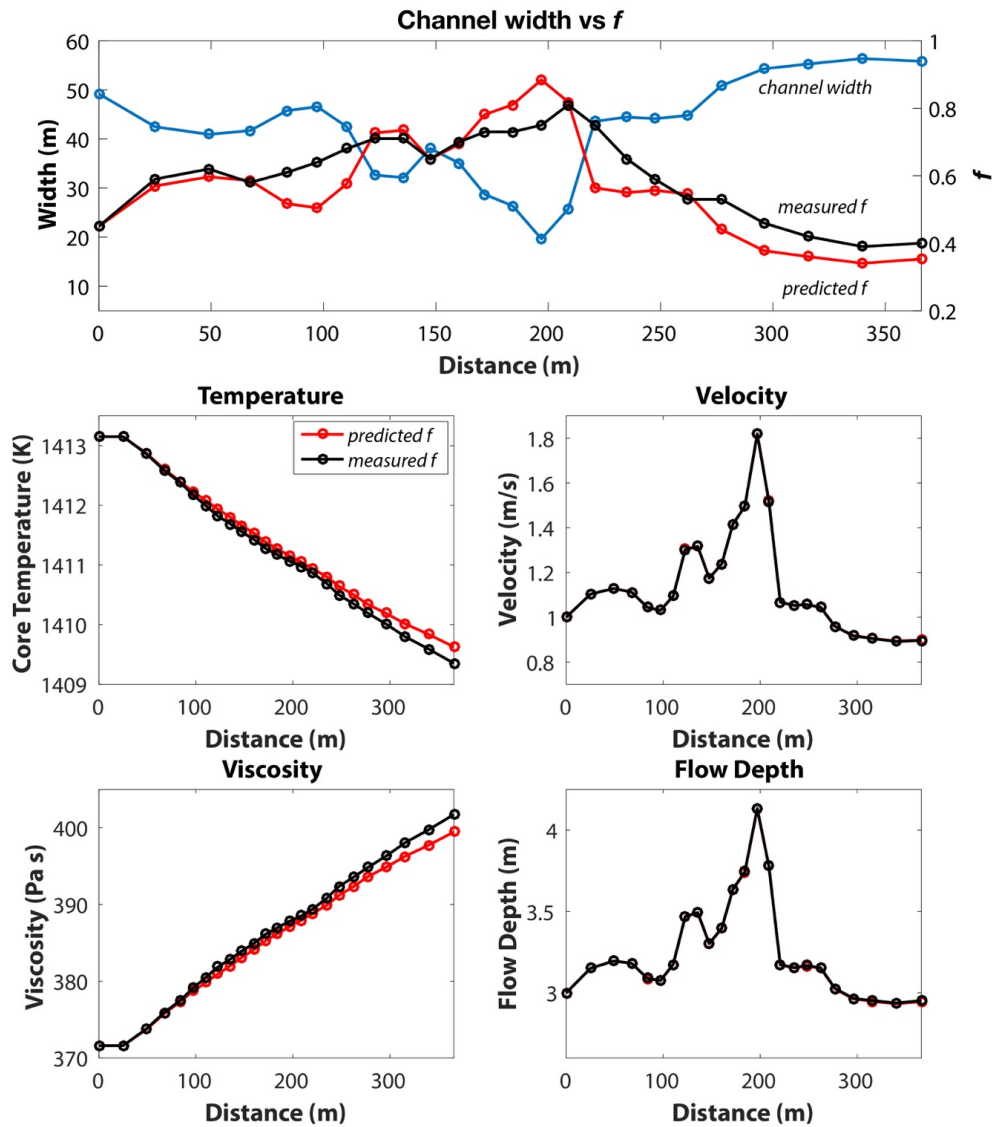


Figure 4.11c. Case 3 model outputs showing predicted fractions of hot core (f) compared to measured values versus measured channel width with distance, and temperature, viscosity, flow velocity, and flow depth versus distance for predicted (red curves) and measured (black curves) f values. The predicted f values agree well with measured values as the flow narrows and widens.

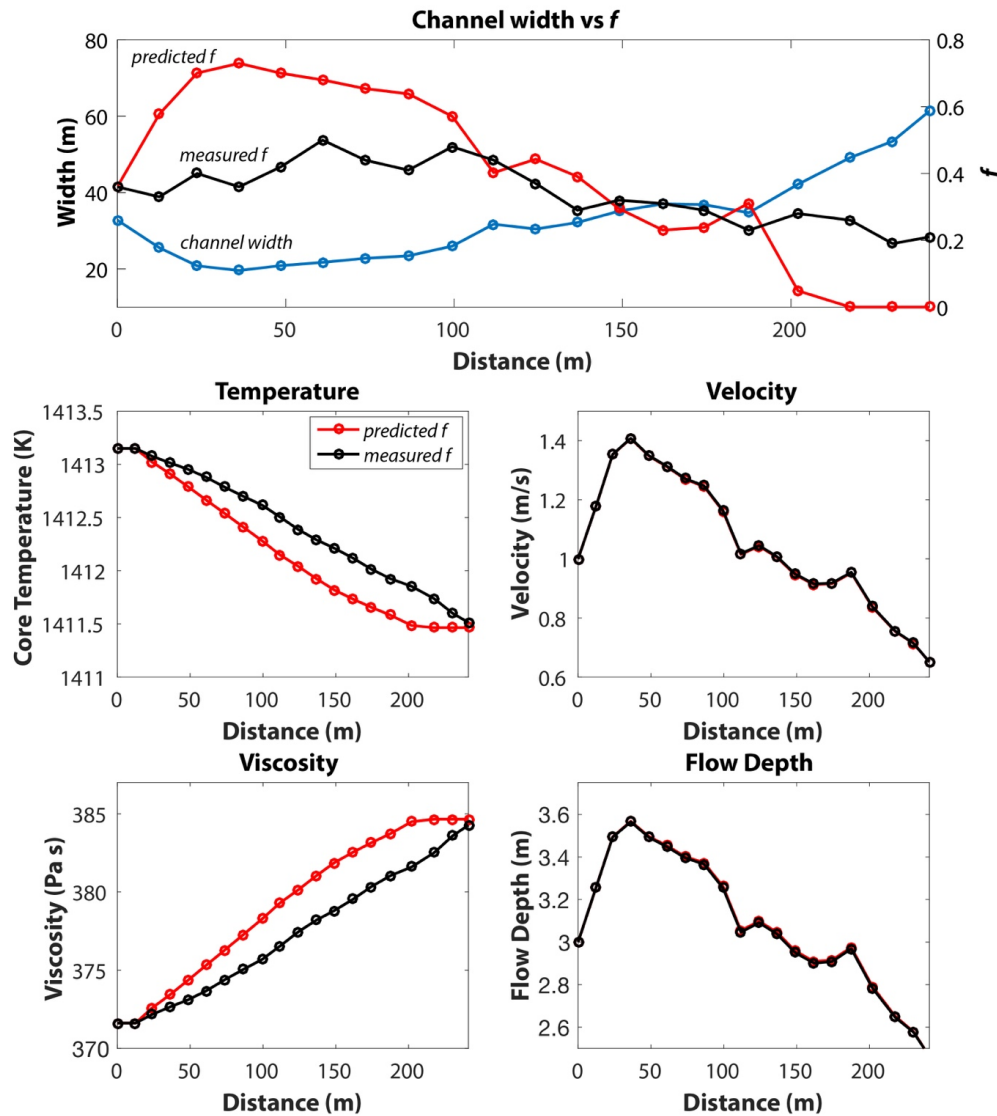


Figure 4.11d. Case 4 model outputs showing predicted fractions of hot core (f) compared to measured values versus measured channel widths with distance, and temperature, viscosity, flow velocity, and flow depth versus distance for predicted (red curves) and measured (black curves) f values. Predicted f values are overestimated for narrow stations and underestimated for wider stations with respect to the measured values.

The best agreement between predicted and measured f values is shown by Case 3 (Figs. 4.2c, 4.11c). Model outputs accurately predicted both the trend and the values of f . Irregularities in the channel margins produce additional, less significant variations in channel width that still affect the f values, velocity, and flow depth predicted by the model.

In Case 4 (Fig. 4.2d, 4.11d), the predicted f values exceed the measured values at the narrowest stations of the channel segment and are underestimated as the channel widens. During the initial widening, both the predicted and measured values agree and begin to decrease together. When the channel begins to widen significantly, however, the measured f values decrease only slowly while the model predicted f values drop rapidly and eventually become zero. Again, the overprediction of f results in a greater temperature decrease and viscosity increase, and the underprediction of f causes temperature and viscosity to both level off.

Constrictions in the channel width have a tendency to increase the fraction of exposed core and cause greater heat loss than if the channel were uniform in width. For comparison, the model was run for a constant width and constant f using the measured values at the first station for Case 3 (Fig. 4.12). In the case of constant width and f , core temperatures are greater and viscosities are less than the resulting profiles for Case 3 with varying widths. Thus the core temperature cools faster when there are constrictions in the flow path that disrupt the surface crust, increasing f . When width, and therefore f , is held constant, the flow does not cool as quickly. Taking into account the variations in width and how they affect crustal coverage is important for the temperature profile of a flow, as they can cause enhancing cooling that may ultimately limit the flow's mobility.

4.6. Discussion

Our model succeeds in predicting the general trends in surface crustal coverage resulting from channel width variations of over distances of several hundred meters, and the predicted f values agree to a variable extent with measurements from the lava flow images. However, we observe some discrepancies between the predicted and measured f values, most notably the tendency in some cases to overpredict f when the channel narrows, and underpredict f when the

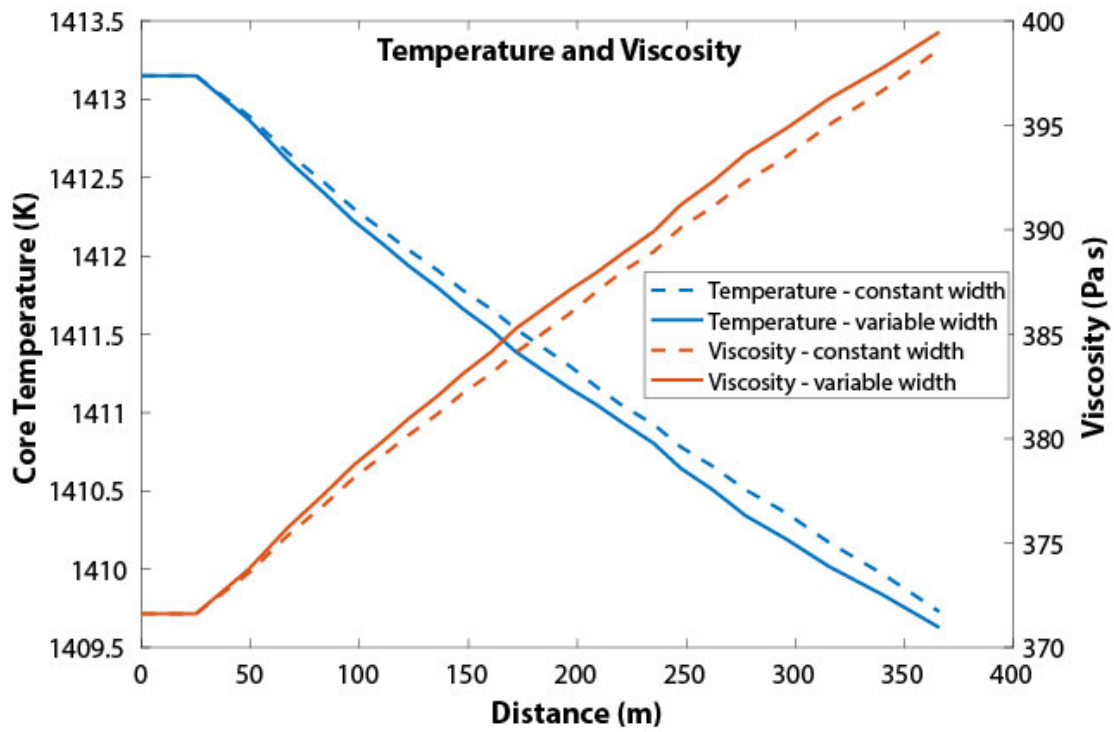


Figure 4.12. Predicted core temperature and viscosity for Case 3 (solid lines) shown in comparison to the case of constant width and constant f (dashed lines). Notice the temperature is less than and viscosity greater than the constant width case.

channel widens. Here we identify limitations in the model that might account for these discrepancies.

First, the model assumes that surface crust is destroyed and created instantaneously in response to changes in shear stresses. In reality, there will be a finite time (distance) over which crust is disrupted due to stresses and reestablished due to cooling, so not accounting for this delay in crust formation and disruption would contribute to the offset between observed and measure f values. Second, by simplifying the treatment of flow dynamics to one dimension, the model is unable to account for lateral velocity components and possible circulation within the lava that are induced when a flow is forced to diverge or converge due to channel width variations. This scenario complicates the treatment of surface stresses to an extent that is beyond the scope of this first-order treatment, but remains an interesting avenue for further study. Third, the treatment of the flow surface as composed of two thermal components (hot core and cooler crust) is a clear simplification of nature. A continuum of temperatures exists but will not be adequately captured in such two-component models [Wright *et al.*, 2003]. For example, Case 1 (Fig. 4.2a) shows a distinct constriction in the channel but the measurements of f change little over this distance. In the image the margins are bright white at the narrow sections and bright yellow at the wider ones. Visually the white margins would appear to be hotter, but because the threshold designates both bright white and bright yellow as exposed core, the f value does not change to reflect this difference. An additional complication is that the model assumes that all hot core material is only exposed at the flow margins, but in nature the crustal distribution is less regular, and cracks exposing hot core can occur across the flow surface.

Finally, although we do not develop a quantitative treatment of the effects of channel bends here, we note that the analyzed lava channel sections (Cases 1–4; Fig. 4.2) commonly have gentle curvature superimposed on them as the flow path is redirected, which may cause additional disruption not accounted for by the model. In the extreme Case 5 (Fig. 4.3), the $\sim 90^\circ$ bend in channel direction exhibits width variations and a significant channel constriction at station 14. The measurements of f from Case 5 suggest that the fraction of hot core material exposed increases as the flow turns through its angle, suggesting that lateral redirections in the

flow path may also cause sufficient changes in the flow dynamics to disrupt surface crust. It is known from the fluvial literature that water in a river encountering a bend will experience a pressure gradient imposed by the sidewalls that cause the fluid to move around the bend, and that this sets up secondary flow in three dimensions, which dominates over irrotational flow. In secondary flow, inward-directed forces exerted on the fluid by the outer channel wall are dominant, and fluid moves from the outside bend to the inside bend along the channel floor, thus inducing circulation (helical flow) [Leopold *et al.*, 1960]. This circulation causes the maximum longitudinal flow velocity to be displaced towards the outer margin of the channel, resulting in higher velocities toward the outside bend. We observe this in the channel bend in Figure 4.3 with the outer flow margin of exposed core growing in width as it passes through the turn. We propose that similar rotational flow behavior takes place in fluid lava encountering channel bends [Booth *et al.*, 1973], and that this circulation is a mechanism that leads to greater hot core exposure, f (e.g., Fig. 4.3) via two possible mechanisms: (i) the internal circulation imparts frictional forces on the underside of crustal components, causing them to translate, break, and/or founder, and (ii) increased shear stresses due to the higher velocities at the outer channel wall cause similar crustal breakage and/or foundering. Neglecting these effects may have contributed to the f mismatches in Cases 1–4.

The cases we examined were for channel lengths of a few hundred meters, but an obvious goal is to apply the model to larger scale examples to predict the consequences of crustal disruption to overall lava flow lengths. As an example, Figure 4.13 compares theoretical core temperature profiles for flows of > 10 km length with a constant width (black curve) and constrictions (red curve). The channel with width constrictions reaches its stopping criterion (cessation temperature) at a distance substantially less than the constant width flow, indicating that cooling and viscosity changes due to disruptions in surface crust can have significant implications on the ultimate flow length. Models that do not account for these surface disruptions can result in an underestimation of final flow lengths.

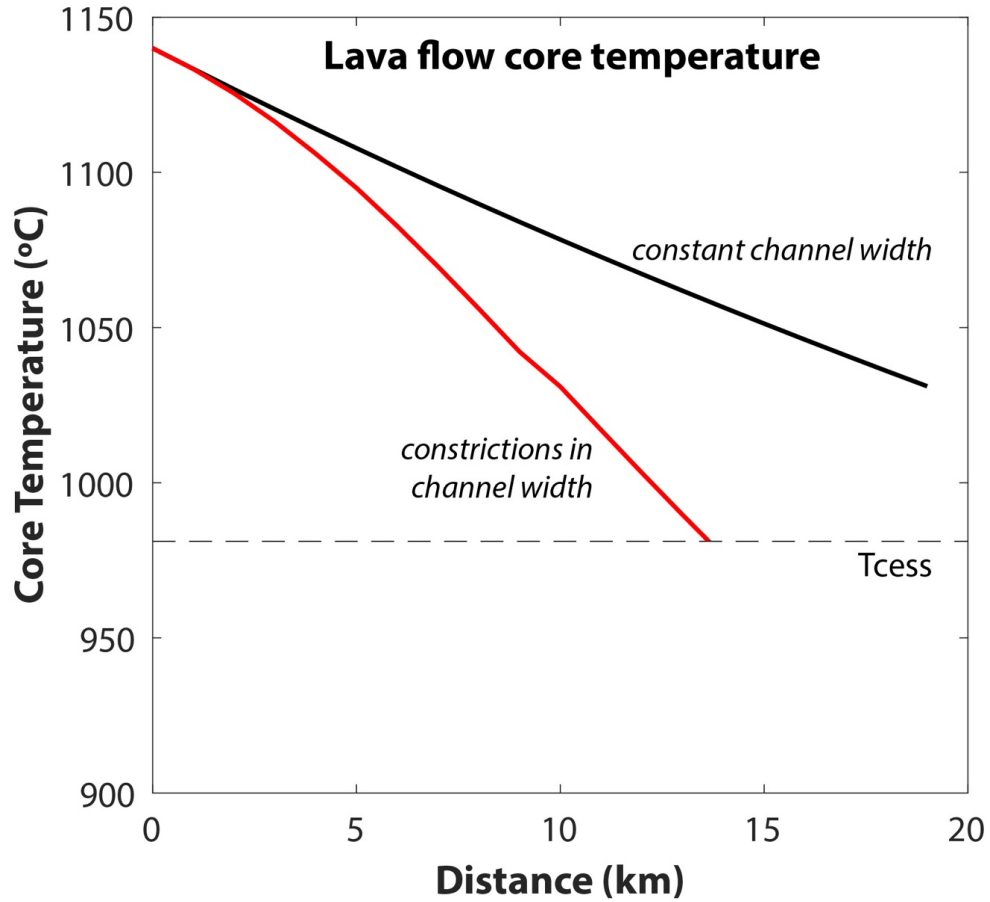


Figure 4.13. Theoretical temperature profile for a channel with constant width and constant f (black curve) and for a channel with a width constrictions (red curve). For the latter case, the temperature drops more rapidly along the flow than for the constant width case, leading to a substantially shorter flow length.

4.7. Conclusions

We have shown that channel width and its variation along the path of an active lava flow are important measurements for understanding the thermal dynamics of the flow. The variations in the width directly affect the shear near the margins of the flow channel. This shear can prevent the formation of or destroy an insulating crust, and induce or increase the internal flow circulation near the channel walls. This circulation is one of the main causes of heat loss from the core. Thus relatively small changes in the channel width (e.g., a few tens of a percent or less) can have a relatively large effect on the thermal loss because of the radiative dependence. Somewhat counterintuitively, a channel width that decreases can increase the radiative heat loss when it inhibits the formation of an insulating crust.

The 2018 Kīlauea eruption produced flows with numerous bends and width changes that highlight their influence on the radiative heat loss. The lava flows from this eruption were well-observed and provided basic data that encouraged our study and the development of an elementary theoretical model to account for such flow phenomena. Our simple model of heat loss from the bright interior channel margins and the inhibition or destruction of surface crust illustrates how the measurements of an active flow can be used to describe these losses quantitatively. The model captures the first-order influence of channel width changes on the heat loss, although the simple model sometimes under-predicts the temperature change for a widening channel and slightly over-predicts the temperature change for one that narrows. The simple model of flow and thermal losses assumes only parallel flow lines within the flow. It is likely that relaxing this assumption in the model would bring the trends in the theoretical predictions more in line with the observations.

We have shown that accounting for disruptions of surface crust can have a significant effect on terminal length. There are clear hazard implications for lava flow emplacement modeling: models that do not incorporate the influence of topography, width variations, and channel bends on surface crustal coverage are likely to underestimate the travel distances of lava flows.

CHAPTER 5. CONCLUSIONS

The work presented in this dissertation contributes to our understanding of several key volcanic processes at Kīlauea, including magma storage and transport, and lava flow dynamics. Our results help to better understand potential volcanic hazards for communities at risk. In the first study, we explored deflation-inflation events recorded in tiltmeter displacements that provided insight into the complexities of the shallow magmatic system and the proposed models for the cause of the events. This work focused on 16 large DI events, but applying our methods to the catalogue of over 500 recorded events could provide a more comprehensive analysis. DI events continue to be recorded in deformation data at Kīlauea summit following the 2018 caldera collapse, and a water pond now exists within Halema‘ūma‘u crater. Future work can be done to investigate DI events under these new conditions at Kīlauea.

The second and third studies were significantly enhanced by exceptional monitoring of the summit collapse and lower ERZ eruption in 2018. In the second study the 1 Hz GPS data from several stations at the summit helped to refine a deformation model of the incremental collapse events. From this analysis, we determined that the vertical shear stresses acting on the walls of the caldera ring faults are greatest at the edges of the magma reservoir and increase as magma pressure decreases, indicating that fault strength likely controls collapse. Our work used a two-dimensional pressurized crack model to determine stress distributions, but a three-dimensional penny-shaped crack model would be ideal to use in future work, and consistent with the deformation model. Tiltmeter data recorded over the same time period can also be incorporated as an additional dataset to constrain the modeling. Finally, a separate model can be developed to explain the sudden outward motion recorded during the time of the earthquakes and collapse.

In the third and final study, we used a theoretical heat loss model to investigate the influence of lava flow geometries on flow emplacement. Videos of active channelized flows from the 2018 lower ERZ eruption provided data that allowed us to quantify the surface area of crustal coverage to be used in the model. Narrowing channel widths were shown to disrupt

surface crust, lowering the core temperature of the flow, and limiting the distance that it can travel. While the model captures the first-order influence of width variations on cooling, assumptions were made which likely contributed to misfits between the model and observations. These included assuming two thermal components of the flow surface, one dimensional velocity profiles, and instantaneous creation and destruction of surface crust. Future work can be done to improve these misfits, and to study how lateral redirections in flow path disrupt surface crust, with the ultimate application being to predict lava flow evolution on large scales for any prescribed set of channel width variations and meanders.

APPENDIX: CESSATION TEMPERATURE

The temperature at which forward motion of a lava flow stops, along with the role of heat loss in controlling flow lengths, has been discussed in numerous studies [*Macdonald* 1963; *Shaw et al.*, 1968; *Walker*, 1973; *Peck*, 1966, 1978; *Pieri and Baloga*, 1986; *Baloga and Pieri*, 1986; *Hon et al.*, 1994; *Crisp and Baloga*, 1990; *Cashman et al.*, 2006; *Harris et al.*, 2001, 2009]. Identifying the extent to which cooling limits a flow is complicated, as several other factors (e.g. effusion rate, erupted volume, eruption duration, morphology, rheology, topography) contribute to the cessation of flow. Temperature measurements of stagnated flows in the field can be challenging to obtain, and the internal thermal complexities of flows and the variations between each flow make it difficult to identify a single representative value. The cessation temperature is proposed as a simplification that accounts for the temperature gradient between the hotter flow interior and the surface crust. It is characterized as the average of the temperature distribution throughout a vertical section of the flow that has stopped moving [*Pieri and Baloga*, 1986].

A thorough discussion of cessation temperature and previously reported values is given by *Pieri and Baloga* [1986]. *Macdonald* [1963] gives field measurements of the “incandescent material just below the cooler surface rubble or visible through cracks” as 750 – 800 °C for “Hawaiian flows at or near cessation of movement.” *Peck* [1966] cites 980 °C for the solidus of Hawaiian basalts, which is also the value given for cooling of the Alae lava lake [*Peck*, 1978], and *Shaw et al.* [1968] give a solidus temperature of ~980 °C for the Makaopuhi lava lake. *Pieri and Baloga* [1986] state that if the solidus temperature is 1000 °C and the temperature below the surface is 750 °C, then a likely range of final core temperatures is 800 – 900 °C. *Hon et al.* [1994] give a range of 800 – 1070 °C for viscoelastic crust based on thermocouple measurements of Kīlauea lava flows. They give a solidification temperature of 1070 °C, below which crust begins to form. *Crisp and Baloga* [1990] comment that “it was necessary for *Pieri and Baloga* [1986] to resort to a core temperature less than solidus 800 – 900 °C to make the thermally unmixed model agree with the data” and give a range of final core temperatures as 980 – 1120 °C, with other cessation temperatures for specific case studies calculated from experimental

measurements of previous works. The FLOWGO model of *Harris and Rowland* [2001] use the *Peck* [1978] solidus value of 980° C for their stopping criterion. The range of temperatures given for different scenarios of cooled lava flows demonstrates the complexity of the cessation temperature concept. The T_{cess} range of 980 – 1030 °C seems to encompass the range of plausible values for Hawaiian basalts in typical eruption and ambient conditions.

The cessation temperature can be described theoretically as a vertical average of two thermal components within the flow. The first component is the inner core at the eruption temperature, T_0 . The second and cooler component is the outer crust at the solidus temperature, $T_{viscoelastic}$, which is the temperature of the transition to viscoelastic rheology, or the lower limit of the viscoelastic regime [*Hon et al.*, 1994]. The eruption temperature is applied over a vertical distance h_{T_0} within the control volume and the second cooler temperature is applied over a total vertical distance $h_{viscoelastic}$. The cessation temperature, T_{cess} , is interpreted as the spatial vertical average such that only the total vertical distance over which the second temperature applies is considered. When the flow stops, a specific fraction of the control volume will be at solidus temperature. The fraction of cooler lava is given by

$$\delta = \frac{h_{viscoelastic}}{h} , \tag{A.1}$$

where h is the total height of the control volume. The cessation temperature can be written as

$$T_{cess} = T_0(1 - \delta) + T_{viscoelastic} \delta . \tag{A.2}$$

If half of the control volume is at the solidus when the flow stops, then the cessation temperature is half way between the eruption temperature and the solidus. If the majority of the control volume is at the solidus when the front stops, then by equation A.2 the cessation temperature is nearly at the solidus. The fraction of solidus lava in the control volume at the front when the flow ceases to advance is given by

$$\delta = \frac{T_0 - T_{cess}}{T_0 - T_{viscoelastic}} \quad (\text{A.3})$$

A constraint exists that is not evident from equations A.1 – A.3, which is interpreted in terms of f . A lower limit of the viscoelastic regime means that f cannot be so large that the viscoelastic regime cannot exceed the flow depth, such that

$$T_{cess} = T_{viscoelastic} = T_0 \left(1 + \frac{fL}{\Lambda} \right)^{\frac{1}{3}} \quad (\text{A. 4})$$

where

$$\Lambda = \frac{\rho C_p h u}{3\varepsilon \sigma T_0^3}$$

REFERENCES

- Almendros, J., Chouet, B., Dawson, P. and Bond, T., 2002. Identifying elements of the plumbing system beneath Kilauea Volcano, Hawaii, from the source locations of very-long-period signals. *Geophysical Journal International*, v. 148: p. 303-312.
- Anderson, K.R., Poland, M.P., Johnson, J.H. and Miklius, A., 2015. Episodic deflation-inflation events at Kīlauea Volcano and implications for the shallow magma system. In: R. Carey, M. Poland, V. Cayol and D. Weis (Editors), *Hawaiian Volcanism: From Source to Surface*. American Geophysical Union Geophysical Monograph Series, v. 208: p. 229-250.
- Apuani, T., Corazzato, C., Cancelli, A., and Tibaldi, A., 2005. Physical and mechanical properties of rock masses at Stromboli: a dataset for volcano instability evaluation. *Bulletin of Engineering Geology and the Environment*, v. 64(no. 4): p. 419.
- Baker, S. and Amelung, F., 2012. Top-down inflation and deflation at the summit of Kīlauea Volcano, Hawai‘i observed with InSAR. *Journal of Geophysical Research: Solid Earth*, 117(B12406): 14 p.
- Baloga, S. and Pieri D., 1986. Time dependent profiles of lava flows. *Journal of Geophysical Research*, v. 91: p. 9543-9552.
- Battaglia, J., Got, J.-L. and Okubo, P., 2003. Location of long-period events below Kilauea Volcano using seismic amplitudes and accurate relative relocation. *Journal of Geophysical Research*, v. 108(no. B12): p. ESE 2-1 to ESE 2-16.
- Booth, B. and Self S., 1973. Rheological features of the 1971 Mt Etna lavas. *Proceedings of the Royal Society of London. Series A*, v. 274: p. 99-106.
- Cashman, K.V., Thornber, C.R. and Kauahikaua, J.P., 1999. Cooling and crystallization of lava in open channels, and the transition of pahoehoe lava to 'a'a. *Bulletin of Volcanology*, p. 306-323.
- Cashman K.V., Kerr R.C. and Griffiths, R.W., 2006. A laboratory model of surface crust formation and disruption on lava flows through non-uniform channels. *Bulletin of Volcanology*, v. 68: p. 753-770. doi: 10.1007/s00445-005-0048-z.
- Cervelli, P.F. and Miklius, A., 2003. The shallow magmatic system of Kilauea Volcano. In: C.C. Heliker, D.A. Swanson and T.J. Takahashi (Editors), *U.S. Geological Survey Professional Paper 1676. The Pu'u 'O'o-Kupaianaha eruption of Kilauea Volcano, Hawai'i: the first 20 years*, pp. p. 149-163.
- Chouet, B.A., Dawson, P.B., James, M.R. and Lane, S.J., 2010. Seismic source mechanism of degassing bursts at Kilauea Volcano, Hawaii: Results from waveform inversion in the 10-50 s band. *Journal of Geophysical Research*, v. 115(no. B09311): 24 p.
- Crisp, J.A. and Baloga, S.M., 1990a. A model for lava flows with two thermal components. *Journal of Geophysical Research*, v. 95: p. 1255-1270.

- Crisp, J.A. and Baloga, S.M., 1990b. Methods for estimating eruption rates of planetary lava flows. *Icarus*, v. 85: p. 512-515.
- Dawson, P., Whilldin, D. and Chouet, B., 2004. Application of near real-time radial semblance to locate the shallow magmatic conduit at Kilauea Volcano, Hawaii. *Geophysical Research Letters*, v. 31(no. 21 (L21606)): p. 1-4. doi:10.1029/2004GL021163.
- Dawson, P.B., Chouet, B.A., Okubo, P.G., Villasenor, A. and Benz, H.M., 1999. Three-dimensional velocity structure of the Kilauea caldera, Hawaii. *Geophysical Research Letters*, v. 26(no. 18): p. 2805-2808.
- Decker, R.W. and Christiansen, R.L., 1984. Explosive eruptions of Kilauea volcano, Hawai'i. In: National Research Council and others (Editors), *Explosive volcanism: Inception, evolution, and hazards (Studies in geophysics)*, National Academy Press, p. 122-132.
- Decker, R.W., 1987. Dynamics of Hawaiian Volcanoes: an overview. In: R.W. Decker, T.L. Wright and P.H. Stauffer (Editors), *Volcanism in Hawaii*, U.S. Geological Survey Professional Paper 1350, v. 2: p. 997-1018.
- Decker, R.W., Okamura, A., Miklius, A. and Poland, M., 2008. Evolution of deformation studies on active Hawaiian volcanoes. U.S. Geological Survey Scientific Investigations Report, 2008-5090, 23 p.
- Delaney, P.T., Fiske, R.S., Miklius, A., Okamura, A.T. and Sako, M.K., 1990. Deep magma body beneath the summit and rift zones of Kilauea Volcano, Hawaii. *Science*, v. 247(March 16): p. 1311-1316.
- Delaney, P.T., Miklius, A., Arnadottir, T., Okamura, A.T. and Sako, M.K., 1993. Motion of Kilauea Volcano during sustained eruption from the Puu Oo and Kupaianaha vents, 1983-1991. *Journal of Geophysical Research*, v. 98(no. B10): p. 17,801-817,820.
- Denlinger, R.P., 1997. A dynamic balance between magma supply and eruption rate at Kilauea Volcano, Hawaii. *Journal of Geophysical Research*, v. 102(no. B8): p. 18,091-018,100.
- Dieterich, J.H. and Decker, R.W., 1975. Finite element modeling of surface deformation associated with volcanism. *Journal of Geophysical Research*, v. 80(no. 29): p. 4094-4102.
- Dragoni, M.A., 1989. A dynamical model of lava flows cooling by radiation. *Bulletin of Volcanology*, v. 51: p. 88-95.
- Duffield, W.A., Christiansen, R.L., Koyanagi, R.Y. and Peterson, D.W., 1982. Storage, migration, and eruption of magma at Kilauea Volcano, Hawaii, 1971-1972. *Journal of Volcanology and Geothermal Research*, v. 13: p. 273-307.
- Dvorak, J.J. and Dzurisin, D., 1993. Variations in magma supply rate at Kilauea Volcano, Hawaii. *Journal of Geophysical Research*, v. 98(no. B12): p. 22,255-22,268.
- Dvorak, J.J. and Dzurisin, D., 1997. Volcano geodesy: the search for magma reservoirs and the formation of eruptive vents. *Reviews of Geophysics*, v. 35(no. 3): p. 343-384.
- Dvorak, J.J. and Okamura, A.T., 1987. A hydraulic model to explain variations in summit tilt rate at Kilauea and Mauna Loa Volcanoes. In: R.W. Decker, T.L. Wright and P.H. Stauffer (Editors), U.S. Geological Survey Professional Paper 1350. *Volcanism in*

- Hawaii, pp. p. 1281-1296.
- Dzurisin, D., 2003. A comprehensive approach to monitoring volcano deformation as a window on the eruption cycle. *Reviews of Geophysics*, v. 41(no. 1): p. 1-1 to 1-29.
- Dzurisin, D., Anderson, L.A., Eaton, G.P., Koyanagi, R.Y., Lipman, P.W., Lockwood, J.P., Okamura, R.T., Puniwai, G.S., Sako, M.K. and Yamashita, K.M., 1980. Geophysical observations of Kilauea Volcano, Hawaii, 2. Constraints on the magma supply during November 1975-September 1977. In: A.R. McBirney (Editor), *Journal of Volcanology and Geothermal Research. Gordon A. Macdonald Memorial Volume (special issue)*, pp. p. 241-269.
- Dzurisin, D. and Lu, Z., 2007. *Volcano deformation--Geodetic monitoring techniques*. Springer-Verlag, Berlin, 441 pp.
- Eaton, J.P., 1962. Crustal structure and volcanism in Hawaii, *American Geophysical Union Geophysical Monograph 6. Crust of the Pacific Basin*, pp. p. 13-29.
- Fagents, S.A. and Greeley, R., 2001. Factors influencing lava-substrate heat transfer and implications for thermomechanical erosion. *Bulletin of Volcanology*, v. 62: p. 519-532.
- Fialko, Y., Khazan, Y. and Simons, M., 2001. Deformation due to a pressurized horizontal circular crack in an elastic half-space, with applications to volcano geodesy. *Geophysical Journal International*, v. 146(no. 1): p. 181-190. <http://dx.doi.org/10.1046/j.1365-246X.2001.00452.x>.
- Fiske, R.S. and Kinoshita, W.T., 1969. Inflation of Kilauea Volcano prior to its 1967-1968 eruption. *Science*, v. 165: p. 341-349.
- Fiske, R.S., Swanson, D.A. and Wright, T.L., 1993. A model of Kilauea Volcano's rift-zone magma system [abs.]. *Eos, Transactions, American Geophysical Union supp.*, v. 74(no. 43): p. 646.
- Geshi, N., Shimano, T., Chiba, T. and Nakada, S., 2002. Caldera collapse during the 2000 eruption of Miyakejima Volcano, Japan. *Bulletin of Volcanology*, v. 64: p. 55-68. doi: 10.1007/s00445-001-0184-z.
- Genco, R. and Ripepe, M., 2010. Inflation-deflation cycles revealed by tilt and seismic records at Stromboli volcano. *Geophysical Research Letters*, v. 37(no. 12).
- Giordano, D., Potuzak, M., Romano, C., Dingwell, D.B. and Nowak, M., 2008a. Viscosity and glass transition temperature of hydrous melts in the system CaAl₂Si₂O₈–CaMgSi₂O₆. *Chemical Geology*, v. 256(3-4): p. 203-215.
- Giordano, D., Russell, J.K. and Dingwell, D.B., 2008b. Viscosity of magmatic liquids: a model. *Earth and Planetary Science Letters*, v. 271(1-4): p. 123-134
- Glaze, L.S., Baloga, S.M., Fagents, S.A. and Wright, R., 2014. The influence of slope breaks on lava flow surface disruption. *Journal of Geophysical Research*, v. 119. doi:10.1002/2013JB010696.
- Griffith, A.A., 1924. The theory of rupture. *Proceedings of the first International Congress for Applied Mechanics, Delft*, p. 55.

- Griffiths, R.W., Kerr, R.C. and Cashman, K.V., 2003. Patterns of solidification in channel flows with surface cooling. *Journal of Fluid Mechanics*, v. 496: p. 33-62.
- Gudmundsson, M.T., et al., 2016. Gradual caldera collapse at Bárðarbunga volcano, Iceland, regulated by lateral magma outflow. *Science*, v. 353(no. 6296): p. 262. doi:10.1126/science.aaf8988.science.org.
- Haney, M.M., Patrick, M.R. and Anderson, K.R., 2016. Ground Tilt Time Delays between Kilauea Volcano's Summit and East Rift Zone Caused by Magma Reservoir Buffering [abs.]. *Eos Transactions AGU, Fall Meeting Suppl. 2016: Abstract V12A-06H*.
- Harris, A.J.L. and Rowland S.K., 2001. FLOWGO: A kinematic thermo-rheological model for lava flowing in a channel. *Bulletin of Volcanology*, v. 63: p. 20-44.
- Harris, A.J.L., and Rowland S.K., 2009. Effusion rate controls on lava flow length and the role of heat loss. In: T. Thordarson, et al. (Editors), *Studies in Volcanology: The Legacy of George Walker, Special Publication, IAVCEI, Geological Society, London*, v. 2: p. 33-51.
- Heliker, C.C. and Mattox, T.N., 2003. The first two decades of the Pu'u 'O'o-Kupaianaha eruption: chronology and selected bibliography. In: C.C. Heliker, D.A. Swanson and T.J. Takahashi (Editors), *U.S. Geological Survey Professional Paper 1676. The Pu'u 'O'o-Kupaianaha eruption of Kilauea Volcano, Hawaii: the first 20 years*, pp. p. 1-27.
- Holcomb, R.T., 1987. Eruptive history and long-term behavior of Kilauea Volcano. In: R.W. Decker, T.L. Wright and P.H. Stauffer (Editors), *U.S. Geological Survey Professional Paper 1350. Volcanism in Hawaii*, pp. p. 261-350.
- Hon, K., Kauahikaua, J., Denlinger, K.R. and Mackay, K., 1994. Emplacement and inflation of pahoehoe sheet flows: Observations and measurements of active lava flows on Kilauea Volcano, Hawaii. *Geological Society of America Bulletin*, v. 106(no. 3): p. 351-370.
- Hulme, G., 1982. A review of lava flow processes related to the formation of lunar sinuous rilles. *Surveys in Geophysics*, v. 5: p. 245-279.
- Jackson, D.B., Swanson, D.A., Koyanagi, R.Y. and Wright, T.L., 1975. The August and October 1968 east rift eruptions of Kilauea Volcano, Hawaii. *U.S. Geological Survey Professional Paper 890: 33 p.*
- Johnson, D.J., 1992. Dynamics of magma storage in the summit reservoir of Kilauea Volcano, Hawaii. *Journal of Geophysical Research*, v. 97(no. B2): p. 1807-1820.
- Johnson, D.J., Eggers, A.A., Bagnardi, M., Battaglia, M., Poland, M.P. and Miklius, A., 2010. Shallow magma accumulation at Kilauea Volcano, Hawai'i, revealed by microgravity surveys. *Geology*, v. 38(no. 12): p. 1139-1142.
- Kauahikaua, J. and Poland, M., 2012. One hundred years of volcano monitoring in Hawaii. *EOS Transactions*, v. 9: p. 29-40. doi: 10.1029/2012EO030001.
- Klein, F.W., Koyanagi, R.Y., Nakata, J.S. and Tanigawa, W.R., 1987. The seismicity of Kilauea's magma system. In: R.W. Decker, T.L. Wright and P.H. Stauffer (Editors), *U.S. Geological Survey Professional Paper 1350. Volcanism in Hawaii*, pp. p. 1019-1185.

- Kumagai, H., Ohminato, T., Nakano, M., Ooi, M., Kubo, A., Inoue, H. and Oikawa, J., 2001. Very-Long-Period Seismic Signals and Caldera Formation at Miyake Island, Japan. *Science*, v. 293: p. 687-690.
- Lengliné, O., Marsan, D., Got, J.-L., Pinel, V., Ferrazzini, V. and Okubo, P.G., 2008. Seismicity and deformation induced by magma accumulation at three basaltic volcanoes. *Journal of Geophysical Research*, 113(B12305).
- Leopold, L.B. and Gordon, M.W., 1960. River Meanders. *GSA Bulletin*, v. 71(no. 6): p. 769-793. doi: [https://doi.org/10.1130/0016-7606\(1960\)71\[769:RM\]2.0.CO;2](https://doi.org/10.1130/0016-7606(1960)71[769:RM]2.0.CO;2).
- Lisowski, M., 2007. Analytical volcano deformation source models. In: D. Dzurisin (Editor). *Volcano deformation: geodetic monitoring techniques*. Springer Verlag, Germany, in association with Praxis Publishing, Ltd., UK, Berlin, Germany, and Chichester, UK, pp. p. 279-304.
- Lockwood, J.P., Tilling, R.I., Holcomb, R.T., Klein, F., Okamura, A.T. and Peterson, D.W., 1999. Magma migration and resupply during the 1974 summit eruptions of Kilauea Volcano, Hawai'i. *U.S. Geological Survey Professional Paper 1613*: 37 p.
- Longpré, M.A., Staudacher, T. and Stix, J., 2007. The November 2002 eruption at Piton de La Fournaise volcano, La Réunion Island: ground deformation, seismicity, and pit crater collapse. *Bulletin of Volcanology*, v. 69: p. 511-525. doi:10.1007/s00445-006-0087-0.
- Lundgren, P., Poland, M., Miklius, A., Orr, T., Yun, S.-H., Fielding, E., Liu, Z., Tanaka, A., Szeliga, W., Hensley, S. and Owen, S., 2013. Evolution of dike opening during the March 2011 Kamoamoā fissure eruption, Kīlauea Volcano, Hawai'i. *Journal of Geophysical Research: Solid Earth*, v. 118(B3): p. 897-914.
- Macdonald, G.A., 1963. Physical properties of erupting Hawaiian magmas. *Geological Society of America Bulletin*, v. 74: p. 1071-1078.
- Macdonald, G.A., Abbott, A.T. and Peterson, F.L., 1970. *Volcanoes in the Sea: The Geology of Hawaii*. University of Hawaii Press.
- Macdonald, G.A., Abbott, A.T. and Peterson, F.L., 1983. *Volcanoes in the Sea: The Geology of Hawaii*, 2nd edition. University of Hawaii Press.
- Michon, L., Staudacher, T., Ferrazzini, V., Bachelery, P. and Marti, J., 2007. April 2007 collapse of Piton de la Fournaise: A new example of caldera formation. *Geophysical Research Letters*, 34(L21301). doi:1029/2007GL031248.
- Michon, L., Villeneuve, N., Catry, T. and Merle, O., 2009. How summit calderas collapse on basaltic volcanoes: New insights from the April 2007 caldera collapse of Piton de la Fournaise volcano. *Journal of Volcanology and Geothermal Research*, v. 184: p. 138-15.
- Miklius, A. and Cervelli, P., 2003. Interaction between Kilauea and Mauna Loa. *Nature*, 421(6920): p. 229.
- McTigue, D.F., 1987. Elastic stress and deformation near a finite spherical magma body: resolution of the point source paradox. *Journal of Geophysical Research*, v. 92(no. B12): p. 12, 931-912, 940.

- Mogi, K., 1958. Relations between the eruptions of various volcanoes and the deformations of the ground surfaces around them. *Bulletin of the Earthquake Research Institute of the University of Tokyo*, v. 36: p. 111-123.
- Montgomery-Brown, E.K., Sinnett, D.K., Poland, M., Segall, P., Orr, T., Zebker, H. and Miklius, A., 2010. Geodetic evidence for an echelon dike emplacement and concurrent slow slip during the June 2007 intrusion and eruption at Kīlauea volcano, Hawaii. *Journal of Geophysical Research*, v. 115(B07405): 15 p.
- Moore, J.G., 1987. Subsidence of the Hawaiian Ridge. In: R.W. Decker, T.L. Wright and P.H. Stauffer (Editors), *Volcanism in Hawaii: U.S. Geological Survey Professional Paper 1350*, v. 1, p. 85-100.
- Moore, J.G. and Clague, D.A., 1992. Volcano Growth and Evolution of the Island of Hawaii. *GSA Bulletin*, 104(11): p. 1471-1484. doi: 10.1130/0016-7606(1992).
- Myer, D., Sandwell, D., Brooks, B., Foster, J. and Shimada, M., 2008. Inflation along Kilauea's Southwest Rift Zone in 2006. *Journal of Volcanology and Geothermal Research*, v. 177(no. 2): p. 418-424.
- Neal, C.A., et al., 2019. The 2018 rift eruption and summit collapse of Kīlauea Volcano: *Science*, v. 363(no. 6425): p. 367-374. <https://doi.org/10.1126/science.aav7046>.
- Ohminato, T., Chouet, B.A., Dawson, P.B. and Kedar, S., 1998. Waveform inversion of very long period impulsive signals associated with magmatic injection beneath Kilauea Volcano, Hawaii. *Journal of Geophysical Research*, v. 103(no. B10): p. 23,839-823,862.
- Okubo, P.G., Nakata, J.S. and Koyanagi, R.Y., 2014. The evolution of seismic monitoring systems at the Hawaiian Volcano Observatory. In: M.P. Poland, T.J. Takahashi and C.M. Landowski (Editors), *U.S. Geological Survey Professional Paper 1801. Characteristics of Hawaiian volcanoes*, pp. p. 66-95.
- Orr, T.R., Thelen, W.A., Patrick, M.R., Swanson, D.A. and Wilson, D.C., 2013. Explosive eruptions triggered by rockfalls at Kīlauea volcano, Hawai'i. *Geology*, 41(2): 207-210.
- Owen, S., Segall, P., Lisowski, M., Miklius, A., Murray, M., Bevis, M. and Foster, J., 2000. January 30, 1997 eruptive event on Kilauea Volcano, Hawaii, as monitored by continuous GPS. *Geophysical Research Letters*, v. 27(no. 17): p. 2757-2760.
- Patrick, M.R. and Orr, T.R., 2013. Controls on lava lake level at Halema'uma'u Crater, Kilauea Volcano [abs.]. *American Geophysical Union, Fall Meeting 2013 Abstracts: abstract no. V52C-04*.
- Patrick, M.R., Orr, T.R., Sutton, A.J., Elias, T. and Swanson, D.A., 2013. The first five years of Kīlauea's summit eruption in Halema'uma'u Crater, 2008–2013. *U.S. Geological Survey Fact Sheet 2013-3116*: 4 p.
- Peck, D.L., Wright, T.L. and Moore, J.G., 1966. Crystallization of tholeiitic basalt in alae lava lake, Hawaii. *Bulletin of Volcanology*, v. 29: p. 629-656.
- Peltier, A., Staudacher, T., Bachelery, P. and Cayol, V., 2009b. Formation of the April 2007 caldera collapse at Piton de La Fournaise volcano: Insights from GPS data. *Journal of*

- Volcanology and Geothermal Research, v. 184: p. 152-163.
doi:10.1016/j.jvolgeores.2008.09.009.
- Peterson, D.W. and Moore, R.B., 1987. Geologic history and evolution of geologic concepts, Island of Hawaii. In: R.W. Decker, T.L. Wright and P.H. Stauffer (Editors), U.S. Geological Survey Professional Paper 1350. Volcanism in Hawaii, pp. p. 149-189.
- Pieri, D.C. and Baloga S.M., 1986. Eruption rate, area and length relationships for some Hawaiian lava flows. *Journal of Volcanology and Geothermal Research*, v. 30: p. 29-45.
- Pietruszka, A.J. and Garcia, M.O., 1999. The size and shape of Kilauea Volcano's summit magma storage reservoir: a geochemical probe. *Earth and Planetary Science Letters*, v. 167(3-4): p. 311-320. [http://dx.doi.org/10.1016/S0012-821X\(99\)00036-9](http://dx.doi.org/10.1016/S0012-821X(99)00036-9).
- Pinkerton, H. and Wilson, L., 1994. Factors controlling the lengths of channel-fed lava flows. *Bulletin of Volcanology*, v. 56: p. 108-120.
- Poland, M.P., Huth, T.E. and Miklius, A., 2009. Source processes of short-term, transient tilt events at Kilauea Volcano, Hawaii [abs.]. *Eos, Transactions, American Geophysical Union supp.*, v. 90(no. 52): abstract no. V43G-2331.
- Poland, M.P., Miklius, A. and Montgomery-Brown, E.K., 2014. Magma supply, storage, and transport at shield-stage Hawaiian volcanoes. In: M.P. Poland, T.J. Takahashi and C.M. Landowski (Editors), U.S. Geological Survey Professional Paper 1801. Characteristics of Hawaiian volcanoes, pp. p. 178-235.
- Poland, M.P., Miklius, A., Sutton, A.J. and Thornber, C.R., 2012. A mantle-driven surge in magma supply to Kilauea Volcano during 2003-2007. *Nature Geoscience*, v. 5(no. 4): p. 295-300.
- Poland, M.P., Miklius, A., Sutton, A.J. and Thornber, C.R., 2012. A mantle-driven surge in magma supply to Kilauea Volcano during 2003-2007. *Nature Geoscience*, v. 5(no. 4): p. 295-300.
- Poland, M.P., Sutton, A.J. and Gerlach, T.M., 2009. Magma degassing triggered by static decompression at Kilauea Volcano, Hawai'i. *Geophysical Research Letters*, v. 36(no. L16306): 5 p.
- Quareni, F., Tallarico, A. and Dragoni, M., 2004. Modeling of the steady-state temperature field in lava flow levees. *Journal of Volcanology and Geothermal Research*, v. 132: p. 241-251.
- Roche, O., van Wyk de Vries, B. and Druitt, T.H., 2001. Sub-surface structures and collapse mechanisms of summit pit craters. *Journal of Volcanology and Geothermal Research*, v. 105: p. 1-18.
- Ryan, M.P., 1988. The mechanics and three-dimensional internal structure of active magmatic systems: Kilauea Volcano, Hawaii. *Journal of Geophysical Research*, v. 93(no. B5): p. 4213-4248.
- Ryan, M.P., Koyanagi, R.Y. and Fiske, R.S., 1981. Modeling the three dimensional structure of macroscopic magma transport systems: application to Kilauea Volcano, Hawaii. *Journal*

- of Geophysical Research, v. 86(no. B8): p. 7111-7129.
- Segall, P., 2013. Volcano deformation and eruption forecasting. Geological Society, London, Special Publications, v. 380(no. 1): p. 85-106.
- Segall, P., Cervelli, P., Owen, S., Lisowski, M. and Miklius, A., 2001. Constraints on dike propagation from continuous GPS measurements. *Journal of Geophysical Research*, v. 106(no. B9): p. 19,301-319,317.
- Sharp, W.D. and Clague, D.A., 2006. 50–Ma initiation of Hawaiian-Emperor bend records major change in Pacific Plate motion. *Science*, 313(5791): p. 1281-1284. doi: 10.1126/science.1128489.
- Shaw, H., Wright, T.J., Peck, D. and Okamura, R., 1968. The viscosity of basaltic magma; An analysis of field measurements in Makaopuhi lava lake, Hawaii. *American Journal of Science*, v. 266: p. 225-264.
- Shimozuru, D., 1981. Magma reservoir systems inferred from tilt patterns. *Bulletin Volcanologique*, v. 44(no. 3): p. 499-504.
- Simkin, T. and Howard, K.A., 1970. Caldera collapse in the Galapagos Islands, 1968. *Science*, v. 169: p. 429-437.
- Sneddon, I. N., 1946. The distribution of stress in the neighborhood of a crack in an elastic solid, *Proceedings of the Royal Society of London, Series A*, v. 187: p. 229-260.
- Staudacher, T., Ferrazzini, V., Peltier, A., Kowalski, P., Boissier, P., Catherine, P., Lauret, F. and Massin, F., 2009. The April 2007 eruption and the Dolomieu crater collapse, two major events at Piton de la Fournaise. *Journal of Volcanology and Geothermal Research*, v. 184: p. 126-137.
- Stearns, H.T., 1946. *Geology of the Hawaiian Islands*. Hawaii Division of Hydrography. Honolulu, Hawaii.
- Swanson, D.A., Duffield, W.A., Jackson, D.B. and Peterson, D.W., 1979. Chronological narrative of the 1969-71 Mauna Ulu eruption of Kilauea Volcano, Hawaii. U.S. Geological Survey Professional Paper 1056: 55 p.
- Swanson, D.A., Jackson, D.B., Koyanagi, R.Y. and Wright, T.L., 1976. The February 1969 east rift eruption of Kilauea Volcano, Hawaii. U.S. Geological Survey Professional Paper 891: p. 1-30.
- Swanson, D.A., Rose, T.R., Mucek, A.E., Garcia, M.O., Fiske, R.S. and Mastin L.G., 2014. Cycles of explosive and effusive eruptions at Kīlauea Volcano, Hawai'i. *Geology*, v. 42(no. 7): p. 631-634.
- Trusdell, F., 2011. Dueling volcanoes: How activity levels at Kilauea influence eruptions at Mauna Loa. American Geophysical Union Fall Meeting, San Francisco, California, 5–9 December, V33E-08.
- Thornber, C.R., Heliker, C., Sherrod, D.R., Kauahikaua, J.P., Miklius, A., Okubo, P.G., Trusdell, F.A., Budahn, J.R., Ridley, W.I. and Meeker, G.P., 2003. Kilauea east rift zone magmatism: an episode 54 perspective. *Journal of Petrology*, v. 44(no. 9): p. 1525-1559.

- Tilling, R.I., 1987. Fluctuations in surface height of active lava lakes during 1972-1974 Mauna Ulu eruption, Kilauea Volcano, Hawaii. *Journal of Geophysical Research*, v. 92(no. B13): p. 13,721-713,730.
- Tilling, R.I. and Dvorak, J.J., 1993. Anatomy of a basaltic volcano. *Nature*, v. 363: p. 125-133. <http://dx.doi.org/10.1038/363125a0>.
- Ukawa, M., Fujita, E., Yamamoto, E., Okada, Y., and Kikuchi, M., 2000. The 2000 Miyakejima eruption: Crustal deformation and earthquakes observed by the NIED Miyakejima observation network. *Earth, Planets Space*, v. 5: p. xix-xxvi.
- Valerio, A., Tallarico A. and Dragoni M., 2011. Effects of the curvature of a lava channel on flow dynamics and crust formation, *Geophysical Journal International*, v. 187: p. 825-832. doi:10.1111/j.1365-246X.2011.05166.X.
- Voight, B., Hoblitt, R.P., Clarke, A.B., Lockhart, A.B., Miller, A.D., Lynch, L. and McMahon, J., 1998. Remarkable cyclic ground deformation monitored in real-time on Montserrat, and its use in eruption forecasting. *Geophysical Research Letters*, v. 25(no. 18): p. 3405-3408.
- Weron, R., 2010. REMST: MATLAB function to remove trend and seasonal component using the moving average method. Statistical Software Components M429001, Boston College Department of Economics.
- Wolfe, E.W., Garcia, M.O., Jackson, D.B., Koyanagi, R.Y., Neal, C.A. and Okamura, A.T., 1987. The Puu Oo eruption of Kilauea Volcano, episodes 1-20, January 3, 1983, to June 8, 1984. In: R.W. Decker, T.L. Wright and P.H. Stauffer (Editors), U.S. Geological Survey Professional Paper 1350. *Volcanism in Hawaii*, pp. p. 471-508.
- Wilson, J.T., 1963. A possible origin of the Hawaiian Islands. *Canadian Journal of Physics*, v. 41: p. 863-870. doi: 10.1139/p63-094.
- Wright, T.L., 1984. Origin of Hawaiian tholeiite: A metasomatic model. *Journal of Geophysical Research*, 89(B5): p. 3233-3252.
- Wright, R. and Flynn, L.P., 2003. On the retrieval of lava flow surface temperatures from infrared satellite data. *Geology*, v. 31: p. 893-896.
- Wright, T.L. and Klein, F.W., 2014. Two hundred years of magma transport and storage at Kilauea Volcano, Hawai‘i, 1790–2008. U.S. Geological Survey Professional Paper 1806: 240 p.
- Yamashina, K.I., Matsushima, T. and Ohmi, S., 1999. Volcanic deformation at Unzen, Japan, visualized by a time-differential stereoscopy. *Journal of Volcanology and Geothermal Research*, v. 89(no. 1): 73-80.
- Yang, X., Davis, P.M., Delaney, P.T. and Okamura, A.T., 1992. Geodetic analysis of dike intrusion and motion of the magma reservoir beneath the summit of Kilauea Volcano, Hawaii: 1970-1985. *Journal of Geophysical Research*, v. 97(no. B3): p. 3305-3324.